

https://dspace.org/

A multi-frequency study of the Sunyaev Zel'dovich effect and its polarization in cosmic structures

Emritte, Mohammad Shehzad

2014-07-21
http://hdl.handle.net/10539/14934

Downloaded from a DSpace repository. https://dspace.org/

A Multi-frequency study of the Sunyaev Zel'dovich effect and its polarization in cosmic structures

Mohammad Shehzad Emritte
Supervisor: Prof. Sergio Colafrancesco

A thesis presented for the degree of
Master of Science in Physics

Department Name : School of Physics
University Name: University of the Witwatersrand
Country: South Africa
Date:24/05/2014

Abstract

The Sunyaev-Zel'dovich effect (hereafter SZE), i.e. the distortion of the cosmic microwave background (CMB) spectrum due to inverse Compton scattering of CMB photons off energetic electrons in cosmic structures, is a relevant investigation tool for astrophysical and cosmological studies. Since the SZE is an interaction between photons and electrons, polarization arises as a natural outcome and then provides the SZE with an important complementary component as an astrophysical and cosmological probe. This thesis is an extensive study on the SZE in non-relativistic and relativistic regime including polarization. We first perform a study on a set of galaxy clusters hosting radio halos where we constrain the non-thermal pressure present in these structures using multifrequency data such as SZE, radio and X-ray. We found that the average ratio between non-thermal to thermal pressure is ≈ 0.5. We then derive, in the full relativistic regime, a general formulation of the properties of the SZE, and we further derive the Stokes parameters, Q and U, of the polarized SZE. This is done in a general case by solving the polarized Boltzmann collisional integral in the Thomson limit that allows us to extract the Stokes parameters for arbitrary electron distribution functions. We further discuss the spectral features of the SZE polarization as produced by other additional effects occurring in the cluster atmospheres, like finite optical depth effects and transverse plasma motions. We finally apply the results of our study to different cosmic structures (e.g. galaxy clusters and radio galaxies) and we discuss the relevance of SZE polarization in the study of extragalactic astrophysical plasmas and for cosmological

applications.

Acknowledgements

I acknowledges support by the South African Research Chairs Initiative of the Department of Science and Technology and National Research Foundation and by the Square Kilometre Array (SKA). I also acknowledges the continuous and enlightening supervision of Prof. S. Colafrancesco, the SKA Research Chair in radioastronomy at Wits University, and it was a great opportunity for me to work with such a great astrophysicist like him. He has been a very good source of guidance for me during these past 2 years. I am also very greatful for the support of the School of Physics and the Faculty of Science of Wits University and I show my appreciation for Prof Daniel Joubert as well as Prof John Carter. I am also very grateful to Dr P. Marchegiani for his encouragement as well as the useful discussions that I've had with him and also my colleagues, Asha Tailor, Peter Nicol and Nicola Orford in the office for their support both morally and academically. I also acknowledge Marco Tullio for his discussions and for giving me the right information concerning the work. Thanks also goes to my parents, Salim and Banon as well as my brothers Umar and Zeehad for always believing in me and supporting me from the start till the end of this journey. An appreciation also goes to Mr Sanjeevi Cuneapen, Mr Tamir Husam and Mr Jamil Laloo. I would like to also thank my cousins Anass and Yasmina Emritte, Mohammad and Surayya Santally and my uncle Yusuf Santally as well as my friend Taha and his wife Imaan. I am very grateful also to my friends Mubeen,Razeena,Talha Khan and their family for their hospitality, kindness and support. A special thank goes to Nebiha Shafi for her advice as well as her

friendship.

Contents

1 Introduction **19**

1.1 Galaxy clusters 21

1.1.1 Physical constituents of galaxy clusters 21

1.1.2 The Sunyaev Zel'dovich effect 33

1.1.3 Polarization of the Sunyaev Zel'dovich effect 36

2 Theoretical modelling of galaxy clusters **39**

2.1 Galaxy cluster quantities and parameters 40

2.2 X-ray luminosity 41

2.3 Integrated Compton parameter 42

3 Multifrequency constraints on non-thermal pressure in galaxy clusters **43**

3.1 X-ray, radio and SZE data 44

3.2 $P_{1.4} - L_X$ and $Y_{SZ} D_A^2 - P_{1.4}$ and $Y_{sph,R500} - L_X$ correlations . . 44

3.2.1 $Y_{SZ} - L_X$ relation 48

3.2.2 Evolution of the non-thermal pressure with X-ray luminosity 50

3.3 Results 54

3.4 Implications of the existence of a non-thermal pressure in galaxy clusters 55

3.5 Discussion 56

4 The relativistic SZ effect **57**

4.1 Thomson scattering in the SZ effect 58

4.2 Scattering Kernel 60

4.2.1 Thermal electrons 61

4.2.2 Non-thermal electrons 61

4.3 The spectrum of the SZ effect 63

4.3.1 Full scattering kernel $P(s)$ 65

5 Polarization of the Sunyaev Zeldovich effect **69**

5.1 Polarization due to the CMB quadrupole 70

5.2 Polarization of the SZE in the relativistic formalism 73

5.2.1 The distribution function in the Thomson approximation 76

5.2.2 Stokes parameters 80

5.2.3 The Stokes parameter I 82

5.2.4 CMB multipoles and polarization of the SZE 87

5.2.5 Combination of two electron populations 91

5.2.6 SZE polarization due to finite optical depth 93

5.2.7 SZE polarization due to tranverse motion of cosmic structures 95

6 Structure of astrophysical plasmas **99**

6.1 Plasma structure from SZE polarization 100

6.2 Reconstruction of peculiar velocity field 102

6.3 SZE polarization from radio galaxy lobes and radio relics 103

6.4 Testing the homogeneity of the Universe with the SZE 108

7 Conclusions and future outline **115**

A Photon re-distribution functions of the CMB radiation **129**

B The RH clusters sample **139**

List of Figures

1.1 The galaxy cluster Abell 1989 observed with Hubble Space Telescope (Kravtsov & Borgani 2012). 22

1.2 The Coma cluster in X-ray showing its thermal plasma content (Bohringer & Werner 2009) 24

1.3 The X-spectra of a thermal plasma showing the different mechanisms: bremsstrahlung (blue), recombination (green) and 2-photon (red) (see review by Bohringer & Werner 2009). One can see that at higher temperatures thermal bremsstrahlung becomes the dominant mechanism for X-ray emission in galaxy clusters. . 25

1.4 Diffuse radio emissions in galaxy clusters shown in contours overlaid on the X-ray emission shown in color. From top to bottom and left to right are A2219 (halo), A2744 (halo+relics), A115 (relic), A754 (complex, halo+relic), A1664 (relic), A548b (relic), A520 (halo), A2029 (mini-halo) and RXJCJ1314.4-2515 (halo+double relics) (Feretti et al. 2012). 30

1.5 The radio flux vs frequency for the Coma Cluster for different intracluster medium magnetic field, B (Blasi & Colafrancesco (1999)). 31

1.6 The spectral distortion function $g(x)$ for a thermal population of electrons in the Kompaneets approximation (solid curve) and the relativistic spectral distortion due to a non-thermal population of electrons (dotted-curve). 35

3.1 The fit between $P_{1.4}$ and L_X in log-log plane. Our result gives a normalization -56.04 ± 3.18 and slope of 1.78 ± 0.07 (Colafrancesco et al. 2013). 45
3.2 The fit between $P_{1.4}$ and $Y_{SZ}D_A^2$ in log-log plane. Our result gives a normalization 31.16 ± 0.36 and slope of 1.80 ± 0.10 (Colafrancesco et al. 2013). 46
3.3 The fit between $Y_{sph,R500}E(z)^{9/4}$ and L_X in log-log plane. Our result gives a normalization -44.11 ± 2.23 and slope of 0.89 ± 0.05. 48
3.4 The fit between $Y_{sph,R500}E(z)^{9/4}$ and L_X in log-log plane (Red) and the beta model (green) for $\beta = 2/3$ and $\lambda = 0.3$. A value of $X = 0.55 \pm 0.05$ is obtained (Colafrancesco et al. 2013). 49
3.5 The variation of the non-thermal pressure ratio X with β (Colafrancesco et al. 2013). 50
3.6 The variation of the non-thermal pressure ratio X with λ (Colafrancesco et al. 2013). 51
3.7 The fit to the X-L_X data. We obtain a normalization 43.49 ± 7.09 and slope -0.96 ± 0.16 (Colafrancesco et al. 2013). 53
3.8 We show here the best fit (green) to the data together with the constant non-thermal (violet) and that of the one decreasing with luminosity (blue) (Colafrancesco et al. 2013). 54

4.1 Scattering geometry in the rest frame of the electron. 59
4.2 The scattering kernel for a thermal electron distribution $P_1(s)$ at different temperatures. 63
4.3 The scattering kernel for a non thermal electron distribution $P_1(s)$ for different minimum momentum p_1. 64
4.4 The change in intensity for an isotropic incident radiation for different plasma temperatures. 65
4.5 The change in intensity for an isotropic incident radiation for different minimum momentum p_1 for a single power law electron distribution. 66

4.6 The change in intensity for an isotropic incident radiation using the exact redistribution kernel $P(s)$ computed for a thermal population of electrons for different optical depth. We used $\tau = 0.01$ for the first order approximation. 67

4.7 The change in intensity for an isotropic incident radiation using the exact redistribution kernel $P(s)$ computed for a non-thermal population of electrons for different optical depth. We use $\tau = 0.01$ for the first order approximation. 68

5.1 The Stokes parameter Q with $a_{2,2} = 10^{-4}$ and $\tau = 0.01$. 72

5.2 The degree of polarization in the case of $|a_{2,2}| = 0.0001$ and $\tau = 0.01$. 72

5.3 The spectrum of the Stokes parameter Q for different temperature of the plasma arising from the quadrupole of the CMB, assumed here to be $a_{2,2} = 3 \times 10^{-4}$ 90

5.4 The spectrum of the Stokes parameter Q for different temperature of the plasma arising from the quadrupole of the CMB, assumed here to be $a_{3,2} = 7 \times 10^{-4}$ 91

5.5 The scattering geometry for double scattering.The second electron is located at the origin of the coordinate system and it receives a radiation from the first electron in the direction (θ, ϕ). The first electron has already introduced a SZE and the second electron sees an anisotropy in the radiation because of the directional dependence of the optical depth $\tau_e(\theta, \phi)$. The second electron then generates polarization when it Thomson scattered the radiation received from the first electron. 94

6.1 The Q Stokes parameter arising from the primordial anisotropy of the CMB for a spherical plasma distribution. The green curve represents the Stokes parameter in the non-relativistic domain. . 100

6.2 The Stokes parameter Q associated with the quadrupole of the CMB for different plasma temperatures at low frequencies. 101
6.3 The encircle regions A and B represent two substructures moving with peculiar velocities -1150 km/s and 2492 km/s along the line of sight (Ruan et al. 2013.). 103
6.4 The thermal (red) and kinetic SZE (blue) spectral distortions for structures A and B. The black curve shows the spectral distortion arising from the superposition of both components (Ruan et al. 2013.).$I_0 = 2(k_B T_0)^3/(hc)^2$ 104
6.5 The Q Stokes parameter spectrum for substructure A for an optical depth $\tau_e = 0.01$. The red curve shows the KSZE spectrum and the purple curve shows the primordial anisotropy spectrum. The blue curve shows the superposition of the two. 105
6.6 The Q Stokes parameter spectrum for substructure B for an optical depth $\tau_e = 0.01$. The red curve shows the KSZE spectrum and the purple curve shows the primordial anisotropy spectrum. The blue curve shows the superposition of the two. 106
6.7 The SZE expected from a set of radio galaxies considered by Colafrancesco et al. 2012. 107
6.8 The spectrum of the Stokes parameter $Q(x)$ associated with the quadrupole of the CMB, computed for the relativistic electrons that inhabit RG lobes. 107
6.9 The spectrum of the Stokes parameter $Q(x)$ associated with the octopole of the CMB, computed for the relativistic electrons that inhabit RG lobes. 108
6.10 We show here the spectrum of the Stokes parameter Q associated with the quadrupole for a thermal population (green) at 5.1 keV, a non-thermal population (dotted) and the combination of both. 109
6.11 We show here the spectrum of the Stokes parameter Q associated with the octopole for a thermal population (green) at 5.1 keV, a non-thermal population (dotted) and the combination of both. . 110

6.12 Galaxy surveys are snapshots of our past lightcone (Maartens 2011). 111
6.13 Scattering of CMB photons by galaxy clusters into our past lightcone (Maartens 2011). 112
6.14 The quadrupole and the octopole at low frequencies for a plasma temperature of 5.1 keV. 113

A.1 The re-distribution function $P_{0,0}(s)$ associated with the monopole for a thermal population of electrons. 130
A.2 The re-distribution function $P_{0,0}(s)$ associated with the monopole for a non-thermal population of electrons. 131
A.3 The re-distribution function $P_{1,0}(s)$ associated with the dipole for a thermal population of electrons. 132
A.4 The re-distribution function $P_{1,0}(s)$ associated with the dipole for a non-thermal population of electrons. 133
A.5 The re-distribution function $P_{2,2}(s)$ associated with the quadrupole for a thermal population of electrons. 134
A.6 The re-distribution function $P_{2,2}(s)$ associated with the quadrupole for a non-thermal population of electrons. 135
A.7 The re-distribution function $P_{3,2}(s)$ associated with the quadrupole for a thermal population of electrons. 136
A.8 The re-distribution function $P_{3,2}(s)$ associated with the quadrupole for a non-thermal population of electrons. 137

List of Tables

3.1 Clusters name and their corresponding calculated X parameters (Colafrancesco et al. 2013). 52

4.1 Minimum momentum p_1 and the optical depth τ_{rel} 62

B.1 The RH clusters sample. Clusters with "*" means no errors available and "**" means no avaliable data 140

B.2 Cluster values for Y_{SZ} and associated uncertainty Θ_X 141

Declaration

I declare that this dissertation is my own, unaided work. It is being submitted for the Degree of Master of Science to the University of the Witwatersrand, Johannesburg. It has not been submitted before for any degree or examination to any other University.

_____

(Signature)

_____

(Date)

Chapter 1

Introduction

Studying the structuration of the Universe consists in studying how galaxies, galaxy clusters, stars and planets form and evolve from their initial cosmological conditions. The starting point of the structuration of the Universe is today well known: the tiny inhomogeneities in the cosmic microwave background, as observed by Planck (Ade et al. 2013), and previously by WMAP (Wilkinson Microwave Background Anisotropy Probe) (Bennett et al. 2003) and COBE (Cosmic Background Explorer) (Smoot et al. 1992).

The theoretical framework of the study of structure formation in the Universe is the so-called cosmological concordancel model, with its two main components: dark energy and dark matter, in addition to the smaller baryonic matter amount of the Universe. Thus, observing the structuration of the Universe is also a way to test the cosmological model.

The cosmic microwave background (CMB) radiation (Penzias & Wilson 1965) is one of the greatest observable supporting the cosmological concordance model with the Universe emerging from a Planck-scale singularity referred to as the Big Bang. Around 300,000 years after this event, the temperature falls down to ≈ 3000 K due to the expansion of the Universe and neutral atoms (e.g hydrogen) was able to form resulting in radiation and matter to decoupled. This radiation is what we refer to as the CMB (see e.g., Peebles 1992, Physical Cosmology, for a

complete description). The observed spectrum of the CMB by COBE (Mather et al. 1990, 1994) follows very closely that of a blackbody spectrum with a characteristic temperature of ≈ 2.7 K, showing that matter and radiation were in thermal equilibrium in the early Universe.

The cosmological Standard Model predicts small primordial fluctuations in the matter-energy density fluid after the epoch of recombination that appear as CMB anisotropies on various angular scales. The anisotropy of the CMB at the level of $\sim 10^{-5}$ observed by COBE (Smoot et al. 1992), WMAP (Benett et al. 2003) and Planck 2013 (Ade et al. 2013) gives us firm observational evidence that structure formation started from small fluctuations in the early Universe. According to this scenario galaxy clusters are at the top of this hierarchy as they are the largest gravitationally bound structures in the Universe, hence implying that they must have had enough time to collapse and accrete cosmic materials over linear scales of $\approx$ Mpc. Such primordial density inhomogeneities, due to their gravitational instability, cause matter to agglomerate on various linear scales, hence hierarchically forming cosmic structures from galaxies to galaxy clusters and superclusters of galaxies (see, e.g., Narayanan & Croft 1999 for an extensive discussion).

The formation of galaxy clusters is well explained within a hierarchical clustering scenario (see e.g., Press & Schechter 1994, Colafrancesco, Lucchin & Matarrese 1989, Bond et al 1991, Colafrancesco and Vittorio 1994). Within this paradigm, galaxy clusters are the result of the merging of smaller structures (sub-clusters and groups of galaxies) collapsed at earlier epochs. The process continues along the cosmic time with larger and larger mass structures collapsing at later epochs, thus resulting in a hierarchical scenario of the evolution of clusters and large-scale structures. Studying galaxy clusters together with the CMB allows hence to link structure formation scenarios to the cosmological initial conditions.

In this Thesis we will concentrate our study on the use of the SZE as a probe of the astrophysical mechanisms for cluster formation and evolution and as a cosmological probe of the Universe as a whole. We will start hence our discussion from a brief description of the structure of galaxy clusters.

1.1 Galaxy clusters

Galaxy clusters are gravitationally bound structures consisting of $\sim 10^2 - 10^3$ galaxies distributed over a region of ≈ 1 Mpc^3 (see e.g. Sarazin 1988 for a review) bound in the potential well created by Dark matter. Initial studies of galaxy clusters were first performed by Wolf (1906) and then Zwicky (1933) but it was only after Abell (1958) made a compilation of them that these objects became widely known as relevant cosmological cosmic structures. The optical classification of galaxy clusters are based on their morphologies (structure, shape, and other morphological parameters) and a popular system of classification is based on the work of Bautz & Morgan (1970). Fig 1.1 shows an optical image of the galaxy cluster A1989. However, these large cosmic structures contain not only galaxies (with their stellar and gaseous content), but also large amounts of hot ionized gas, relativistic and/or supra-thermal plasmas, magnetic fields, and Dark Matter as we will briefly describe in the following sections.

1.1.1 Physical constituents of galaxy clusters

Dark Matter

Observing the velocity dispersion of the galaxies in the Coma cluster, Zwicky (1933) could not explain the high values of the observed velocity dispersion 1019 ± 360 km s^{-1} assuming that only galaxies contribute to the cluster mass in the virial theorem, $2T + U = 0$ where T is the kinetic energy and U is the gravitational potential of the system. Consistently with our current theory of gravity (General Relativity), a direct way to alleviate this discrepancy is to assume that there is more mass in the cluster volume than one can actually observe in the luminous objects. This invisible mass is what is now referred to as Dark Matter (DM).

Dark Matter is the main constituent of galaxy clusters accounting for a mass fraction of about 80% of the total cluster's mass. Dark matter reveals itself only through its gravitational influence on the velocity distribution of the galax-

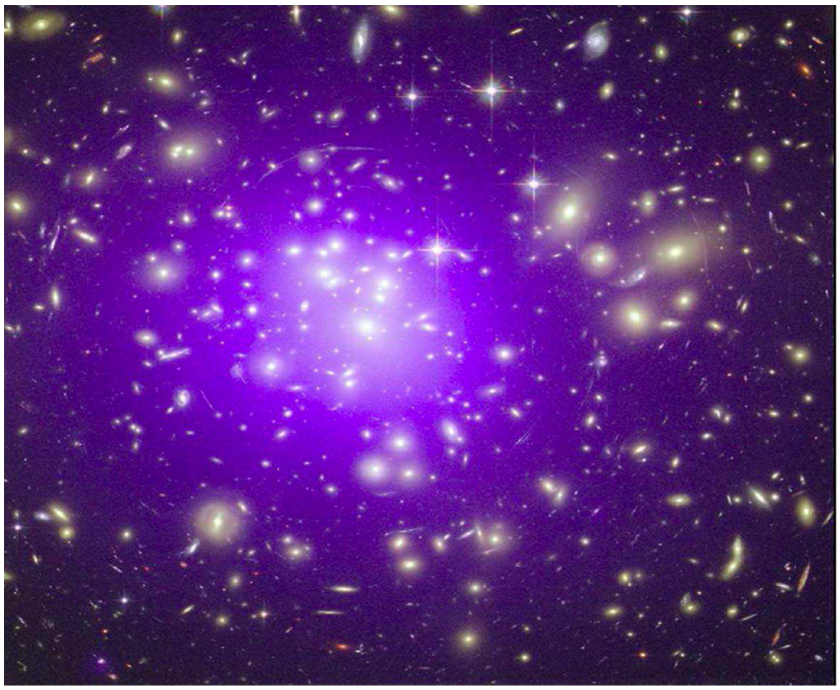

Figure 1.1: The galaxy cluster Abell 1989 observed with Hubble Space Telescope (Kravtsov & Borgani 2012).

ies and on the gravitational lensing effect distorting the images of background sources along the line of sight through a galaxy cluster (see e.g., Blandford & Narayan 1992). DM is a crucial ingredient of the cosmic fluid for the formation of cosmic structures (galaxies, clusters of galaxies etc.) (see e.g., Vergados, Hansen & Host 2008). On cosmological scales, DM provides about 26 % of the total matter-energy content of the Universe and yet it is totally elusive to observational evidence. Because DM interacts only gravitationally with ordinary matter, it is invisible over the whole electromagnetic spectrum and this is one of the evidence among others that indicates the non-baryonic nature of dark matter. Even though we don't know what DM actually is, several candidates have been proposed so far for its nature (see e.g., Feng 2010): two main viable particle candidates are the WIMPs (Weakly Interacting Massive Particles) (see

e.g., Jungman, Kamionkowski & Griest 1996) and Axions (see Peccei & Quinn 1977, Sikivie 2010).

DM probes are of inference and physical character (see Colafrancesco 2010 for a review). Inference probes [i.e., the CMB anisotropy spectrum (see, e.g., Hu & Dodelson 2002,Spergel et al. 2003), the dynamics of galaxies (Zwicky 1933), the hydrodynamics of the hot intra-cluster gas (see a review by Sarazin 1988) and the gravitational lensing distortion of background galaxies by the intervening potential wells of galaxy clusters (see Bartelmann & Schneider 1999 for a review and references therein)] tell us about the presence, the total amount and the spatial distribution of DM in the large scale structures of the Universe but cannot provide detailed information on the nature of DM. Physical probes tell us about the nature and the physical properties of the DM particles and can be obtained by studying the astrophysical signals of their annihilation/decay in the atmospheres of DM-dominated structures (like galaxy cluster and galaxies). These probes can be recorded over a wide range of frequencies from radio to gamma-rays and prelude to a full multi-frequency, multi-experiment and multi-messenger search for the nature of DM in cosmic structures. A detailed description of the multifrequency search for the nature of DM in galaxy clusters has been given by Colafrancesco, Profumo and Ullio (2006).

The Intracluster Medium (ICM)

In addition to DM and galaxies, galaxy clusters host a hot plasma known as the Intracluster Medium (ICM) which reveals itself mainly via X-ray emission (see e.g.,reviews by Bohringer & Werner 2009, Sarazin 1988) due to thermal bremsstrahlung (Rybicki & Lightman 1979). For example Figure 1.2 shows an X-ray image of the Coma cluster of galaxies.The X-ray bolometric luminosity, $L_X \propto n_{e,th} T_e^{1/2}$, where $n_{e,th}$ is the number density of thermal electrons and T_e is their temperature, ranges between $\sim 10^{44}$ and 10^{46} erg/s. This means that the ICM is mainly consisting of a thermal plasma in equilibrium with the gravitational potential provided by the DM and represents about 15 % of the

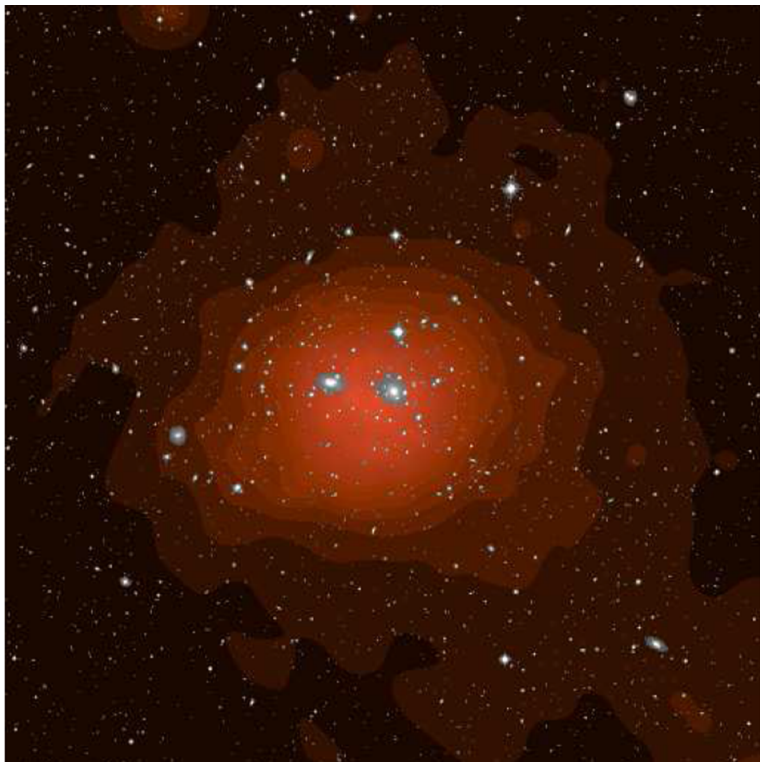

Figure 1.2: The Coma cluster in X-ray showing its thermal plasma content (Bohringer & Werner 2009)

galaxy cluster total mass (i.e. it provides a gas mass of $M \approx 10^{14}\odot$, see review by Sarazin 1988). The temperature T_e of the ICM ranges from $\sim$ 1 keV up to $\sim$17 keV (Reichert et al. 2011, Tucker et al. 1998) and at these temperatures the dominant emission mechanism in a thermal plasma is thermal bremsstrahlung, as shown in Fig 1.3. The ICM is the main baryonic component of a galaxy cluster and it has been extensively observed in X-ray for almost every massive cluster known today. One can derive from observations of the ICM information on crucial physical quantities of galaxy clusters like the total cluster mass, the plasma temperature, and its pressure (see e.g., Arnaud et al. 2010): we will discuss this issue in more detail in the next chapter.

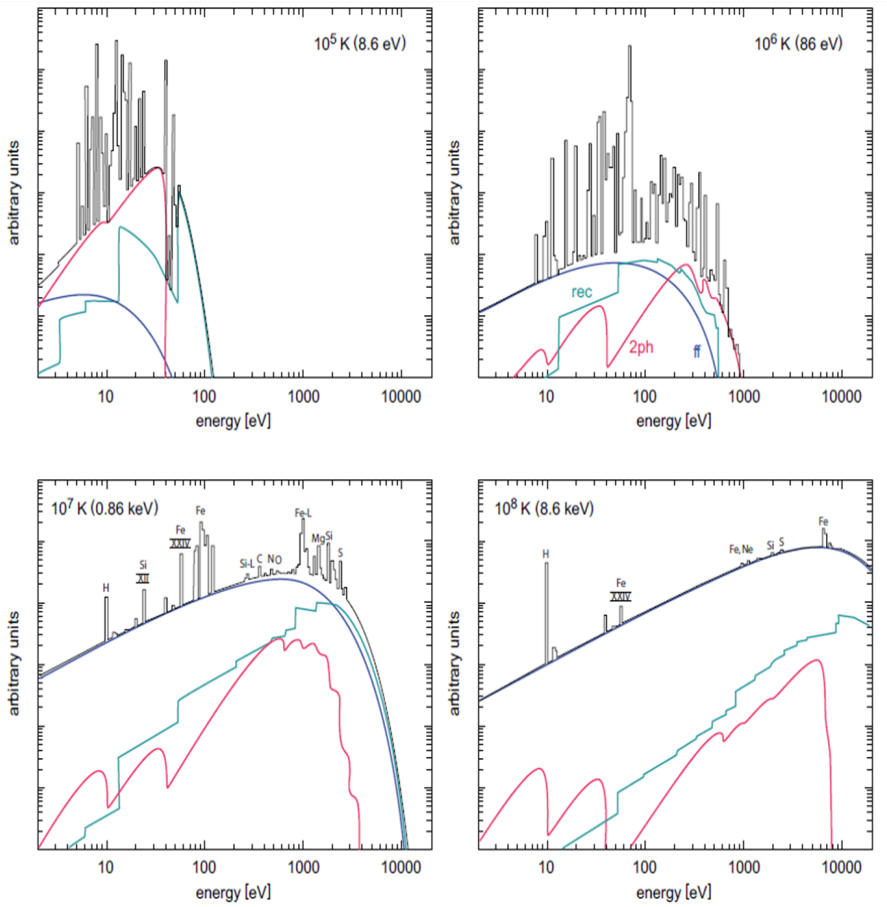

Figure 1.3: The X-spectra of a thermal plasma showing the different mechanisms: bremsstrahlung (blue), recombination (green) and 2-photon (red) (see review by Bohringer & Werner 2009). One can see that at higher temperatures thermal bremsstrahlung becomes the dominant mechanism for X-ray emission in galaxy clusters.

Magnetic field

Radio observations of galaxy clusters in the frequency range between 10 MHz and 10 GHz (e.g., Giovannini 2004 and Govoni & Feretti 2004) show the existence of diffuse large-scale radio emissions. Depending on the morphology and

spectral features of the diffuse radio emission regions, galaxy clusters are classified as containing a radio halo, a mini-halo or relics. In the case of radio halo, the diffuse radio emission region is mostly concentrated around the center of the cluster and depending on the size it may be referred to as halo or mini-halo, whereas relics are diffuse radio emissions typically found at the periphery of clusters. Some clusters presenting diffuse radio emissions of different types (halo,mini-halo and relics) are shown in Fig 1.4.

The radio flux in radio halos vary with frequencies with a power law spectrum, $P_\nu \propto \nu^{-(q-1)/2}$, which suggests that it is synchrotron radiation emitted by relativistic particles (electrons) interacting with large-scale magnetic fields. The sources of these magnetic fields could be of primordial origin or could have been created in the post-recombination epoch. Emitting synchrotron radiation at these frequencies suggests the existence of magnetic field with amplitude $\approx$ few μG and energies of particles around several GeVs (Longair 1993). The rate at which the electrons spiralling the magnetic fields emit radiation is

$$-\frac{d\epsilon}{dt} \approx 1.6 \times 10^{-15} \gamma_e^2 (B_{[G]} \sin\theta)^2 [erg/s], \tag{1.1}$$

and the critical frequency at which the radiation is peaked is

$$\nu_c = 4.2 \times (B_{[G]} \sin\theta) \gamma^2, \tag{1.2}$$

where γ_e is the Lorentz factor. For a given frequency $\nu_c = 100$MHz and magnetic field $B = \mu$G indicates a value of $v_e \approx 0.99c$ for the speed of the electrons.

The synchrotron power at 1.4 GHz , $P_{1.4}$, is proportional to the number density of relativistic electrons and the magnetic field, given as follows

$$P_{1.4} \propto n_{e,rel} B^{(q+1)/2} \nu^{-(q-1)/2}, \tag{1.3}$$

and $n_{e,rel}$ is the number density of relativistic electrons. The electron energy distribution associated (Colafrancesco et al 2012) with this type of radio spectra is of power-law type given by

$$N_e(\epsilon) d\,\epsilon = N_0 \epsilon^{-q} d\,\epsilon. \tag{1.4}$$

The observed value of $P_{1.4}$ ranges between $\sim 10^{24}$ and $\sim 10^{25}$ W/Hz (see Brunetti et al. 2009). It has been recognized that galaxy clusters hosting radio-halos, show a correlation between the power at 1.4 GHz, $P_{1.4}$ and their X-ray luminosity L_X (see e.g., Colafrancesco 1999, Giovannini & Feretti 2000), $P_{1.4} \propto L_X^a$ with a lying in the range $1.5 - 2.1$ (Brunetti et al.2009). The number density of relativistic electrons in galaxy clusters lies typically between 10^{-4} and 10^{-5} per cm^3 but this number density depends on the minimum momentum p_1 assumed for electrons (see e.g., Colafrancesco et al. 2003, Ensslin and Kaiser 2000) because of the power law shape of the electron energies which implies at higher p_1 the number of relativistic electrons decreases. Estimating number densities of relativistic electrons in galaxy clusters hosting radio-halos has been done using synchrotron power $P_{1.4}$ but the magnetic field has to be assumed (see e.g., Sarazin 1999, Blasi & Colafrancesco 1999). Figure 1.5 shows different plots of radio flux vs frequency of the Coma Cluster for different intracluster magnetic field.

Synchrotron emission from cosmic structures can also tell us information about the magnetic field that permeates the plasma hosted by these objects. The degree of linear polarization due to synchrotron emission for an electron population following a power law spectrum with index q is given by

$$\Pi(x) = \frac{q+1}{q+7/3}. \tag{1.5}$$

Usually the value of $\Pi(x)$ lies within 70% to 80% (Govoni & Feretti 2004) for typical spectral index q. This shows that radiation emitted via synchrotron emission from usual radio sources shows strong linear polarization. Since most of the radiation emitted by a charge particle are contained in the perpendicular polarization (see e.g., Longair 1993) to the magnetic field and are strongly beamed (within an angle of $2/\gamma_e$), this gives us an indication of the uniformity of the component of the magnetic field perpendicular to the line of sight. The value of the magnetic field can then be estimated by minimizing the total energy content of a given radio- source with respect to the magnetic field (see e.g., a review by Govoni & Feretti 2004). The different components that contribute to

the total energy are those coming from the relativistic particles (electrons and protrons) and from the magnetic field. The total energy can be written as

$$U_{tot} = U_p + U_e + U_B. \tag{1.6}$$

where U_p and U_e are the energies of the protons and electrons while U_B is the magnetic energy. In order to derive a quantitative estimation of the magnetic field, one has to invoke the assumption of equipartion of energy. This implies that the total energy is distributed approximately equal between the particles and the magnetic field. The minimum energy density corresponding to this configuration is written as

$$u_{min} = \frac{U_{tot}}{V\Phi} \propto \Phi^{-4/7} V^{-4/7} L_{syn}^{4/7}, \tag{1.7}$$

where Φ is the volume occupy by the magnetic field, V is volume of the cosmic structure and L_{syn} is the synchrotron luminosity.The magnetic field can then be written as

$$B = \left(\frac{24}{7}\pi u_{min}\right)^{1/2}. \tag{1.8}$$

The value of the magnetic field derived from this method is usually of order μG for values of q lying between 0.75-1.

Another evidence for the existence of large-scale magnetic fields in galaxy clusters is inferred through Faraday rotation measurements (see review by Govoni and Feretti 2004) of polarized radio emissions from sources found in the background of or embedded within the cluster. Faraday rotation effect is the rotation of the plane of polarization of a linearly polarized electromagetic beam when it passes through a plasma having a magnetic field component along the direction of propagration of the beam. The Faraday Rotation measure is given in practical units as

$$RM = 812 \int_0^L n_e \ [cm^{-3}] \ B_{||} \ [\mu G] \ dl \ [kpc] \ [rad/m^2]. \tag{1.9}$$

The integration is performed along the line of sight.The rotation measure is directly related to the parallel component of the magnetic field $B_{||}$ and the

number density n_e of the plasma. From X-ray observations the number density profile can be obtained and hence allowing the estimation of the component of the magnetic field along the line of sight. Typical values of the magnetic field using Faraday rotation measurements are found within 1-50 μ G (see a review by Carilli & Taylor 2001), especially in the central regions of galaxy clusters.

Cosmic rays

Galaxy clusters are observed in a wide range of frequencies, in X-ray, Optical, UV (see e.g., Lieu et al 1996a for soft X-ray detection in Coma and Virgo clusters of galaxies) as well as in radio (see the review by Govoni and Feretti 2004), and this has in turn shows that galaxy clusters are much more complex systems rather than just collections of thermal gas and dark matter over large cosmic distances. The detection of soft X-ray excess in non-cooling flow clusters (e.g. Coma cluster) by the EUEV (Extreme Ultraviolet Explorer) and the detection of hard X-ray excess in the cluster A2199 as well as in the Coma cluster (Fusco-Femiano et al. 1999) by the Beppo-SAX PDS (Phoswich Detertor system) (Kaastra, Blecker & Mewe 1998) are example of observations that could not be related to the thermal plasma component in these structures. These multi-frequency observations show that there are emissions in galaxy clusters which are of non-thermal origins. These origins of non-thermal emissions have been attributed to the existence of cosmic rays (relativistic electrons and protons) which are confined in these structures via cluster-scale magnetic fields. Models have been proposed to explain the origins of these cosmic rays and all these models rely on the existence of relativistic electrons. These electrons emit via synchrotron mechanism in the radio spectral region as well as by inverse Compton scattering of the CMB photons which are observable in the hard X-ray and gamma-ray spectral regions. In addition, other emission features like e.g. supra-thermal and relativistic bremsstrahlung can be also attributed to the presence of cosmic rays in the atmospheres of galaxy clusters (see Colafrancesco 2009 for a review).

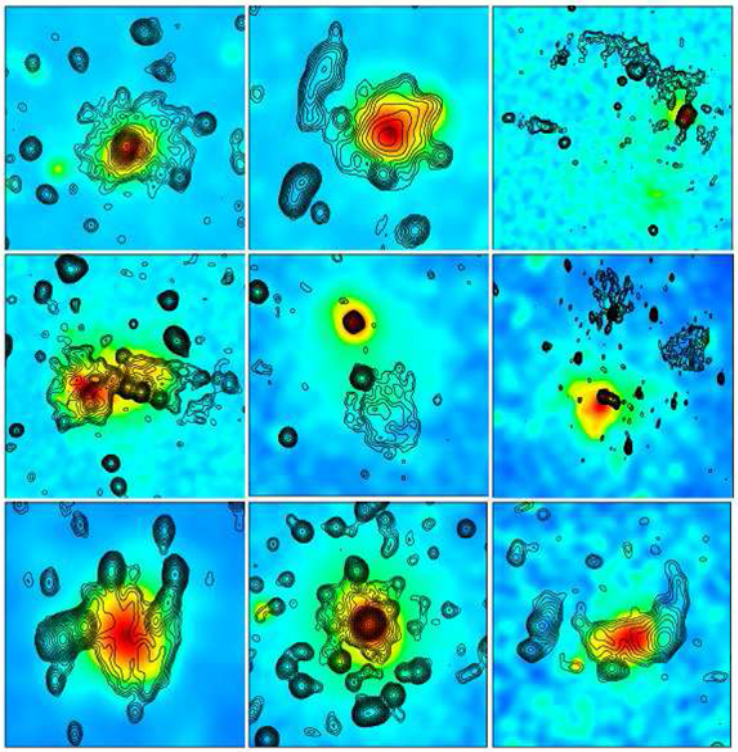

Figure 1.4: Diffuse radio emissions in galaxy clusters shown in contours overlaid on the X-ray emission shown in color. From top to bottom and left to right are A2219 (halo), A2744 (halo+relics), A115 (relic), A754 (complex, halo+relic), A1664 (relic), A548b (relic), A520 (halo), A2029 (mini-halo) and RXJCJ1314.4-2515 (halo+double relics) (Feretti et al. 2012).

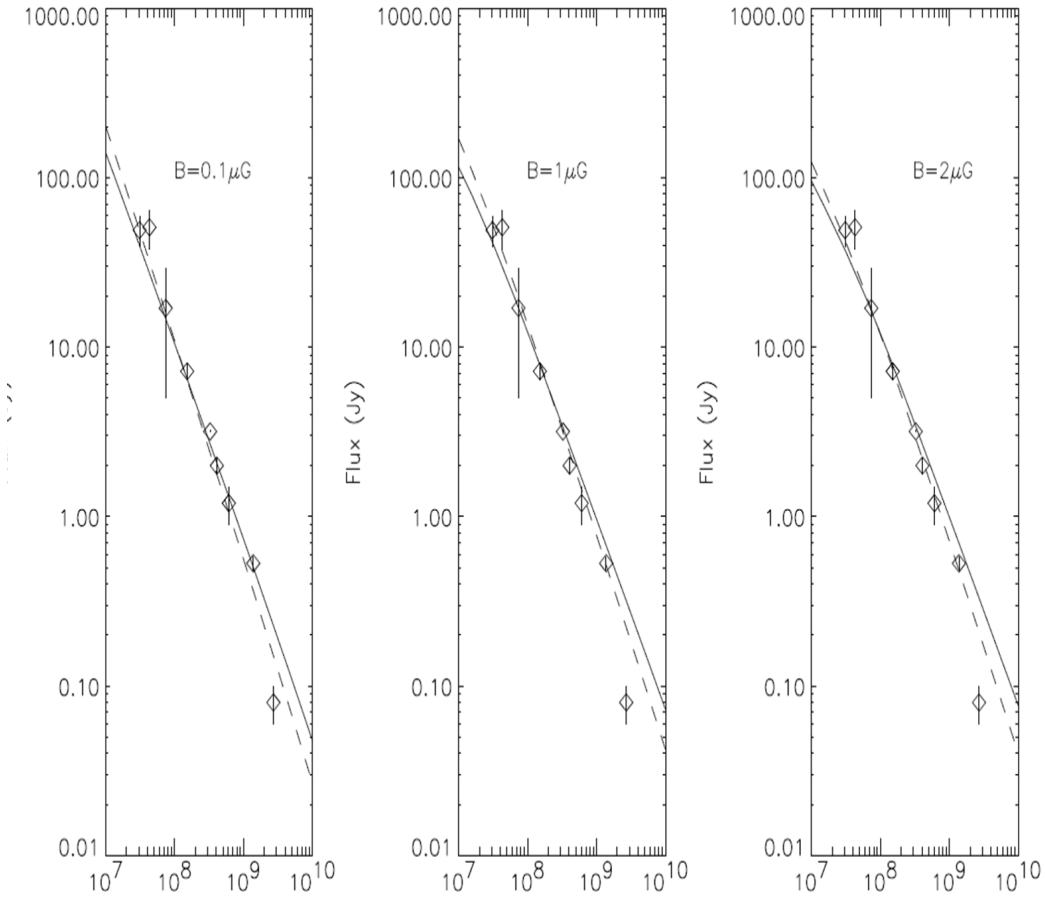

Figure 1.5: The radio flux vs frequency for the Coma Cluster for different intracluster medium magnetic field, B (Blasi & Colafrancesco (1999)).

The origin of these high energetic particles are explained within the framework of two distinct types of models:

1. Primary electron models or Leptonic models
2. Secondary electron models or Hadronic models.

Primary electron models rely on the existence of a population of relativistic electrons irrespective of their origins, which undergo acceleration at shocks during e.g. cluster mergers. The energy released during these events can be the order of 10^{64} ergs in a cosmic time scale of $\sim 1-2$ Gyrs (Roettiger, Burns & Stone 1999) and large-scale shock waves could be created during these processes. Diffusive shock acceleration together with the presence of a magnetic field are assumed to accelerate electrons to relativistic energies which are then expected to form large synchrotron emitting regions. Cosmological simulations (Miniati et al 2001) have shown that the radio power radiated, the polarization as well as the morphology predicted by the primary electron models are similar to those observed in radio-relics. Explaining radio-halos within this framework does not give satisfactory result due to the short life-time of these electrons, hence posing a problem for their propagations over large volumes $\approx$ Mpc^3, over which the diffuse radio emission are observed. In order to solve this problem, an efficient re-acceleration mechanism has been proposed to sustain the life time of these electrons a bit longer, $\approx$ 1 Gyr more. A more complex model involving two acceleration phases has also been proposed (Brunetti et al 2001) to try solving the lifetime and extension problems of radio diffuse emission in clusters. On the other hand secondary electron models rely on the continuous production of relativistic electrons via hadronic interactions (see e.g., Dennison (1980), Colafrancesco & Blasi (1998), Blasi & Colafrancesco 1999) of cosmic ray protons with thermal protons of the ICM. For example one hadronic interaction that produces relativistic electrons is between cosmic ray protons and the protons of the intracluster medium which produces charged pions as well as neutral ones. The charged pions then decay to produce secondary products among which are

charge muons, which can in turn decay to produce relativistic electrons.

$$\begin{aligned} p + p &\longrightarrow \Pi^{\pm} + X, \\ \Pi^{\pm} &\longrightarrow \mu^{\pm} \longrightarrow e^{\pm} + \bar{\nu_{\mu}}(\nu_{\mu}) + \nu_e(\bar{\nu_e}), \\ p + p &\longrightarrow \Pi^0 + X. \end{aligned} \tag{1.10}$$

In this model high energetic electrons are produced in-situ and hence do not need acceleration or re-acceleration mechanisms. In addition, protons have a long life-time and are able to propagate over large cosmic distances and at the same time supply relativistic electrons over Mpc^3 cosmic volume. These electrons then interact with the magnetic field present in the ICM to produce synchrotron emission, and with the CMB (and other backgrounds) to reduce inverse Compton scattering (ICS) emission at high energies.

Another scenario for interpreting the non-thermal emissions from galaxy clusters is through the annihilation of Dark Matter particles, namely neutralino-like (WIMP) particles (see e.g., Colafrancesco & Mele 2001, Colafrancesco, Profumo and Ullio 2006). Assuming that Dark Matter consists of WIMPs, then the annihilation of these particles will produce secondary particles like energetic electrons and positrons (the distinction is not important here) with energies around 10-100 GeV (up to the energy of the mother DM particle) in addition to other products (like, e.g., fermions, bosons etc). Then these energetic electrons will emit synchrotron radiation when they interact with the magnetic fields present in dark matter halos, like galaxy clusters, as well as ICS emission by interacting with the CMB (and other backgrounds) photons.

1.1.2 The Sunyaev Zel'dovich effect

The Sunyaev Zel'dovich effect (SZE) (Sunyaev & Zel'dovich 1972,see also the review by Birkinshaw 1999) is another observable emission feature in cosmic structures (e.g., galaxy clusters, radio-lobes). The SZE is the distortion of the CMB spectrum due to inverse Compton scattering of the CMB photons by electrons found in the plasmas hosted by these cosmic structures.

In addition to the thermal SZE produced by the thermal ICM electrons, other SZE of different origins can also be produced such as the non-thermal SZE (Colafrancesco et al. 2003, Ensslin & Kaiser 2000) produced by relativistic electrons in cluster radio-halos/relics or in the radio galaxy lobes (Colafrancesco 2008).Figure 1.6 shows the spectral distortions due to thermal (solid) and non-thermal SZE (dotted).

The SZE has been derived initially (Sunyaev and Zel'dovich 1972) using the Kompaneets (1957) equation and from this the distorted spectrum of the CMB is computed in the non-relativistic regime. The spectral distortion can be written in terms of the a-dimensional frequency, $x = h\nu/k_B T_0$ where T_0 is the CMB temperature ≈ 2.73 K , h the Planck constant and k_B is the Boltzmann constant. In the Kompaneets approximation, the distortion can be written as

$$\Delta I(x) = 2\frac{(k_B T_0)^3}{(hc)^2} y g(x), \tag{1.11}$$

where

$$g(x) = \frac{x^4 e^x}{(e^x - 1)^2}\big[x\frac{e^x + 1}{e^x - 1} - 4\big]. \tag{1.12}$$

The quantity y is the Compton parameter, which is the total pressure (thermal pressure + non-thermal pressure) of the cosmic atmosphere along a given line of sight, is written as follows

$$y = \int \frac{\sigma_T}{m_e c^2} n_e k_B T_e dl = \tau_e \frac{k_B T_e}{m_e c^2}, \tag{1.13}$$

where $\tau_e = \int \sigma_T n_e dl$, m_e is the mass of the electron and σ_T is the Thomson cross-section. Here the integration is performed along the line of sight. The Kompaneets equation produces correct result as long as y is small, implying low temperature for a given optical depth. Relativistic extension of the SZE has been performed by many authors (see Wright 1979 , Itoh et al. 1998, Challinor & Lasenby 1998, Colafrancesco et al. 2003) and in chapter 4 we are going to study the spectral distortion of the SZE in the relativistic regime. The component of the peculiar velocity along the line of sight of a cosmic structure (galaxy clusters, radio-lobes) can also induce a kinetic Sunyaev- Zel'dovich effect (kSZE) (Sunyaev & Zel'dovich 1980, Ensslin & Kaiser 2000, review by Birkinshaw 1999)

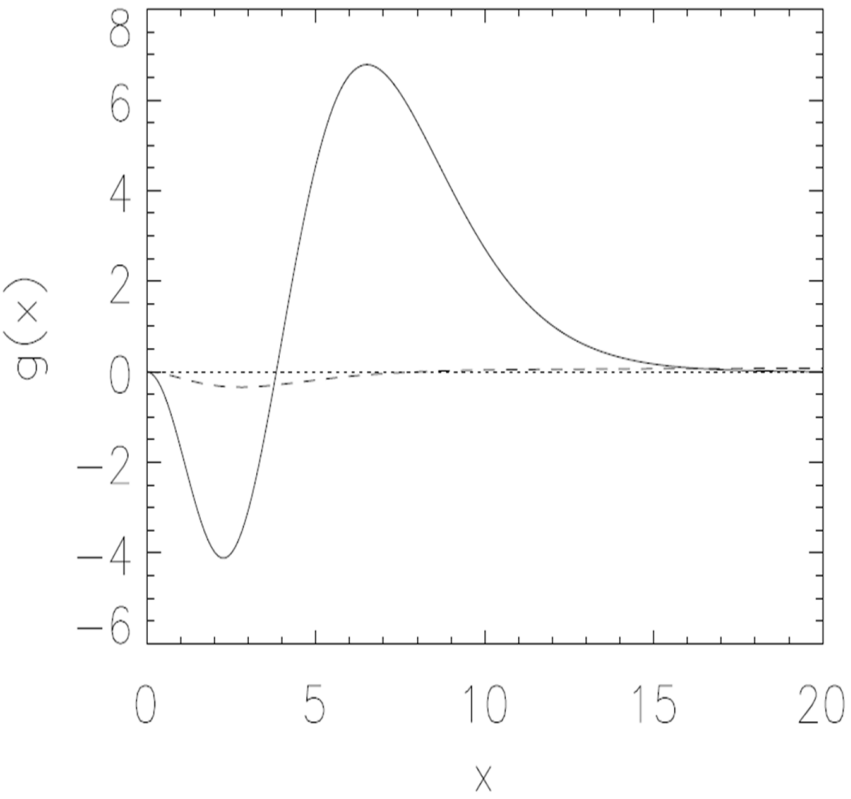

Figure 1.6: The spectral distortion function $g(x)$ for a thermal population of electrons in the Kompaneets approximation (solid curve) and the relativistic spectral distortion due to a non-thermal population of electrons (dotted-curve).

which is of the order of $\tau_e V_r/c$ where V_r is the bulk velocity of the cosmic structure along the line of sight which ranges between 500 km/s and 5000 km/s. The spectral distortion in this case is written, in a non-relativistic approach, as follows

$$\Delta I_{ksz} = 2\frac{(k_B T_0)^3}{(hc)^2}\beta_r \tau_e \frac{x^4 e^x}{(e^x-1)^2}, \tag{1.14}$$

and $\beta_r = V_r/c$. The kSZE allows in principle the determination of cosmic structure bulk velocity along the line of sight but measuring this distortion is

difficult since it is a small effect compare to the one induce by the random motion of the electrons.

In principle one can distinguish between the thermal SZE and the kSZE at the cross-over frequency of the thermal SZE, i.e. at $x_0 \approx 3.83$, as the former is zero at this point, leaving the kSZE "naked". The Kinetic SZE has been detected, at least statistically, if not for individual objects at high confidence (Hand et al. 2012).

1.1.3 Polarization of the Sunyaev Zel'dovich effect

Since the SZE is an interaction between electrons and photons, polarization is a natural outcome of this interaction. One of the first reason why polarizaton is expected is due to the primordial anisotropy of the CMB. Because of this anisotropy, Thomson's scattering by electrons found in cosmic structures is expected to produce polarization. Calculation of the generation of polarization in the SZ effect has been done by Sazanov, S.Y. & Sunyaev (1999) but it was achieved in a non-relativistic limit. Another computation of polarization in SZ effect was done by Challinor et al.(2000) where they conclude that the biggest contribution to polarization in SZ effect is due to the primordial multipoles of the CMB (in particular the quadrupole). Higher order contribution to the polarization of SZE has also been predicted. A bulk transverse velocity of the plasma will produce polarization pattern perpendicular to this transverse velocity ,$\propto \beta_T^2 \tau_e$, where β_T is the transverse peculiar velocity of the plasma. Another approximate contribution that can be mentioned here is the contribution of multiple scattering to the polarization, $\propto \left(k_B T_e / m_e c^2\right) \tau_e^2$. This polarization effect is caused due to the dependency of the optical depth τ_e on direction.

Relevance in cosmology and cosmic structures

One of the first discussed use of the SZE is to measure distance and hence the Hubble constant (see the reviews by Birkinshaw 1999, Carlstrom et al. 2002). This can be achieved by combining X-ray and SZE measurements by exploiting

the dependency of the X-ray emissivity ($\propto n_e T_e^{1/2}$) and the Compton parameter ($\propto n_e T_e$) on the number density of the plasma (Silk & White (1978), Ameglio et al. (2006)). One advantage of SZE over X-ray is that it is independent of redshift (see Carlstrom et al. 2002).

Recently the use of SZE has proven to be very useful in the studies of radio halos (see e.g., Basu 2012, Colafrancesco et al 2013) where a correlation between the Compton parameter and the power at 1.4 GHz is shown. The Compton parameter is linked to the total pressure (thermal+non-thermal) of the particles and radio power is connected to only the non-thermal pressure. Combination of both should allow the estimation of the magnetic field.

It has also been shown (Colafrancesco 2008, Colafrancesco et al. 2012) that a non-thermal SZE is expected from the lobes of radio galaxies, thus probing their leptonic and magnetic field structure. Combining Radio, Gamma and SZE measurements should allow to disentangle the relativistic electron distribution from that of the magnetic field.

Chapter 2

Theoretical modelling of galaxy clusters

Galaxy clusters are the largest virialized system in the Universe meaning that the virial theorem can be applied to them very well

$$E_k = -\frac{1}{2}E_p, \tag{2.1}$$

where E_k and E_p are the kinetic energy and potential energy of the system. The characteristic quantities that describe the galaxy cluster structure are defined in a simple self similar model (see Kaiser 1986 and also e.g., Colafrancesco and Vittorio 2004, Arnaud et al. 2010). By self similar we mean that for example a cluster of higher mass is just a scaled up version of a cluster of lower mass. Self-similarity relies on two assumptions: 1) clusters are formed via a single gravitational collapse at the observed redshift; 2) gravitational energy is the sole source of input energy. Within this framework the ICM of a galaxy cluster is treated as an ideal gas and based on that, quantities like mass, temperature, pressure etc can be defined. In this chapter we are going to see how these quantities are defined and it is a prerequisite for the next chapter where a study is performed on a set of galaxy clusters observed by the Planck Collaboration.

2.1 Galaxy cluster quantities and parameters

Galaxy clusters are over-density regions in the Universe that are gravitationally bound by the total enclosed mass of the structure within its physical volume. One defines a radius R_{500} given by

$$M_{500} = \frac{4}{3}\pi R_{500}^3 \times 500\rho_c(z), \tag{2.2}$$

where M_{500} is the mass enclosed in the radius R_{500} within which the mean density is 500 times the critical density ρ_c of the Universe at that redshift. The critical density at a redshift z is defined as:

$$\rho_c(z) = \frac{3H^2(z)}{8\pi G}. \tag{2.3}$$

Here $H(z)$ is the Hubble parameter given by $H(z) = H(0)[\Omega_M(1+z)^3 + \Omega_\Lambda]^{\frac{1}{2}}$ where G is the Newton's gravitational constant and $H(0)$ is the Hubble constant at redshift zero. Galaxy clusters represent the relative mass composition of baryonic matter to dark matter for the whole Universe because of their sizes. The density of the ICM can be written then as $\rho_g(r) = f_B\rho(r)$ where f_B is the baryonic fraction of the Universe, which is ≈ 0.175 (see Arnaud et al. 2010) and ρ is total density (baryonic and dark matter). Using this one can write down the characteristic electron number density as

$$n_e(r) = \frac{\rho_g(r)}{\mu_e m_p}, \tag{2.4}$$

where $\mu_e = 1.14$ is the mean molecular weight of the ICM gas per free electron. As we mentioned before galaxy clusters are virialized system and therefore applying the Virial theorem we obtain the temperature of the ICM gas as the following:

$$kT_{500} = \frac{\mu m_p G M_{500}}{2R_{500}}, \tag{2.5}$$

where $\mu = 0.59$ is the mean molecular weight of the ICM gas and m_p is the mass of the proton. The ICM is assumed to be in hydrostatic equilibrium with the pressure balancing gravity. The equation for hydrostatic equilibrium writes

as (see e.g., Ota & Mitsuda 2004):

$$\frac{k_B T}{\mu m_p}\left(\frac{d\ln\ \rho_g}{d\ln\ r}\ +\ \frac{d\ln\ T}{d\ln\ r}\right)\ =\ -\frac{GM(r)}{r}, \tag{2.6}$$

where $M(r)$ is the total mass enclosed in a radius r and ρ_g is density of the gas. In a simple β-model density profile $\rho_g(r) = \rho_{g,0}\left[1+\left(\frac{r}{r_c}\right)^2\right]^{-\frac{3\beta}{2}}$ where $\rho_{g,0}$ is the central gas density, r_c the core radius and β takes usually values $\sim 0.5-1$, the mean total density, $\bar{\rho}(r)$ inside a radius of r is given by

$$\bar{\rho}(r) = \frac{3M(r)}{4\pi r^3} = \frac{\rho_0}{1+(\frac{r}{r_c})^2}, \tag{2.7}$$

where $\rho_0 = \dfrac{9k_B T\beta}{4\pi G\mu m_p {r_c}^2}$ is the central total density of the cluster. From this one can write the central gas number density as

$$n_{e0,g} = \frac{f_B\rho_0}{\mu_e m_p}. \tag{2.8}$$

Then using 2.7 and 2.5 and writing $r_c = \lambda R_{500}$ one can cast the central gas number density as

$$n_{e0,g} = \frac{3\beta f_B 500\rho_c}{2\lambda^2\mu_e m_p}. \tag{2.9}$$

Several values of λ have been used by different authors (see, e.g., Bahcall 1995, Sarazin 1988, Dressler 1978) suggesting that for typical rich clusters the value of λ is in the range $0.1-0.25$. For X-ray clusters the value of λ can even go up to 0.3. We adopt here the value of $\lambda = 0.3$.

2.2 X-ray luminosity

As we have mentioned before the ICM is a hot gas with temperature $\approx 10^7$ K in which the dominant radiation mechanism is thermal bremsstrahlung and is observed in the X-ray region of the electromagnetic spectrum. We define the bolometric X-ray luminosity of the cluster ICM gas as follows:

$$L_{X,500} = 4\pi\lambda^3 C_2 T_{500}^{\frac{1}{2}} n_{e0,g}^2 R_{500}^3 W_1(\lambda), \tag{2.10}$$

where

$$W_1(\lambda) = \int_0^{\frac{1}{\lambda}} \left(1 + u^2\right)^{-3\beta} u^2 du. \tag{2.11}$$

Here $u = r/r_c$. This luminosity is the radiation emitted solely by the thermal content of the ICM.

2.3 Integrated Compton parameter

The spherical integrated Compton parameter is defined by:

$$Y_{sph,R} = \frac{\sigma_T}{m_e c^2} \int_0^R P_{tot}(r)\ dV. \tag{2.12}$$

Usuallly the radius R is most of the time R_{500} or $5R_{500}$ and at radius of $5R_{500}$ the spherical integrated Compton parameter is equal to the cylindrical integrated Compton parameter based on the computation by Arnaud et al. 2010. The Planck collaboration (2011) data of the integrated Compton parameter are computed over $5R_{500}$. Using the scaling relation of Arnaud et al (2010) one can write :

$$Y_{sph,R500} = \frac{I(1)}{I(5)}\ (Y_{SZ} D_A^2)\ _{5R500}, \tag{2.13}$$

where $I(1) = 0.6552$ and $I(5) = 1.1885$ (these values are given in the Appendix of Arnaud et al. 2010).

Chapter 3

Multifrequency constraints on non-thermal pressure in galaxy clusters

As mentioned previously, galaxy clusters show large scale radio emissions from the ICM and the origin of these radio halos is still an open problem.Various scenarios have been proposed that refer to primary electron models (Sarazin 1999, Miniati et al. 2001), re-acceleration models (see e.g., Blasi & Colafrancesco 1999, Miniati et al. 2001, Brunetti et al 2001) and also geometrical projection effect models (Skillman et al. 2012). All these models rely on the existence of a non-thermal population of electrons residing in the ICM and a large scale magnetic field that are spatially distributed in the cluster atmosphere. In this chapter we present the result of a multi-frequency study of the SZE in a sample of galaxy clusters hosting radio-halos (RHs clusters). From a combination of available X-ray, radio and SZE data of these clusters, we calculate the non-thermal pressure existing in these structures. We assume throughout the work a flat vacuum dominated Universe with $\Omega_m = 0.32$ and $\Omega_\Lambda = 0.68$ and $H_0 = 67.3$ km/(s Mpc). This part of the thesis has been accepted in A&A journal under

four authors. The bulk calculations and analysis behind the paper has been done by the present author under the guidance of his supervisor and relevant discussions has been added by the other two authors.

3.1 X-ray, radio and SZE data

The data for our work is a set of galaxy clusters that has combined X-ray, Radio and SZE observations and that are also RH clusters.The SZE and radio observations for our cluster list has been taken from the Planck collaboration (2011) and Brunetti et al. (2009) respectively while X-ray information has been taken from Reichert et al. 2011. In our present analysis, the most relevant quantities that we need are the Compton parameter, the radio power at 1.4 GHz and the bolometric X-ray luminosities. In order to satisfy the criteria of being RHs, we checked that the clusters also formed part of the list of RHs cluster compiled by Feretti et al.(2012). Information on the clusters velocity dispersion collected by Wu et al. (2009) and Zhang et al. (2011) have also been used.Specifically for the velocity dispersion of cluster A781, we had to consider the information provided by Cooke et al. (2012) and Geller et al. (2013). In appendix B we show the list of our chosen clusters.

3.2 $P_{1.4} - L_X$ and $Y_{SZ} D_A^2 - P_{1.4}$ and $Y_{sph,R500} - L_X$ correlations

A correlation, that can be fitted with a power law $P_{1.4} = P_0 L_X^d$, between the radio power at 1.4 GHz, $P_{1.4}$, due to synchrotron emission and the bolometric X-ray luminosity, L_X, due to thermal bremsstralung has been noticed in galaxy clusters hosting RHs (see Brunetti et al. 2009, Feretti et al. 2012). Since the power at 1.4 GHz is related to the non-thermal particle and magnetic field energy, $P_{1.4} \propto P_{non-th} U_B^{(\alpha+1)/4}$, and the bolometric X-ray luminosity is connected with the thermal content of the plasma, $L_X \propto n_e T^{1/2}$, this correlation implies

a link between non-thermal energy and thermal energy in RHs clusters. Another correlation exhibits by RHs clusters is between $P_{1.4}$ and the integrated Compton parameter Y_{SZ} (see Basu 2012). These two correlations ($P_{1.4} - L_X$ and $Y_{SZ}D_A^2 - P_{1.4}$) indicates a relation between the ICM thermal pressure and the non-thermal pressure implying a correlation be tween bolometric X-ray luminosity and Compton parameter which is actually noticed in the data. In

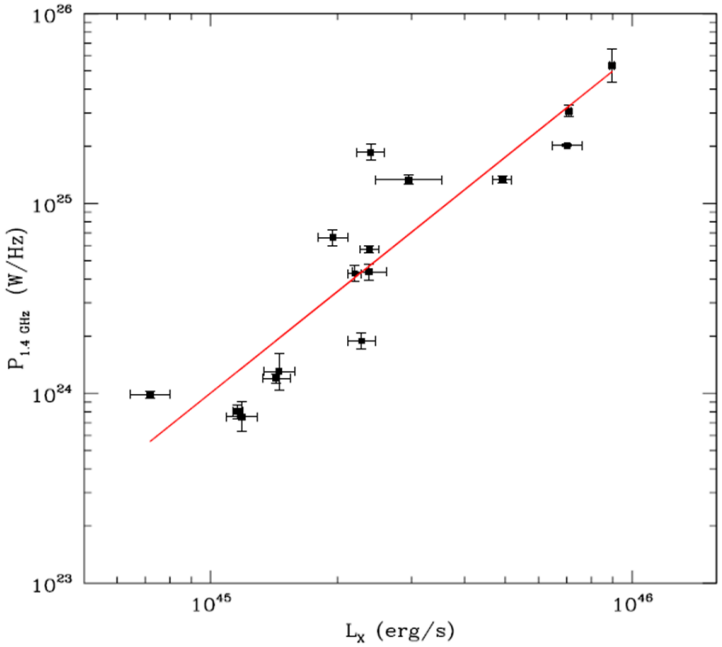

Figure 3.1: The fit between $P_{1.4}$ and L_X in log-log plane. Our result gives a normalization -56.04 ± 3.18 and slope of 1.78 ± 0.07 (Colafrancesco et al. 2013).

order to fit the $P_{1.4}$ – L_X, the $P_{1.4}$ – Y_{SZ} and the Y_{SZ} – L_x correlations, we have adopted the approach of Akritas and Bershady (1996) using the BCES estimator. According to this approach, in order to fit a straight line $y = mx + c$ to a data set, the slope and the intercept are given as follows:

$$m = \frac{\sum_{i=1}^{N}(x_i - \bar{x})(y_i - \bar{y}) - \sum_{i=1}^{N}\sigma_{y,i}\sigma_{x,i}}{\sum_{i=1}^{N}(x_i - \bar{x})^2 - \sum_{i=1}^{N}\sigma_{x,i}^2} \tag{3.1}$$

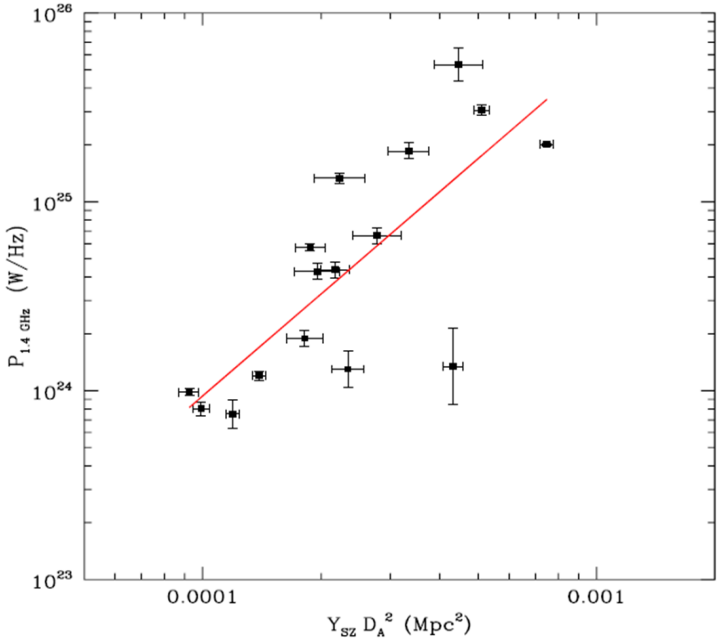

Figure 3.2: The fit between $P_{1.4}$ and $Y_{SZ}D_A^2$ in log-log plane. Our result gives a normalization 31.16 ± 0.36 and slope of 1.80 ± 0.10 (Colafrancesco et al. 2013).

and

$$c = \bar{y} - m\bar{x}, \tag{3.2}$$

where $\bar{x}$ is the mean of x and same for $\bar{y}$. $\sigma_{x,i}$ and $\sigma_{y,i}$ are the errors in x and y. A proper treatment of the error propagation shows that the variance in the slope and in the normalization of the best-fit line can be computed as follows

$$\sigma_m^2 = \sum_{j=1}^{N} \left(\frac{1}{W(y_j)} \left(\frac{\partial m}{\partial y_j} \right)^2 + \frac{1}{W(x_j)} \left(\frac{\partial m}{\partial x_j} \right)^2 \right), \tag{3.3}$$

$$\sigma_c^2 = \sum_{j=1}^{N} \left(\frac{1}{W(y_j)} \left(\frac{\partial c}{\partial y_j} \right)^2 + \frac{1}{W(x_j)} \left(\frac{\partial c}{\partial x_j} \right)^2 \right), \tag{3.4}$$

where σ_m^2 is the variance in the slope and σ_c^2 is the variance in the normalization and

$$W(x_i) = \frac{1}{\sigma_{x,i}^2}, \tag{3.5}$$

and

$$W(y_i) = \frac{1}{\sigma_{y,i}^2}. \tag{3.6}$$

In addition to the previous analysis of the variance in the slope and of the normalization, a further treatment is needed here to take into account the intrinsic scatter in the data. In order to estimate this intrinsic scatter we follow the method outline in Akritas and Bershady (1996) which summarize as follows:

$$R_i = y_i - c - mx_i, \tag{3.7}$$

where R_i is the residual. Then the intrinsic scatter σ_0^2 is estimated as follows:

$$\sigma_0^2 = \frac{\sum_{i=1}^{N}(R_i - \bar{R})^2 - \sum_{i=1}^{N}\sigma_{y,i}^2}{N-2}. \tag{3.8}$$

The χ^2 is then written as:

$$\chi^2 = \sum_{i=1}^{N} \frac{(y_i - mx_i - c)^2}{\sigma_{y_i}^2 + m^2\sigma_{x_i}^2 + \sigma_0^2}, \tag{3.9}$$

where $\sigma_{x_i}^2$ and $\sigma_{y_i}^2$ are the corresponding variances of x_i and y_i, respectively.

We show the results of the fit $P_{1.4} = C \cdot L_X^d$ and $P_{1.4} = B \cdot (Y_{SZ}D_A^2)^a$ in Figure 3.1 and Figure 3.2 respectively. Our analysis yields best-fit parameters $Log\ C = -56.04 \pm 3.18$ and $d = 1.78 \pm 0.07$, and also $Log\ B = 31.16 \pm 0.36$ and $a = 1.80 \pm 0.10$. The results obtained here are quite consistent with those obtained by Brunetti et al. (2009), where d was found to be in the range of $1.5 - 2.1$ and $Log\ C$ in the range -55.4 to -60.85, and with the analysis of Basu (2012), who obtained $Log\ B = 32.1 \pm 1$ and $a = 2.03 \pm 0.28$ for the Brunetti et al. (2009) RH sample.

The same data also exhibit a correlation between the Compton parameter $Y_{SZ}D_A^2$ and the X-ray bolometric luminosity L_X which is shown in Figure 3.3. Our analysis of this power-law correlation $Y_{SZ}D_A^2 = cL_X^m$ provides best fit slope of $m = 0.89 \pm 0.05$ and a normalization of $Log\ c = -44.11 \pm 2.23$.

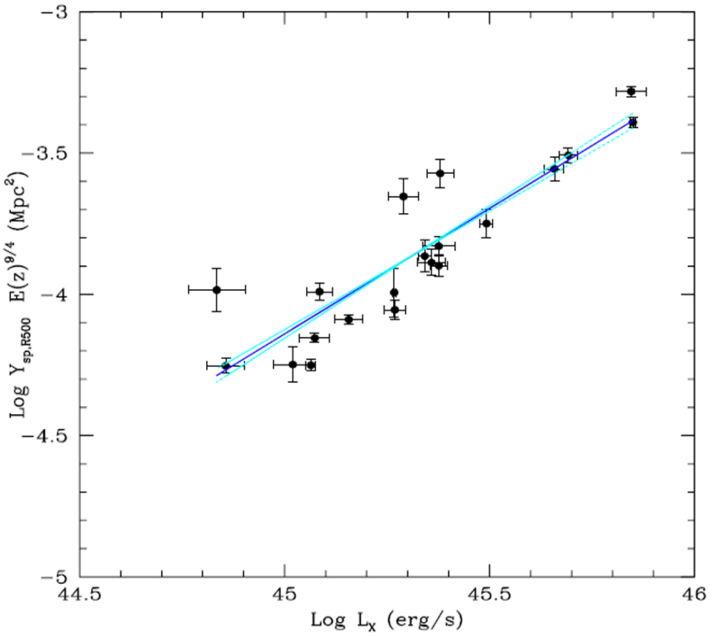

Figure 3.3: The fit between $Y_{sph,R500}E(z)^{9/4}$ and L_X in log-log plane. Our result gives a normalization -44.11 ± 2.23 and slope of 0.89 ± 0.05.

3.2.1 $Y_{SZ} - L_X$ relation

The Compton parameter is proportional to the total particle pressure provided by all the electron populations (thermal + non-thermal) in the cluster atmosphere. For the sake of generality we write here the total particle pressure P_{tot} as follows

$$P_{tot} = P_{th} + P_{non-th} = P_{th}(1 + X). \tag{3.10}$$

We write down then the Compton parameter

$$Y_{sph,R500} = \frac{\sigma_T}{m_e c^2} \int_0^{R_{500}} P_{th}(r) + P_{non-th}(r)\, dV = \frac{\sigma_T}{m_e c^2}(1+X) \int_0^{R_{500}} P_{th}(r)\, dV, \tag{3.11}$$

where

$$P_{th}(r) = k_B T_{500}\ n_{e0,g} \left[1 + \left(\frac{r}{r_c}\right)^2\right]^{-\frac{3\beta}{2}}. \tag{3.12}$$

Then one can write the relationship between $Y_{sph,R500}$ and L_X given by

$$Y_{sph,R500}E(z)^{9/4} = (1+X)J_1(\lambda)\left[\frac{L_X}{J_2(\lambda)}\right]^{5/4}, \tag{3.13}$$

where

$$J_1(\lambda) = \frac{4000\pi^2}{3}\frac{\sigma}{m_e c^2} \times G\mu m_p \rho_c n_{e0,g}\lambda^3 V_1(\lambda). \tag{3.14}$$

and

$$J_2(\lambda) = 4\pi C_2\left(\frac{2\pi}{3k_B}G\mu m_p 500\rho_c\right)^{\frac{1}{2}} \times n_{e0,g}^2\lambda^3 W_1(\lambda). \tag{3.15}$$

The theoretical prediction for a constant value of $X = 0.55 \pm 0.05$ is shown

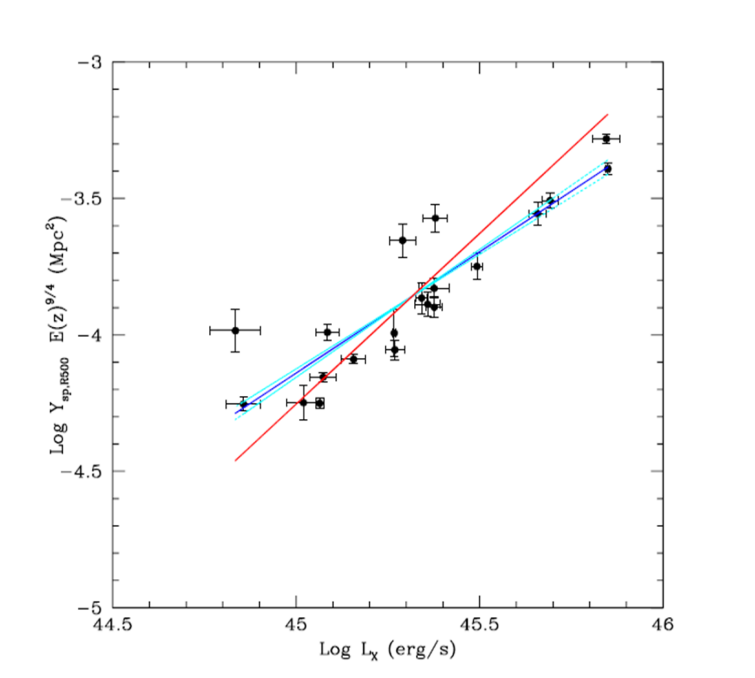

Figure 3.4: The fit between $Y_{sph,R500}E(z)^{9/4}$ and L_X in log-log plane (Red) and the beta model (green) for $\beta = 2/3$ and $\lambda = 0.3$. A value of $X = 0.55 \pm 0.05$ is obtained (Colafrancesco et al. 2013).

in Fig.3.4 together with the best-fit correlation of the data. We stress that the theoretical curve calculated under these assumptions is sensitively steeper

than the power-law best-fit to the data. This is the result of having assumed a constant value of X for all cluster X-ray luminosities in our model.

3.2.2 Evolution of the non-thermal pressure with X-ray luminosity

A decreasing value of X with the X-ray luminosity (or with the Compton parameter) as $X \sim L_X^{-\xi}$ can alleviate the problem providing a better agreement between the cluster formation scenario and the non-thermal phenomena in RH clusters. In order to analyze this point, we compute the value of X for each individual cluster in our sample by using the relationship between the Compton parameter and the X-ray bolometric luminosity given above (eq 3.13). Table 3.1 reports the values of X calculated for the considered clusters assuming the previous β-model. For some clusters the value of X is negative and we did not consider their value of X for these clusters. The reason for the negative value

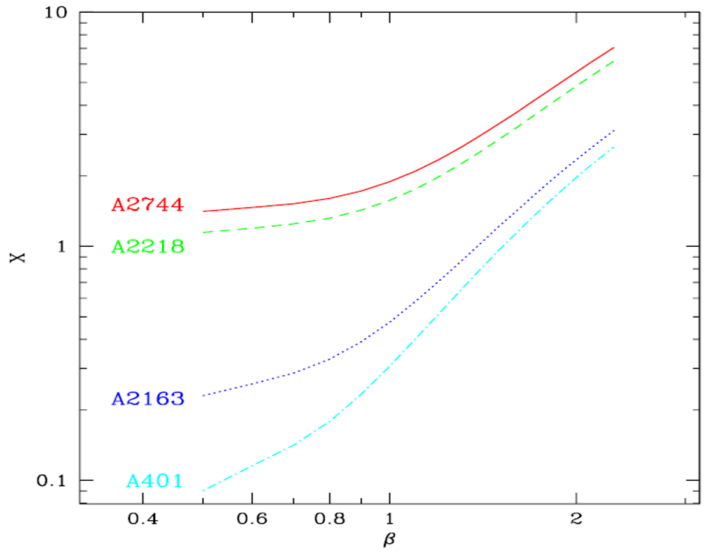

Figure 3.5: The variation of the non-thermal pressure ratio X with β (Colafrancesco et al. 2013).

of X for these clusters can be attributed to the fact that we assumed $\lambda = 0.3$ which is constant for all the clusters. In our formalism the value of X decreases with increasing core radius (increasing λ) and increases with increasing value of central particle density. We show the variation of X with β and λ in Figure 3.5 and Figure 3.6 respectively. We compute the errors in X using

$$\Delta X^2 = \left(\frac{\partial X}{\partial L_X}\Delta L_X\right)^2 + \left(\frac{\partial X}{\partial Y_{sph,R500}}\Delta Y_{sph,R500}\right)^2 \tag{3.16}$$

Fig 3.7 shows the correlation of the values of X with both the Compton parameter and with the bolometric X-ray luminosity of each cluster. The data and our estimate for X show that there is a clear decreasing trend of the pressure ratio X with both the cluster X-ray luminosity and with the integrated Compton parameter indicating that low-L_X (mass) cluster hosting RHs require a larger ratio of the non-thermal to thermal pressure ratio. We fit the $X - L_X$ relation

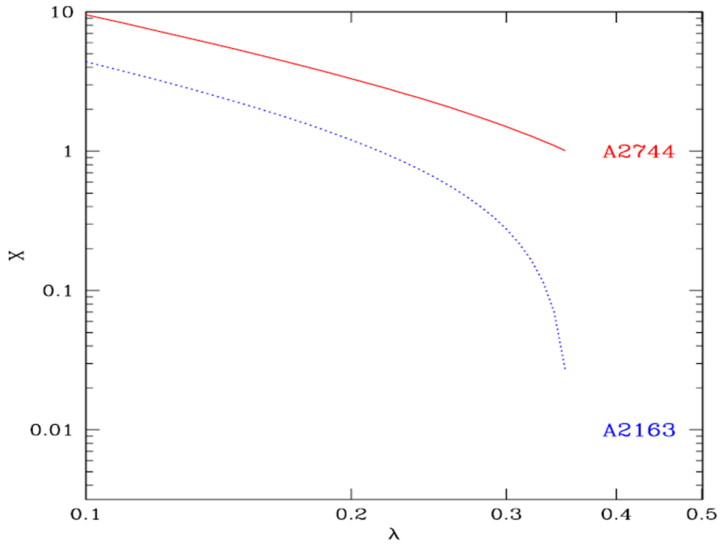

Figure 3.6: The variation of the non-thermal pressure ratio X with λ (Colafrancesco et al. 2013).

Table 3.1: Clusters name and their corresponding calculated X parameters (Colafrancesco et al. 2013).

Cluster	X (β-model)
1ES0657	0.16
RXCJ2003	-
A2744	7.17
A2163	0.61
A1300	2.03
A0665	0.33
A773	0.41
A2256	1.33
Coma	0.322
A0520	0.50
A209	-
A754	0.478
A401	0.349
A697	0.140
A781	3.07
A1995	0.61
A2034	0.52
A2218	3.79
A1689	0.42
MACSJ0717	-
A1914	0.13
A2219	0.21
A2255	1.65

by assuming a power-law form

$$X = Q \cdot L_X^{-\xi}, \tag{3.17}$$

and we obtain best fit values of $\xi = 0.96 \pm 0.16$ and $Log\ Q = 43.49 \pm 7.09$. The best fit curve with these parameters is also shown in Fig 3.7. We then calculate our theoretical prediction for the $Y_{sph,R500} - L_X$ relation using the previous $X \propto L_X^{-\xi}$ relation and we find indeed a better agreement of the cluster formation model with the available data for our sample of RH clusters. (see Figure 3.8). This last result indicates that the existence of a non-thermal pressure in RH clusters with a ratio $X = P_{non-th}/P_{th}$ that decreases with cluster X-ray luminosity (or mass) is able to recover the consistency between the theoretical model for cluster formation and the presence of RHs in clusters.

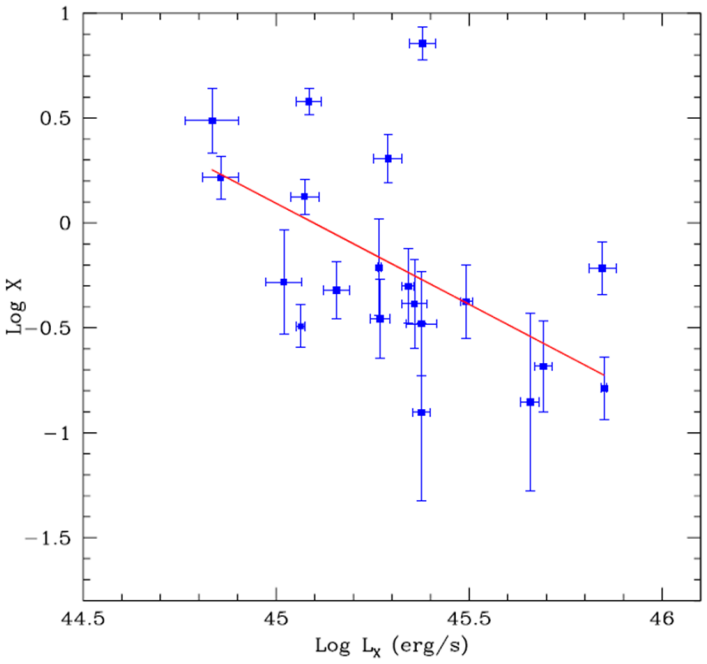

Figure 3.7: The fit to the X-L_X data. We obtain a normalization 43.49 ± 7.09 and slope -0.96 ± 0.16 (Colafrancesco et al. 2013).

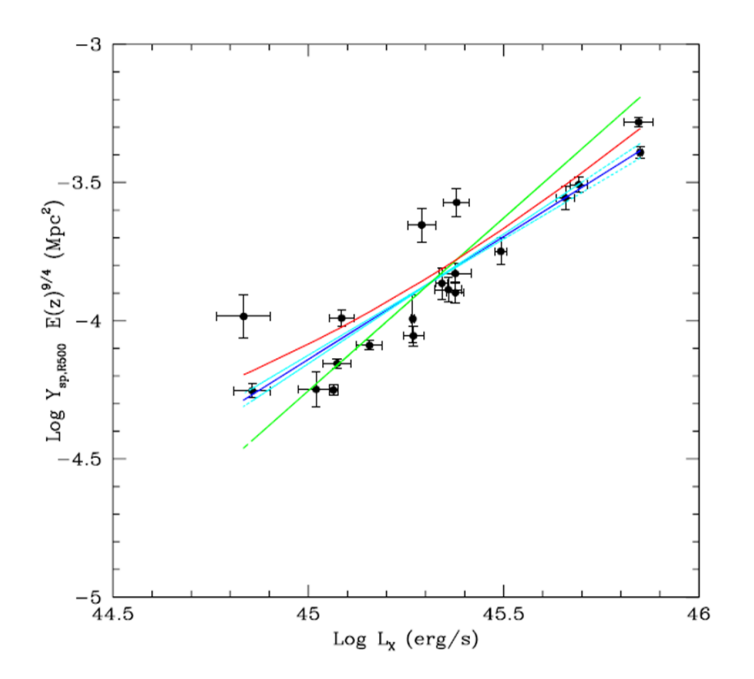

Figure 3.8: We show here the best fit (green) to the data together with the constant non-thermal (violet) and that of the one decreasing with luminosity (blue) (Colafrancesco et al. 2013).

3.3 Results

The results presented are quite independent on our assumptions of the cluster structural properties.Specifically, the slope of the $Y_{sph,R500} - L_X$ relation does not depend on the detailed shape of the cluster density profile, and hence the condition $X \sim L_X^{-0.96}$ seems quite robust. However, the absolute value of the pressure ratio X for each cluster depends on the assumed density profile and on the simplifying assumption that the non-thermal electron distribution resembles the thermal ICM one. It might be considered, in general, that the non-thermal and thermal particle density radial distributions are correlated as $n_{e,non-th}(r) \propto [n_{e,th}(r)]^{\alpha}$, and previous studies (see Colafrancesco and Marchegiani 2008) showed that the values of α do not strongly deviate

from 1, thus rendering our assumption reasonable and our result robust.

3.4 Implications of the existence of a non-thermal pressure in galaxy clusters

We found evidence that the largest available sample of RH clusters with combined radio, X-ray and SZE data require a substantial non-thermal particle pressure to sustain their diffuse radio emission and to be consistent with the SZE and X-ray data. This result has been derived mainly from the $Y_{sph,R500} - L_X$ relation for a sample of RH clusters selected from the Planck SZ effect survey. This non-thermal particle (electron and positron) pressure affects in particular the value of the total Compton parameter $Y_{sph,R500}$ within R_{500} indicating an integrated Compton parameter that is a factor $\sim 0.55 \pm 0.05$ (on average) larger that the one induced by the thermal ICM alone. The shape of the $Y_{sph,R500} - L_X$ does not depend on the assumptions on the cluster parameters and density profiles, while its normalization (and therefore the value of X) depend on the cluster parameters. Specifically, the value of X decreases with increasing cluster core radius (or increasing value of λ) and increases with increasing value of the central particle density. Therefore, the normalization of the previous correlation, and consequently the best-fit value of X, are affected by the cluster structural parameters. Detailed studies of the values of X derived from the previous correlation could be then used as barometric probes of the structure of cluster atmospheres. However, one of the most important results we obtained in this work is that the simple description in which X is constant for every cluster fails to reproduce the observed $Y_{sph,R500} - L_X$ relation, requiring that $X \sim L_X^{-0.96 \pm 0.16}$. We hence found that the impact of the non-thermal particle pressure is larger (in a relative sense) in low-L_X RH clusters than in high-L_X RH clusters, requiring a luminosity evolution of the pressure ratio $X \sim L_X^{-\xi}$ with $\xi \approx 0.96 \pm 0.16$. We note, in fact, that without this luminosity evolution the theoretical model for the $Y_{sphR500} - L_X$ correlation predicts a steeper relation

compare to the best-fit one which is considerably flatter. A decreasing value of X with the X-ray luminosity can therefore provide a better agreement between the cluster formation scenario and the presence of non-thermal phenomena in RH clusters. This behavior can be attributed to the decreasing impact of the non-gravitational processes in clusters going from low to high values of L_X.

3.5 Discussion

The positive values of X found in our cluster analysis indicates the presence of a considerable non-thermal pressure provided by the non-thermal electrons (and positrons): the presence of non-thermal electrons (positrons) is the minimal particle energy density requirement because it has been derived from SZE measurements (i.e. by Compton scattering of CMB photons off high-energy electrons, and positrons). For a complete understanding of the overall cluster pressure structure one should also consider the additional contribution of non-thermal proton that is higher than the electron one since protons loose energy on a much longer time scale. Therefore, the derived values of X should be considered as lower limits to the actual total non-thermal pressure and this will point to the presence of a relatively light non-thermal plasma in cluster atmospheres. A full understanding of the proton energy density (pressure) in cluster atmospheres could be obtained by future gamma-ray observations (or limits) of these galaxy clusters with RHs because the gamma-ray emission could possibly be produced by $\pi^0 \rightarrow \gamma + \gamma$ decays where the neutral pions π^0 are the messengers of the presence of hadrons (protons) in cluster atmospheres (see, e.g., Colafrancesco & Blasi 1998, Colafrancesco & Marchegiani 2008 and references therein).

Chapter 4

The relativistic SZ effect

In this chapter, we introduce relativistic effect in the SZE. To compute the SZ effect in a relativistic formulation, there are various approaches which have been used by several authors, but the two most consistent ones are described below and they are going to be the ones related to our work. The relativistic SZ effect can be computed:

i) using the scattering probability derived by Chandrasekhar. This method is coined Wright's method by Nozawa & Kohyama (2009a). It has been used by many authors such as Colafrancesco et al. (2003), Birkinshaw (1999) etc. to compute the SZ effect in the Thomson approximation. In this approach one calculate the frequency redistribution function in the electron rest frame;

ii) by solving the collision integral of the covariant Boltzmann equation for the photon distribution function. This method is coined the Covariant formalism by Nozawa & Kohyama (2009a).

It has been shown by Nozawa & Kohyama (2009a) that both methods give the same result in the Thomson approximation. The second one has an advantage over the first one not only because it can compute SZ effect outside the Thomson regime but that it also allows one to compute polarization in SZ effect in a covariant way very easily. This has been shown by Portsmouth and Bertschinger (2004b). In this present chapter we are going to study the SZ effect using the

first method and then in the next chapter we are going to use the second method to include polarization. For completeness we also show that both methods are equivalent in the Thomson regime.

4.1 Thomson scattering in the SZ effect

Even though the Inverse Compton effect is usually associated with the Sunyaev Zel'dovich effect but for low frequency analysis which is very ideal to study the CMB radiation, the process can be described using Thomson scattering in the rest frame of the electron (pointed out by e.g., Birkinshaw 2000). This is valid for non-relativistic electrons as well as very highly relativistic electrons as pointed out by Nozawa and Kohyama (2009). The Thomson limit is written as follows:

$$\gamma_e h\nu \ll m_e c^2. \tag{4.1}$$

The geometry of the interaction between the CMB photon and the electron is shown in Fig 4.1 and we are working in the electron's rest frame. In the Thomson limit the momentum of the incident photon p_1 is equal to the momentum of the scattered photon p_2. The differential Thomson cross-section is written as

$$\frac{d\sigma}{d\Omega} = \frac{r_e^2}{2}\big(1 + \cos^2\psi\big), \tag{4.2}$$

where r_e is the electron radius and ψ is the angle between the unit vector in the direction of p_1 and the unit vector in the direction of p_2. The probability of a photon coming from an angle $d\theta$ around θ and collide with the electron is

$$p_{in}(\mu)d\mu = \frac{d\mu}{2\gamma_e^4\big(1-\beta_e\mu\big)^3}. \tag{4.3}$$

We have define here $\mu = \cos\theta$ and $\mu' = \cos\theta'$. The probability for the photon to be scattered into $d\theta'$ around θ' is given by

$$p_{out}\big(\mu,\mu'\big)d\mu' = \frac{3}{8}\big[1 + \mu^2\mu'^2 + \frac{1}{2}(1-\mu^2)(1-\mu'^2)\big]. \tag{4.4}$$

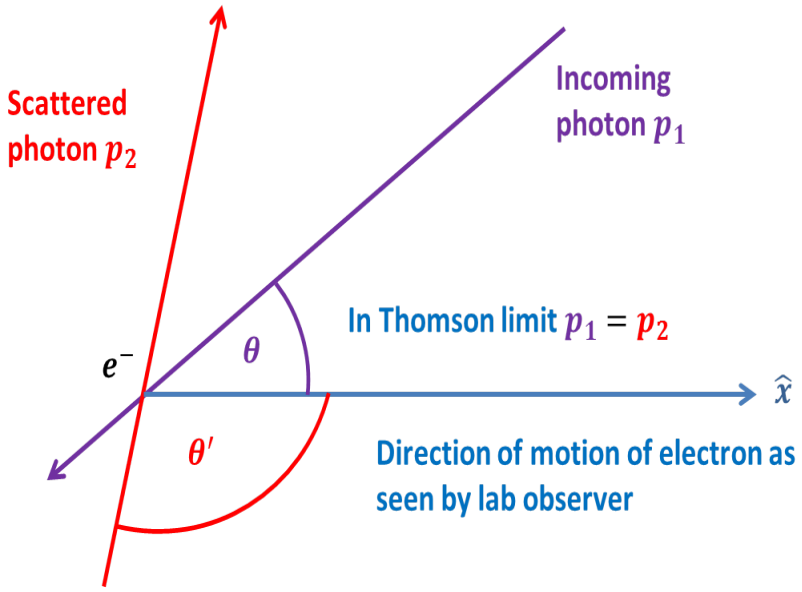

Figure 4.1: Scattering geometry in the rest frame of the electron.

Then the probability to have a shift s due to a photon coming from $d\theta$ around θ and being scattered by an electron into $d\theta'$ around θ' is given by

$$\begin{aligned} P(s,\beta_e)ds &= ds\int_{\mu_{down}}^{\mu_{up}} p_{out}(\mu,\mu')p_{in}(\mu)\frac{d\mu'}{ds}d\mu = \\ &= 3e^s ds\int_{\mu_{down}}^{\mu_{up}} \frac{\beta_e^2(3-\mu^2)-(1-3\mu^2)\left[1-e^s(1-e^s(1-\beta_e\mu)\right]^2}{32\beta_e^3\gamma_e^4(1-\beta_e\mu)^2}\,d\mu, \end{aligned} \tag{4.5}$$

where

$$e^s = \frac{\nu'}{\nu} = \frac{1-\beta_e\cos\theta'}{1-\beta_e\cos\theta} = \frac{1-\beta_e\mu'}{1-\beta_e\mu}, \tag{4.6}$$

and ν' and ν are the frequency measured in the lab frame and not in the rest frame of the electron, and

$$\mu' = \frac{1-e^s(1-\beta_e\mu)}{\beta_e}. \tag{4.7}$$

The limit of the integration namely μ_{down} and μ_{up} can be written as follows

$$\mu_{down} = \begin{cases} -1 & s \leq 0 \\ \dfrac{1 - e^s(1+\beta_e)}{\beta_e} & s \geq 0 \end{cases} \tag{4.8}$$

$$\mu_{up} = \begin{cases} \dfrac{1 - e^s(1-\beta_e)}{\beta_e} & s \leq 0 \\ 1 & s \geq 0. \end{cases} \tag{4.9}$$

After computing the integration one obtains the following analytical solution by defining $p_e = \gamma_e \beta_e$ which is the normalized momentum

$$P\big(s, p_e\big) = \frac{3(1+e^s)e^s}{8p_e^5}\left[\frac{3 + 3p_e^2 + p_e^4}{\sqrt{1+p_e^2}} - \frac{3+2p_e^2}{2p_e}\big(2\sinh^{-1} p_e - |s|\big)\right] + \\ -\frac{3\big|1-e^s\big|}{32p_e^6}\Big[1 + \big(10 + 8p_e^2 + 4p_e^4\big)e^s + e^{2s}\Big]. \tag{4.10}$$

4.2 Scattering Kernel

In order to compute the change in the intensity of the radiation, one needs to compute the probability to have a shift s from a momemtum/velocity distribution of electrons. For photons that have been scattered once this is done by averaging over the electron momentum distribution function as follows:

$$P_1\big(s\big) = \int_{p_{min}}^{\infty} P\big(s, p_e\big) f_e\big(p_e\big)\ dp_e. \tag{4.11}$$

This is called the single scattering limit. This is true if the optical depth of the plasma is small. The function $P_1\big(s\big)$ may or may not have an analytical form depending on the momentum distribution of the electrons. p_{min} is the minimum momentum needed to give rise to a shift s. One interesting feature of the function $P_1\big(s\big)$ is the following:

$$P_1\big(-s\big) = e^{-3s} P_1\big(s\big). \tag{4.12}$$

4.2.1 Thermal electrons

This electron population is the one responsible for the high X-ray emission due to thermal bremsstrahlung. The distribution function for this type of electron distribution is written as follows (see e.g., Ensslin and Kaiser 2000)

$$f_e(p) = \frac{\beta_{th}}{K_2(\beta_{th})} p_e^2 e^{-\beta_{th}\sqrt{1+p_e^2}}, \tag{4.13}$$

where $\beta_{th} = m_e c^2/k_B T_e$ and $K_2(\beta_{th})$ is the modified Bessel function of the second kind.The minimum momentum $p_e = p_{min}$ needed to give rise to a shift s in this case is given by $p_{min} = \sinh(\big|s\big|/2)$. In computing the SZE for this type of population we use an optical depth value of 0.01.

4.2.2 Non-thermal electrons

This type of electron population are those suspected for the synchrotron emissions and IC emissions in galaxy clusters as well as in lobes of radio galaxies. The momentum distribution of these electrons follows as

$$f_e(p_e) = A(p_1, p_2, \alpha) p_e^{-\alpha}. \tag{4.14}$$

The normalization $A(p_1, p_2, \alpha)$ is given by:

$$A(p_1, p_2, \alpha) = \frac{\alpha - 1}{p_1^{1-\alpha} - p_2^{1-\alpha}}. \tag{4.15}$$

Usually $\alpha = 2.5$ is the most common value which is consistent with observations and the momentum p_2 is taken to be infinity. The momentum p_1 sets the normalization and the number density which in turn sets the optical depth (see Colafrancesco et al. 2003). The minimum momentum $p_e = p_{min}$ needed to give rise to a shift s in this case is given by $p_{min} = \mathrm{MAX}\big(p_1, \sinh(\big|s\big|/2)\big)$. The number density of non-thermal electrons decreases with increasing value of p_1. The number density can be written as follows

$$n_{e,rel}(p_1) = \frac{n_{e,rel}(\bar{p_1}) A(\bar{p_1})}{A(p_1)}, \tag{4.16}$$

where we fixed $\bar{p_1} = 100$ and $n_{e,rel}(\bar{p_1}) = 1 \times 10^{-6}$ cm^{-3}. The optical depth can then be written as

$$\tau_{rel}(p_1) = 2 \times 10^{-6} \frac{A(\bar{p_1})}{A(p_1)} \left[\frac{n_{e,rel}(\bar{p_1} = 100)}{10^{-6} \text{ cm}^{-3}} \right] \frac{l}{\text{Mpc}}. \tag{4.17}$$

In this work we use $l = 1$ Mpc. Table 4.1 gives the corresponding values of τ_{rel} for different minimum momentum p_1. We show the redistribution function $P_1(s)$ for a thermal and non-thermal population of electrons in Figure 4.2 and 4.3.

Table 4.1: Minimum momentum p_1 and the optical depth τ_{rel}

Minimum momentum p_1	Optical depth τ_{rel}
0.5	0.0057
1	0.002
3	0.0004

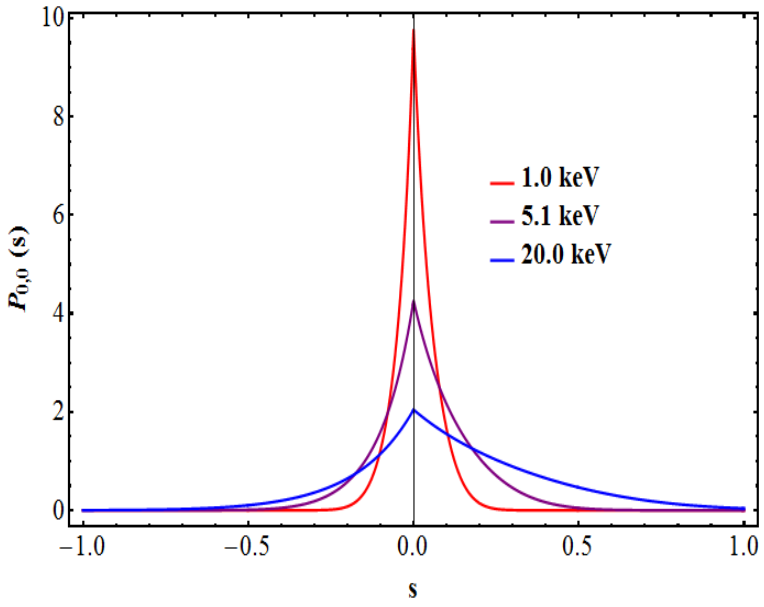

Figure 4.2: The scattering kernel for a thermal electron distribution $P_1(s)$ at different temperatures.

4.3 The spectrum of the SZ effect

We compute here the change in intensity for two electron populations, one for thermal and one for non-thermal. The change in intensity for an incident isotropic radiation (Planck spectrum) in the Thomson limit for any electron population is calculated as follows:

$$\Delta I(x) = \frac{2(kT_0)^3}{(hc)^2}\tau_e \int_{-\infty}^{\infty} P_1(s)\left[I_0(xe^{-s}) - I_0(x)\right]ds. \tag{4.18}$$

The change in intensity for a thermal electron population is shown in Fig 4.4. We see that the SZ effect in relativistic formalism depends on the plasma parameters such as temperature and it does show a distinct feature for different temperatures. This is the change in intensity in the single-scattering limit that is for a low optical depth plasma which is quite valid in many astrophysical media. Fig 4.5 shows the change in intensity for a non-thermal electron popu-

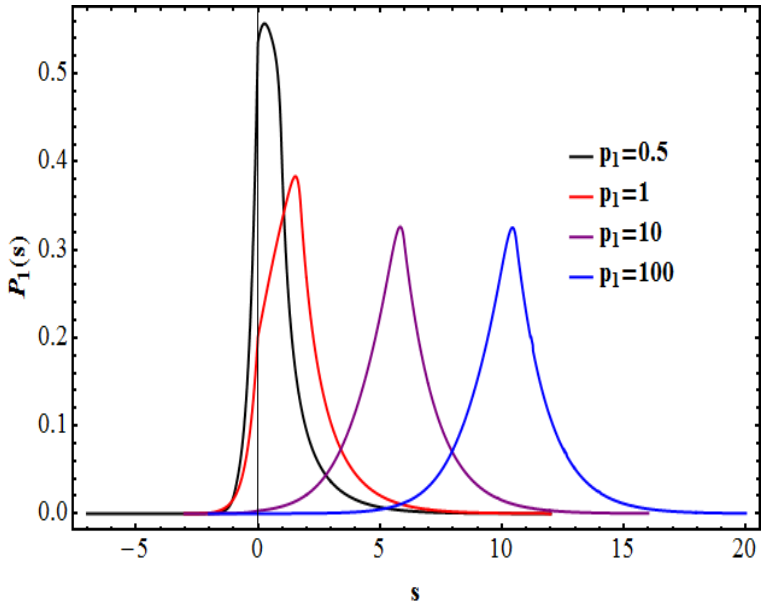

Figure 4.3: The scattering kernel for a non thermal electron distribution $P_1(s)$ for different minimum momentum p_1.

lation. One can see that the shifts are much bigger, meaning the photons are scattered into the high frequency regimes. One can also note the difference of the non-thermal spectrum and the thermal spectrum. This helps in distinguishing plasmas present in cosmic structures very easily.

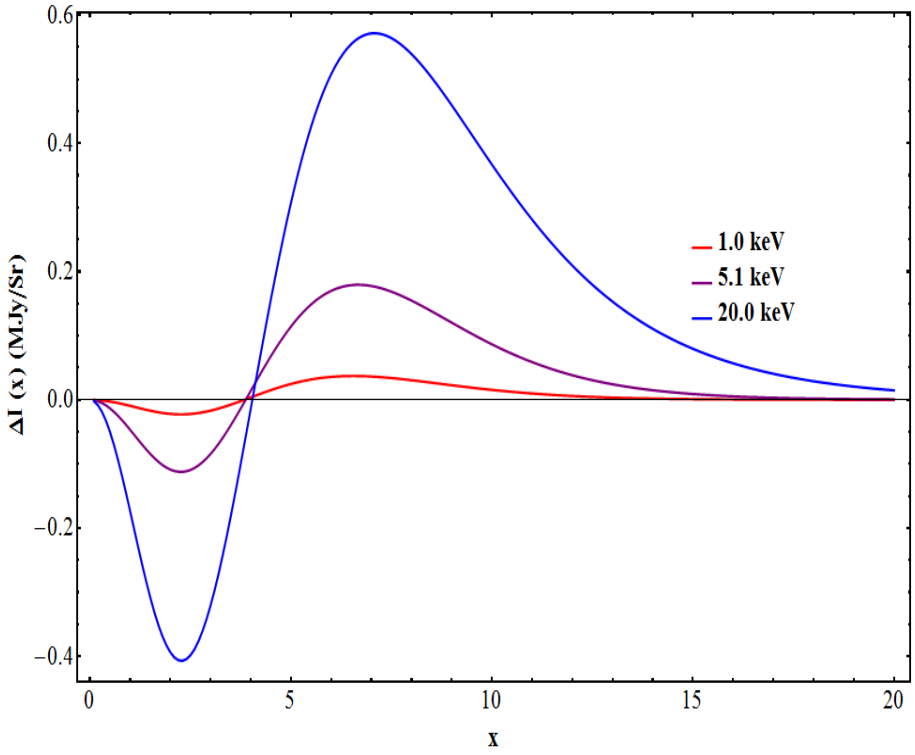

Figure 4.4: The change in intensity for an isotropic incident radiation for different plasma temperatures.

4.3.1 Full scattering kernel $P(s)$

Although the analysis so far is good but it applies for thin plasma and very often in astrophysical systems we do have situations, even though very rare, where the plasma is optically thick and this make the analysis above not accurate (see Colafrancesco et al. 2003). A CMB photon may be scattered several times 1, 2 or 3 and some even more. So one need to take into account this effect when computing the SZ effect in cases where the optical depth is thick, for example at the center of Radio galaxies. The full scattering kernel writes as follows (see Colafrancesco et al. 2003):

$$P(s) = e^{-\tau_e}\left[\delta(s) + \tau_e P_1(s) + \frac{\tau_e^2}{2!}P_2(s) + \frac{\tau_e^3}{3!}P_3(s) + ...\right], \qquad (4.19)$$

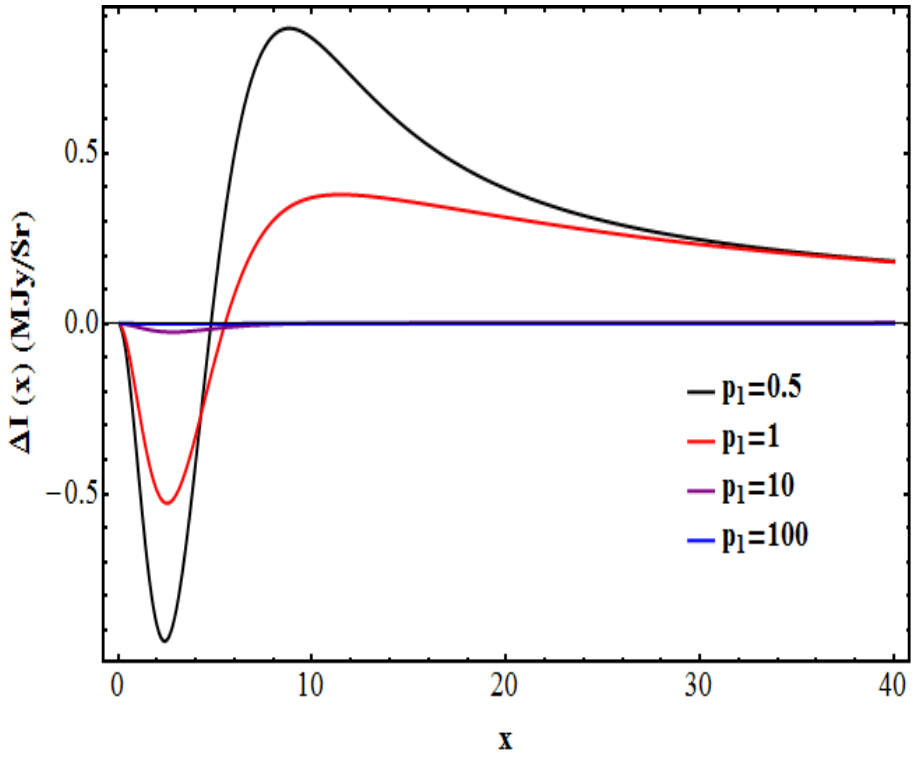

Figure 4.5: The change in intensity for an isotropic incident radiation for different minimum momentum p_1 for a single power law electron distribution.

where

$$P_n(s) = P_1(s) \star ... \star P_1(s), \tag{4.20}$$

and $\star$ is the convolution operation.

The change in the spectrum is computed as follows

$$\Delta I(x) = \frac{2(kT_0)^3}{(hc)^2} \int_{-\infty}^{\infty} P(s) \left[I_0(xe^{-s}) - I_0(x) \right]. \tag{4.21}$$

Using the full scattering kernel $P(s)$ one can compute the change in intensity up to any order of the optical depth τ. The optical depth is related to the number density of the plasma and this shows that the SZ effect can be used to probe

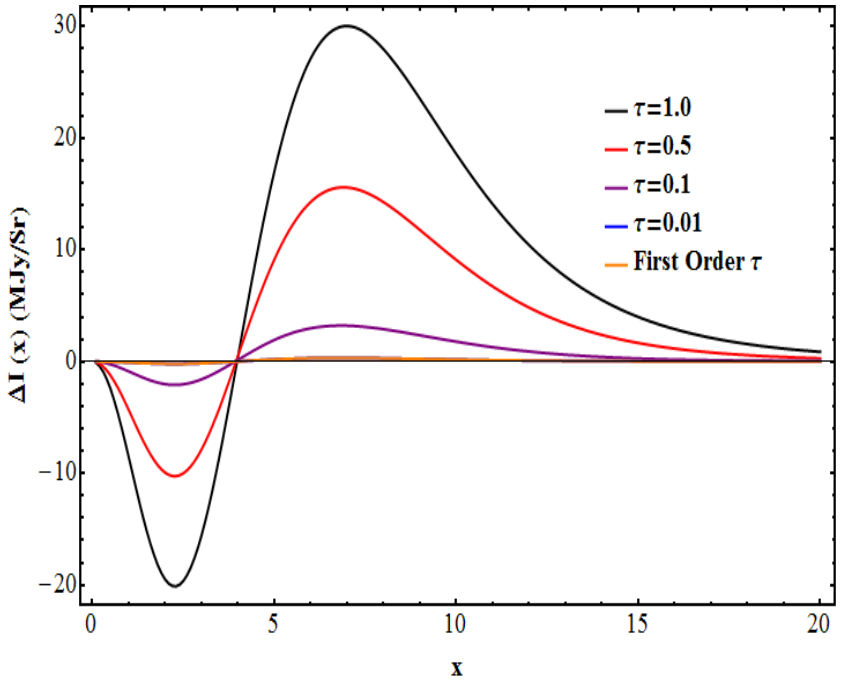

Figure 4.6: The change in intensity for an isotropic incident radiation using the exact redistribution kernel $P(s)$ computed for a thermal population of electrons for different optical depth. We used $\tau = 0.01$ for the first order approximation.

density of plasma in cosmic structures. Figure 4.6 and Figure 4.7 show the spectrum for a thermal and non-thermal population in the high optical depth regime.

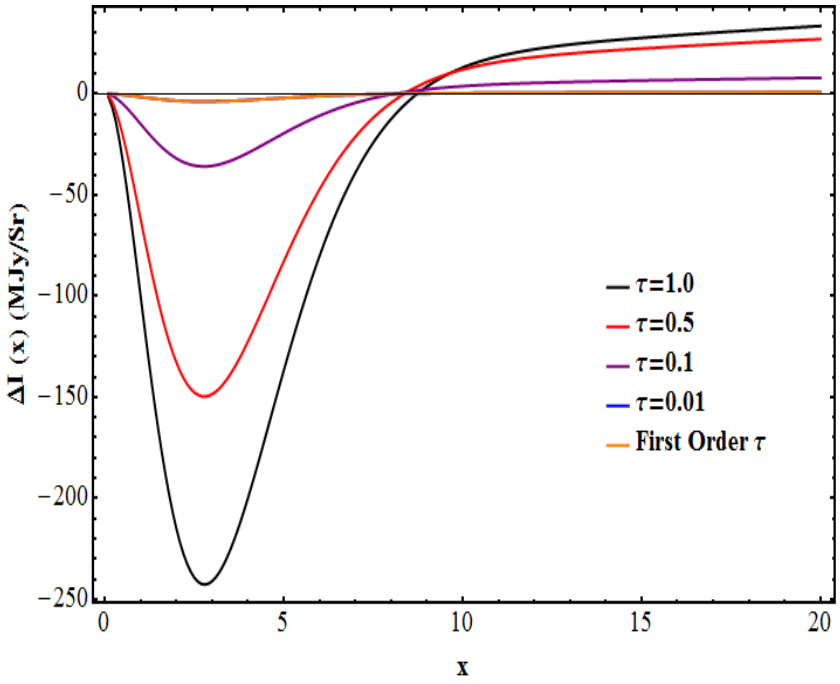

Figure 4.7: The change in intensity for an isotropic incident radiation using the exact redistribution kernel $P(s)$ computed for a non-thermal population of electrons for different optical depth. We use $\tau = 0.01$ for the first order approximation.

Chapter 5

Polarization of the Sunyaev Zeldovich effect

As mention earlier the CMB is anisotropic on the level of 10^{-5} and ,in the non-relativistic case, will produce a polarization proportional to the quadrupole moment of the incident radiation upon scattering with the electrons in galaxy clusters. Polarization in SZE arises mainly due to the thermal electrons scattering the low energy photons of the CMB radiation but in addition to that polarization also arise from the non thermal population of electrons present in radio halos as well as in radio-relics. The measured polarization is usually of the order of the optical depth τ_e in the case of single scattering. Sunyev and Zeldovich 1980b made reference to polarization in measuring cluster velocities and from this onwards many works have been done to compute polarization in SZE whether in relativistc or non-relativistic domain (Portsmouth & Bertschinger 2004b, Nagirner & Poutanen 1994 etc). We present here, following the approach of Portsmouth & Bertschinger 2004b, a general formalism to compute SZE in a completely relativistic manner. The method relies on the Covariant Formalism of the SZE (Nozawa & Kohyama 2009) where the Boltzmann collisional integral is solved but this time, polarization is taken into account.

5.1 Polarization due to the CMB quadrupole

Before computing SZE polarization in a full relativistic formalism, we derive here the generation of polarization in the non relativistic regime and then in the next section we describe the extension to relativistic domain.A first approach in the study of polarization in Sunyaev Zeldovich effect is based on the assumption that the speed of the electrons which diffuse the CMB is small $\beta_e << 1$ and also that the Thomson limit is valid that is $h\nu << m_e c^2$. Under the second assumption the process can be described using Thomson cross-section. Assuming that the incident radiation is not polarized but still anisotropic, the outgoing radiation will have the same degree of linear polarization proportional to the quadrupole moment in the angular distribution of the incident radiation. Chosing a frame of reference in such a way that the Z-axis coincides with the line of sight of the scattered radiation at first scattering, the Stokes parameters Q and U will be given by the following integral (Chandrasekhar 1960):

$$\frac{\partial Q}{\partial \tau}(x) = \frac{3}{16\pi}\int \sin^2(\theta)\cos(2\phi) I(\nu,\theta,\phi) d\Omega, \tag{5.1}$$

$$\frac{\partial U}{\partial \tau}(x) = \frac{3}{16\pi}\int \sin^2(\theta)\sin(2\phi) I(\nu,\theta,\phi) d\Omega, \tag{5.2}$$

where $x = h\nu/kT_0$. The integral is computed over all direction of the incident radiation.The intrinsic anisotropy of the incoming radiation in the case of the CMB is given by the primordial fluctuations of the temperature dependent unit vector $\hat{n}(\theta,\phi)$. Thus $I(\nu,\theta,\phi)$ is written as:

$$I(\nu,\theta,\phi) = \frac{2h}{c^2}\frac{\nu^3}{\exp\left[\frac{h\nu}{kT(\theta,\phi)}\right]-1}, \tag{5.3}$$

where in this case $T(\hat{n})$ is given by

$$T(\hat{n}) = T_0[1+\delta(\theta,\phi)], \tag{5.4}$$

and

$$\delta(\theta,\phi) = \sum_{l,m}^{\infty} a_{l,m} Y_{l,m}(\theta,\phi). \tag{5.5}$$

By putting eq 5.5 into eq 5.4 and then substitute into eq 5.3, we can write the intensity of the incident radiation as an expansion in terms of the spherical harmonics given that the variations in the temperature of the CMB are generally very small:

$$I(x,\theta,\phi) = \frac{2(kT_0)^3}{(hc)^2}\left[\frac{x^3}{e^x-1} + \frac{e^x x^4}{(e^x-1)^2}\sum_{l,m}^{\infty} a_{l,m}Y_{l,m}(\theta,\phi)\right] + O(\delta^2). \quad (5.6)$$

Now putting this into eq 5.1 and eq 5.2 and integrate over the solid angle leave us with only two terms $l = 2, m = \pm 2$. This answer can be written as

$$\frac{\partial Q}{\partial \tau}(x) = \sqrt{\frac{3}{10\pi}}\frac{I_{2,2} + I_{2,-2}}{4} = \frac{1}{2}\sqrt{\frac{3}{10\pi}}Re[I_{2,2}(x)], \quad (5.7)$$

and

$$\frac{\partial U}{\partial \tau}(x) = \sqrt{\frac{3}{10\pi}}\frac{I_{2,-2} + I_{2,-2}}{4i} = -\frac{1}{2}\sqrt{\frac{3}{10\pi}}Im[I_{2,2}(x)]. \quad (5.8)$$

We use the fact that $I^*_{l,m} = (-1)^m I_{l,-m}$. Then we obtain the Stokes parameter Q and U as follows:

$$\frac{\partial Q}{\partial \tau}(x) = \frac{1}{2}\sqrt{\frac{3}{10\pi}}\frac{(kT_0)^3}{(hc)^2}Re[a_{2,2}]F_1(x) = Re[a_{2,2}]F_1(x) \times 20.863\left(\frac{\text{MJy}}{\text{Sr}}\right). \quad (5.9)$$

and

$$\frac{\partial U}{\partial \tau}(x) = -\frac{1}{2}\sqrt{\frac{3}{10\pi}}\frac{(kT_0)^3}{(hc)^2}Im[a_{2,2}]F_1(x) = -Im(a_{2,2})F_1(x) \times 20.8633\left(\frac{\text{MJy}}{\text{Sr}}\right), \quad (5.10)$$

where $F_1(x) = \dfrac{x^4}{2\sinh^2(\frac{x}{2})}$. From this we can define the degree of polarization as follows

$$\Pi(x) = \frac{\tau}{I(x,T_0)}\sqrt{\left(\frac{\partial Q}{\partial \tau}\right)^2 + \left(\frac{\partial U}{\partial \tau}\right)^2} = \frac{\tau}{2}\sqrt{\frac{3}{10\pi}}|a_{2,2}|\frac{xe^x}{e^x-1}. \quad (5.11)$$

We computed the Stokes parameter Q and the degree of polarization which are shown in Figure 5.1 and Figure 5.2.

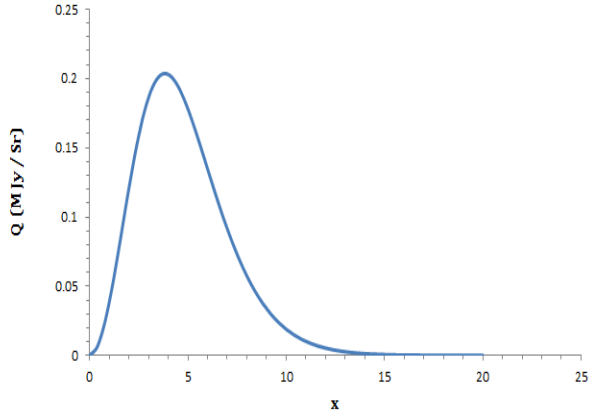

Figure 5.1: The Stokes parameter Q with $a_{2,2} = 10^{-4}$ and $\tau = 0.01$.

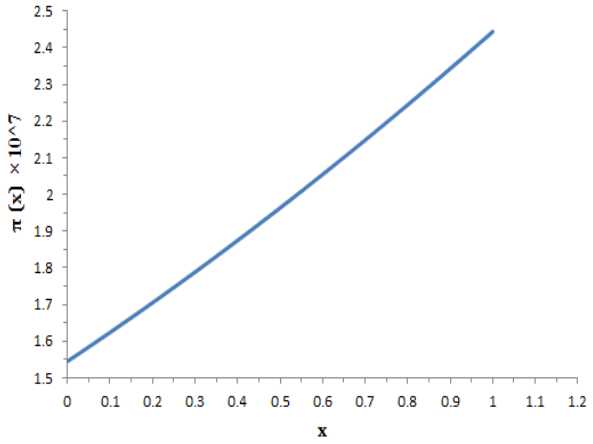

Figure 5.2: The degree of polarization in the case of $|a_{2,2}| = 0.0001$ and $\tau = 0.01$.

5.2 Polarization of the SZE in the relativistic formalism

In order to include polarization in Sunyaev Zeldovich , we follow the approach of Portsmouth and Bertshinger 2004b. From now onwards we are going to use $c = 1$ and $h = 1$ except where otherwise specifed. The Covariant Boltzmann equation for Compton scattering of photons due to electrons in a given rest-frame ($V_L^\mu = [1, 0, 0, 0]$) in the non-polarized case is written as (Itoh et al 1998):

$$\frac{df(\vec{p_1})}{dt} = 2\int d^3q_1 d^3q_2 d^3p_2 W\Big[f(\vec{p_2})g_e(\vec{q_2}) - f(\vec{p_1})g_e(\vec{q_1})\Big], \tag{5.12}$$

with W written as

$$W = \frac{3\sigma_T}{32\pi}m_e^2\frac{X}{E_1E_2p_1p_2}\delta^4\big(p_1^\mu + q_1^\mu - p_2^\mu - q_2^\mu\big), \tag{5.13}$$

$$X = m_e^2\left(\frac{1}{k_2} - \frac{1}{k_1}\right)^2 + 2m_e\left(\frac{1}{k_1} - \frac{1}{k_2}\right) + \frac{1}{2}\left(\frac{k_1}{k_2} + \frac{k_2}{k_1}\right), \tag{5.14}$$

and k_1 and k_2 are defined as follows:

$$k_1 = -p_1^\mu V_{2\mu} \tag{5.15}$$

$$k_2 = -p_2^\mu V_{2\mu}. \tag{5.16}$$

This equation describes the interaction $\gamma(\vec{p_1}) + e^-(\vec{q_1}) \longrightarrow \gamma(\vec{p_2}) + e^-(\vec{q_2})$. In the rest-frame V_L, $\vec{p_1}$ and $\vec{p_2}$ represent the momentum of the photon before and after collision and $\vec{q_1}$ and $\vec{q_2}$ represent the momentum of the electron before and after collision. The 4-vectors in the delta function are represented as $p_1^\mu = \big(p_1, \vec{p_1}\big)$, $q_1^\mu = \big(E_1, \vec{q_1}\big)$ and $p_2^\mu = \big(p_2, \vec{p_2}\big)$ and $q_2^\mu = \big(E_2, \vec{q_2}\big)$. k_i represents the magnitude of the photon with 4-momentum p_i^μ in the rest frame of V_2 where $i = 1, 2$. The time derivative $\frac{d}{dt}$ should be interpreted as

$$\frac{d}{dt} = \frac{1}{p_1}p_1^\alpha\partial_\alpha. \tag{5.17}$$

Usually it is very convenient to intepret the Boltzmann equation as consisting of two terms, "scattering in" and "scattering out" of the momentum element

d^3p_1 which can be written as follows:

$$\frac{df}{dt} = \frac{df}{dt}_{in} - \frac{df}{dt}_{out}. \tag{5.18}$$

The first term is the rate of scattering of photons with momentum $\vec{p_2}$ from electrons with momentum $\vec{q_2}$ into d^3p_1 around $\vec{p_1}$ while the second term represents the rate of scattering of photons with momentum $\vec{p_1}$ from electrons $\vec{q_1}$ into d^3p_2 around $\vec{p_2}$. We should also point out that this equation neglects stimulated emission as well as Pauli blocking but is still valid outside Thomson's regime where quantum effects are not negligible. The covariant Boltzmann equation for polarization is very similar to the non-polarized one except that the cross-section and the distribution functions becomes tensor quantities which in turn requires the use of projection tensors (see Portsmouth & Bertschinger 2004b). The equation writes as follows:

$$\begin{aligned} p_1 \frac{df}{dt}^{\mu\nu}(p_1^m, V_L^m) &= m_e^2 \sigma_T \int \frac{d^3q_1}{E_1}\frac{d^3q_2}{E_2}\frac{d^3p_2}{p_2}\delta^4\left(p_1^\mu + q_1^\mu - p_2^\mu - q_2^\mu\right) \times \\ &\quad \times P^{\mu\nu}_{\alpha\beta}(p_1^m, V_L^m)\Big[\Phi^{\alpha\beta}_{\rho\sigma}(p_1^m, p_2^m, V_2^m) f^{\rho\sigma}(p_2^m, V_L^m) g_e(\vec{q_2}) + \\ &\quad - \phi^{\alpha,\beta}(p_1^m, V_L^m) g_{\gamma\delta} \Phi^{\gamma\delta}_{\rho,\sigma}(p_2^m, p_1^m, V_1^m) f^{\rho\sigma}(p_1^m, V_L^m) g_e(\vec{q_1})\Big]. \end{aligned} \tag{5.19}$$

We again here specify that $V_L^\mu = [1, 0, 0, 0]$. We usually call it the lab frame and it is the frame in which it is seeing the velocity of the electrons to be V_1^m/V_2^m and its polarization tensor for photons with momentum p_1^μ is denoted by $f^{\mu\nu}(p_1^m, V_L^m)$. V_1^m and V_2^m denotes the 4-velocity of the electron before and after collision whose momentum is q_1^m and q_2^m respectively whereas p_1^m and p_2^m represent that of the photon before and after the interaction.

Note: There is something that we need to be clear about the notation used for the distribution function which is that $f^{\mu\nu}(p^m, V^m)$ does not mean that f is a function of V^m in the usual sense of function variables but it says that f is the distribution function of the observer going with velocity V and it also

does not mean that we are evaluating $f^{\mu\nu}$ in its rest-frame. If one wants to get the distribution function in the rest-frame one has to Lorentz-transform to the V frame in order to do so. So the function $f^{\mu\nu}(p^m, V^m) \longrightarrow f^{\mu\nu}(p^0, \vec{p}, V^m)$ $\longrightarrow f^{\mu\nu}(\vec{p}, V^m)$ can also be written as $f^{\mu\nu}(\vec{p}, V^m)$. Also for the scalar function $f(p^\mu) \longrightarrow f(p^0, \vec{p}) \longrightarrow f(\vec{p})$. The reason why we can write it in terms of only 3-vectors is because $p^0 = |p|$ for the photon but it is also true for massive particles because $p^0 = \sqrt{p^2 + m^2}$. The cross-section here becomes a tensor as we have mentioned before and is written as follows:

$$\begin{aligned} \Phi^{\mu\nu}_{mn}\big[p^m_1, p^m_2, V^m_2\big] &\longrightarrow \text{ is the scattering cross-section for } (p^m_2, V^m_2) \rightarrow p^m_1 \ , \\ \Phi^{\mu\nu}_{mn}\big[p^m_2, p^m_1, V^m_1\big] &\longrightarrow \text{ is the scattering cross-section for } (p^m_1, V^m_1) \rightarrow p^m_2 \ . \end{aligned} \tag{5.20}$$

This $\Phi^{\mu\nu}_{mn}$ is an analogue of X for the polarized case and is constructed out of projection tensors (see Portsmouth & Bertschinger 2004b). The tensor $\phi^{\mu\nu}$ represents the normalized polarization tensor written as $f^{\mu\nu}/f$. Then finally we have $P^{\mu\nu}_{\alpha\beta}$ which is constructed out of the projection tensors as follows:

$$P^{\mu\nu}_{\alpha\beta}(p^m, v^m) = P^\mu_\alpha(p^m, V^m) P^\nu_\beta(p^m, V^m). \tag{5.21}$$

This projection actually projects the terms in the right hand side of the Boltzmann polarized equation into the plane perpendicular to the photon with momentum p^m_1 and 4-velocity of the observer V^m_L. In the rest frame of the observer V^m_L the projection tensor has only spatial components (see Portsmouth & Bertschinger 2004a). The cross-section term is written in terms of the projection tensors in Thomson approximation as

$$\Phi^{\mu\nu}_{\gamma\delta}(p^m_2, p^m_1, V^m_1) = \frac{3}{8\pi} P^{\mu\nu}_{\alpha\beta}(p^m_2, V^m_1) P^{\alpha\beta}_{\gamma\delta}(p^m_1, V^m_1). \tag{5.22}$$

The $\delta^4(p^\mu_1 + q^\mu_1 - p^\mu_2 - q^\mu_2)$ can be integrated out by using the following relation:

$$\frac{d^3 q_1}{E_1} = d^4 q^\mu_1 \delta\big[\frac{1}{2}(q^\mu_1 q_{1\mu} + m^2_e)\big]. \tag{5.23}$$

We also write the electron distribution function as $g_e(\vec{q}) = n_e f_e(\vec{q})$ where n_e is the electron number density. We can also use the definition of optical depth,

$d\tau_e = n_e \sigma_T dt$, to get rid of the Thomson total cross-section. The collision equation is written as

$$q_1^m = q_2^m + p_2^m - p_1^m. \tag{5.24}$$

This acts as a constraint on q_1^m and using this the delta function in eq 5.19 can be simplified to

$$\delta\big[\frac{1}{2}(q_1^m q_{1m} + m_e^2)\big] = \delta\big[m_e\big(k_1 - (k_2 + R_{12})\big)\big]. \tag{5.25}$$

We have also introduced a new variable, $R_{12} = p_1^\mu p_{2\mu}/m_e$, which is going to be very useful for later calculations. Using all these simplifications we can now cast the Boltzmann polarized equation as follows

$$\begin{aligned} p_1 \frac{\partial}{\partial \tau} f^{\mu\nu}(p_1^m, V_L^m) \quad &= \quad m_e^2 \int \frac{d^3q_2}{E_2}\frac{d^3p_2}{p_2}\delta\big[m_e\big(k_1 - (k_2 + R_{12})\big)\big] \times \\ &\times P^{\mu\nu}_{\alpha\beta}(p_1^m, V_L^m)\Big[\Phi^{\alpha\beta}_{\rho\sigma}(p_1^m, p_2^m, V_2^m) f^{\rho\sigma}(p_2^m, V_L^m) f_e(\vec{q_2}) + \\ &- \phi^{\alpha\beta}(p_1^m, V_L^m) g_{\gamma\delta} \Phi^{\gamma\delta}_{\rho\sigma}(p_2^m, p_1^m, V_1^m) f^{\rho\sigma}(p_1^m, V_L^m) f_e(\vec{q_1})\Big]. \end{aligned} \tag{5.26}$$

We stress here that $\vec{q_1}$ is not a free variable and it is constrained by the collision kinematics given by $\vec{q_1} = \vec{q_2} + \vec{p_2} - \vec{p_1}$.

5.2.1 The distribution function in the Thomson approximation

Now we will show how we can use this formalism to derive the Stokes parameters of the scattered radiation by an electron gas. To do this we will make three important assumptions which actually not only simplify the calculation but also allows the results to be check with previous work. The three assumptions are

1. Single Scattering approximation

This means that we assume that the each photon is scattered once by the electrons. This is valid in mild optical depth regime making it quite valid for the study of galaxy clusters.

2. Thomson's cross-section

This means that we are neglecting quantum effects and in this way the scattering in the electron rest-frame can easily be described by Thomson's scattering which in turn simplifies the cross-section term.

3. Unpolarized CMB

What we mean by this assumption is that before scattering the CMB is completely unpolarized which is not completely true but for most calculations it is quite a reasonable simplification because the degree of polarization of CMB before collision is very small (Dunkley et al. 2009).

With these assumptions in hand the Boltzmann polarized equation can be simplified extensively. In addition to these assumptions we also make a small change in our notation mainly $q_2 \longrightarrow q_e$ and also $V_2 \longrightarrow V_e$. For single scattering the equation writes as

$$\begin{aligned} p_1 \frac{\partial}{\partial \tau} f^{\mu\nu}(p_1^m, V_L^m) &= m_e \int \frac{d^3 q_e}{\gamma_e} \frac{d^3 p_2}{p_2} \delta\big[m_e\big(k_1 - (k_2 + R_{12})\big)\big] \times \\ &\times P^{\mu\nu}_{\alpha\beta}(p_1^m, V_L^m) \Big[\Phi^{\alpha\beta}_{\rho\sigma}(p_1^m, p_2^m, V_e^m) f^{\rho\sigma}(p_2^m, V_L^m) f_e(\vec{q_e}) + \\ &- \phi^{\alpha\beta}(p_1^m, V_L^m) g_{\gamma\delta} \Phi^{\gamma\delta}_{\rho\sigma}(p_2^m, p_1^m, V_1^m) f^{\rho\sigma}(p_1^m, V_L^m) f_e(\vec{q_1}) \Big]. \end{aligned} \tag{5.27}$$

Now we make use of our second assumption which is the Thomson limit which writes as

$$\begin{aligned} \gamma_e \alpha_2 &<< 1, \\ \alpha_2 &= \frac{p_2}{m_e}. \end{aligned} \tag{5.28}$$

We also use the cross-section that we introduced in the previous section written as

$$\Phi^{\mu\nu}_{\gamma\delta}(p_k^m, p_i^m, V_i^m) = \frac{3}{8\pi} P^{\mu\nu}_{\alpha\beta}(p_k^m, V_i^m) P^{\alpha\beta}_{\gamma\delta}(p_i^m, V_i^m). \tag{5.29}$$

One point to be noted with this cross-section term is that the projection tensors which project the distribution function perpendicular to V_i^m and p_i^m is included

in it where $k, i = 1, 2$. Then we define the following very useful variables

$$\begin{aligned} n_{12} &= \frac{k_1}{p_1} = \gamma_e\big(1 - \vec{\beta}_e.\hat{n_1}\big), \\ n_{22} &= \frac{k_2}{p_2} = \gamma_e\big(1 - \vec{\beta}_e.\hat{n_2}\big), \\ r_{12} &= \frac{p_1^\mu p_{1\mu}}{p_1 p_2} = m_e R_{12} = \hat{n_1}.\hat{n_2} - 1. \\ \alpha_j &= \frac{p_j}{m_e}. \end{aligned} \tag{5.30}$$

where $\hat{n_1}$ and $\hat{n_2}$ are unit vectors in direction of $\vec{p_1}$ and $\vec{p_2}$ and $\vec{\beta}_e$ is the electron velocity. The delta function $\delta\big[m_e\big(k_1 - (k_2 + R_{12})\big)\big]$ can be further simplified by using the Thomson limit as follows:

$$\begin{aligned} m_e\big[k_1 - (k_2 + R_{12})\big] &= -m_e^2 n_{22}\big[\alpha_2 - \alpha_1\frac{n_{12}}{n_{22}}(1 - \alpha_2\frac{r_{12}}{n_{12}})\big] \\ &= -m_e^2 n_{22}\big[\alpha_2 - \alpha_1\frac{n_{12}}{n_{22}}(1 - O(\alpha_2\gamma_e)) \\ &= -m_e^2 n_{22}\big[\alpha_2 - \alpha_1\frac{n_{12}}{n_{22}}\big]. \end{aligned} \tag{5.31}$$

In order to arrive at the previous approximation we made use of the following inequality:

$$\alpha_2|\frac{r_{12}}{n_{12}}| \leq \frac{2\alpha_2}{\gamma_e(1 - \beta_e)} = 2\alpha_2(1 + \beta_e)\gamma_e \leq 4\gamma_e\alpha_2 = O(\gamma_e\alpha_2). \tag{5.32}$$

We should also bear in mind that the variable p_2 is not free but is constraint by the following:

$$p_2 = \frac{n_{12}}{n_{22}}p_1. \tag{5.33}$$

Another simplification can be made by noticing that

$$\gamma_1 = \gamma_e\big[1 + O(\alpha_2\gamma_e)\big]. \tag{5.34}$$

This can be achieved by putting $m = 0$ in the equation $q_1^m = q_2^m + p_2^m - p_1^m$. Using $\alpha_1 = \big(n_{22}/n_{12}\big)\ \alpha_2$ we get

$$\gamma_1 = \gamma_e + \alpha_2\left[1 - \frac{n_{22}}{n_{12}}\right]. \tag{5.35}$$

Then one can show that:

$$\begin{aligned}\gamma_1 &= \gamma_e\Big(1+\frac{\alpha_2}{\gamma_e}\ (1-\frac{n_{22}}{n_{12}})\Big) \leq \\ &\leq \gamma_e\Big(1+\frac{\alpha_2}{\gamma_e}\ \Big|1-\frac{n_{22}}{n_{12}}\Big|\Big) = \\ &= \gamma_e\Big[1+2\beta_e\alpha_2\big(1+\beta_e\big)\gamma_e\Big] \leq \\ &\leq \gamma_e\Big[1+4\alpha_2\gamma_e\Big] = \\ &= \gamma_e\Big[1+O(\alpha_2\gamma_e)\Big]. \end{aligned} \tag{5.36}$$

To arrive at the result we use the following inequalities:

$$\begin{aligned}\Big|\alpha_2\big(1-\frac{n_{22}}{n_{12}}\big)\Big| &\leq \Big|\alpha_2\Big[1-\frac{1+\beta_e}{1-\beta_e}\Big]\Big| = \\ &= \alpha_2\Big|\frac{-2\beta_e}{1-\beta_e}\Big| = \\ &= 2\beta_e\alpha_2\big(1+\beta_e\big)\gamma_e^2 \leq \\ &\leq 4\alpha_2\gamma_e^2. \end{aligned} \tag{5.37}$$

To calculate the integrals inside the Boltzmann equation we can always choose a frame of reference in which the electron gas is isotropic and therefore we can do this last simplification:

$$f_e(\vec{q_1}) \approx f_e(\vec{q_e}). \tag{5.38}$$

With all these simplifications we arrive at this:

$$\begin{aligned}\frac{\partial}{\partial\tau}f^{\mu\nu}(p_1^m, V_L^m) &= \frac{3}{8\pi}\int\frac{d^3q_e}{\gamma_e}\int d\Omega_2\frac{n_{12}}{n_{22}^2}f_e(\vec{q_e})\times \\ &\times\Big[J_\alpha^\mu(p_1^m, V_e^m, V_L^m)J_\beta^\nu(p_1^m, V_e^m, V_L^m)f^{\alpha\beta}(p_2^m, V_e^m) + \\ &-\phi^{\mu\nu}(p_1^m, V_L^m)P_{\alpha\beta}(p_2^m, V_1^m)f^{\alpha\beta}(p_1^m, V_1^m)\Big], \end{aligned} \tag{5.39}$$

with

$$J^{\mu}_{\alpha}(p^m_1, V^m_e, V^m_L) = P^{\mu}_{\beta}(p^m_1, V^m_L) P^{\beta}_{\alpha}(p^m_1, V^m_e). \tag{5.40}$$

Now we make use of the third assumption which is that the CMB is unpolarized prior to scattering by the electrons. With this assumption one can replace:

$$f^{\mu\nu}(p^m, V^m) = \frac{1}{2} f(p^m) P^{\mu\nu}(p^m, V^m), \tag{5.41}$$

$$\phi^{\mu\nu}(p^m, V^m) = \frac{1}{2} P^{\mu\nu}(p^m, V^m). \tag{5.42}$$

Then at last the equation is written as follows:

$$\begin{aligned} \frac{\partial}{\partial \tau} f^{\mu\nu}(p^m_1, V^m_L) = & \frac{3}{16\pi} \int \frac{d^3 q_e}{\gamma_e} \int \Omega_2 \frac{n_{12}}{n^2_{22}} f_e(\vec{q_e}) \times \\ & \times \Bigg[\Big[P^{\mu\nu}(p^m_1, V^m_L) - L^{\mu} L^{\nu}(p^m_1, p^m_2, V^m_e) \Big] f(p^m_2) + \\ & - P^{\mu\nu}(p^m_1, V^m_L) \Big[1 + \eta_{12} \big(1 + \frac{1}{2} \eta_{12} \big) \Big] f(p^m_1) \Bigg], \end{aligned} \tag{5.43}$$

where we have defined these variables:

$$\begin{aligned} L^{\mu}(p^m_1, p^m_2, V^m_e) &= \frac{1}{n_{22}} \left[\frac{p^{\mu}_2}{p_2} - \left(1 + \gamma_e \frac{r_{12}}{n_{12}} \right) \frac{p^{\mu}_1}{p_1} + \frac{r_{12}}{n_{12}} V^{\mu}_e \right], \\ \eta_{12} &= \frac{r_{12}}{n_{12} n_{22}}, \\ L^{\mu} L_{\mu} &= -2\eta_{12} \left(1 + \frac{1}{2} \eta_{12} \right). \end{aligned} \tag{5.44}$$

In these last equations we re-call that p^{μ}_1 or p^{μ}_2 is the momentum in the frame $V^{\mu}_L = \big[1, 0, 0, 0\big]$ and from this we can say that $p_k = -p^{\mu}_k V_{L\mu}$. Since we are using $c = 1$ and $h = 1$, then p_1 and ν_1 can be interchange at will.

5.2.2 Stokes parameters

We show here how the Stokes parameters are derived from this formalism using the same techniques of Porthsmouth and Betsrchinger (2004a). We first derive

the first Stokes parameter I which is straight forward

$$\frac{\partial}{\partial\tau}I(\vec{p_1}) = p_1^3\frac{d}{d\tau}f_\mu^\mu(\vec{p_1}) = \frac{3p_1^3}{8\pi}\int\frac{d^3q_e}{\gamma_e}\int d\Omega_2\frac{n_{12}}{n_{22}^2}f_e(\vec{q_e})\times \times\left[1+\eta_{12}\left(1+\frac{\eta_{12}}{2}\right)\right]\left[f(\vec{p_2})-f(\vec{p_1})\right]. \tag{5.45}$$

where here we have used the notation $f(p^\mu) = f(\vec{p})$ which we already discussed before and the fact that $I = p^3 f$ which is the relation between the distribution function of photons to the intensity. Now to determine the other Stokes parameters namely Q and U the choice of basis matters here and depending on how the basis are chosen will determine the simplicity of the calculation (see Portsmouth and Bertschinger 2004b). In our case we choose a system of basis perpendicular to the observed radiation, that is in usual term we choose our z-axis to be along the direction of the observed radiation. In this way the tensor $f^{\mu\nu}(\vec{p_1})$ can be written as follows:

$$f^{\mu\nu}(\vec{p_1}) = \frac{1}{2p_1^3}\begin{bmatrix} 0 & 0 & 0 & 0 \\ 0 & I(\vec{p_1})+Q(\vec{p_1}) & U(\vec{p_1})+iV(\vec{p_1}) & 0 \\ 0 & U(\vec{p_1})-iV(\vec{p_1}) & I(\vec{p_1})-Q(\vec{p_1}) & 0 \\ 0 & 0 & 0 & 0 \end{bmatrix}. \tag{5.46}$$

We then extract the Stokes parameters from this matrix as follows

$$\frac{d}{d\tau}Q(\nu_1) = \nu_1^3\frac{d}{d\tau}\left[f^{11}(\nu_1)-f^{22}(\nu_1)\right], \tag{5.47}$$

$$\frac{d}{d\tau}U(\nu_1) = \nu_1^3\frac{d}{d\tau}\left[f^{12}(\nu_1)+f^{21}(\nu_1)\right]. \tag{5.48}$$

In this coordinate system the following parameters take the form:

$$p_1^\mu = p_1\big(1,0,0,1\big), \tag{5.49}$$

$$r_{12} = \cos\theta_2 - 1, \tag{5.50}$$

$$n_{12} = \gamma_e\big[1-\beta_e\cos\theta_e\big], \tag{5.51}$$

$$n_{22} = \gamma_e\Big[1-\beta_e\big[\cos\theta_2\cos\theta_e+\sin\theta_2\sin\theta_e\cos(\phi_2-\phi_e)\big]\Big]. \tag{5.52}$$

Here θ_e and θ_2 represent the polar angles for the vector $\vec{\beta_e}$ and $\vec{p_2}$ while ϕ_e and ϕ_2 are the azimuthal angles for the same two vectors. Then the four-vectors V_e^μ and p_2^μ can be written in component forms

$$V_e^\mu = \gamma_e \Big[1, \beta_e \cos\phi_e \sin\theta_e, \beta_e \sin\phi_e \sin\theta_e, \beta_e \cos\theta_e\Big], \tag{5.53}$$

$$p_2^\mu = p_2 \Big[1, \cos\phi_2 \sin\theta_2, \sin\phi_2 \sin\theta_2, \cos\theta_2\Big]. \tag{5.54}$$

The Stokes parameters Q and U are then written as follows:

$$\begin{aligned}
\frac{\partial Q}{\partial \tau} &= -\frac{3}{16\pi} \int \frac{d^3 q_e}{\gamma_e} \int d\Omega_2 \frac{I(\nu_2, \hat{n}_2)}{n_{12}^4 n_{22}} f_e(\vec{q_e}) \times \\
&\quad \times \big[\cos 2\phi_2 \sin^2\theta_2 n_{12}^2 + 2\cos(\phi_2 + \phi_e) \sin\theta_2 \sin\theta_e n_{12} r_{12} \gamma_e \beta_e + \\
&\quad + \cos 2\phi_e \sin^2\theta_e r_{12}^2 \beta_e^2 \gamma_e^2 \big], \qquad (5.55) \\
\frac{\partial U}{\partial \tau} &= -\frac{3}{16\pi} \int \frac{d^3 q_e}{\gamma_e} \int d\Omega_2 \frac{I(\nu_2, \hat{n}_2)}{n_{12}^4 n_{22}} f_e(\vec{q_e}) \times \\
&\quad \times \big[\sin 2\phi_2 \sin^2\theta_2 n_{12}^2 + 2\sin(\phi_2 + \phi_e) \sin\theta_2 \sin\theta_e n_{12} r_{12} \gamma_e \beta_e + \\
&\quad + \sin 2\phi_e \sin^2\theta_e r_{12}^2 \beta_e^2 \gamma_e^2 \big]. \qquad (5.56)
\end{aligned}$$

These 5-dimensional integrals can be evaluated by breaking them into 5 one-dimensional integrals. By doing this on the first Stokes parameter I one can show that the formalisms discussed at the start of the previous chapter are consistent with each other in the Thomson limit.

5.2.3 The Stokes parameter I

We compute here the integrals for the Stokes parameter I for an isotropic incident radiation first and later we will introduce an anisotropy via a series expansion. We start by defining $\mu_e = \cos\theta_e$, $\mu_2 = \cos\theta_2$ and $\phi_0 = \phi_2 - \phi_e$. With these new variables equation takes the form as follows:

$$\begin{aligned}
\frac{\partial f}{\partial \tau}(\nu_1) &= \frac{3}{32\pi^2} \int_0^1 d\beta_e \int_{-1}^1 d\mu_e \int_0^{2\pi} d\phi_e \int_{-1}^1 d\mu_2 \int_0^{2\pi} d\phi_0 \frac{n_{12}\ f_e(\beta_e)}{\gamma_e n_{22}^2} \times \\
&\quad \times \Big[1 + \eta_{12}\Big(1 + \frac{\eta_{12}}{2}\Big)\Big] \Big[f(\nu_2) - f(\nu_1)\Big], \qquad (5.57)
\end{aligned}$$

where we have used also

$$\frac{1}{4\pi} f_e(\beta_e) d\beta_e = f_e(q_e) q_e^2 dq_e, \tag{5.58}$$

and the fact that

$$\int_0^{2\pi} \int_0^{2\pi} \Psi(\phi_e, \phi_2 - \phi_e)\ d\phi_2\ d\phi_e = \int_0^{2\pi} \int_0^{2\pi} \Psi(\phi_e, \phi_0)\ d\phi_0\ d\phi_e. \tag{5.59}$$

In order to further simplify the equation we introduce another variable:

$$\chi_0 = \cos\phi_0, \tag{5.60}$$

and if we consider a function which has trigonometric functions as its argument, then we can write

$$\begin{aligned} \int_0^{2\pi} F(\cos\phi_0, \sin\phi_0) d\phi_0 &= \int_{-1}^{1} \Big[F(\cos\phi_0 \to \chi_0, \sin\phi_0 \to \sqrt{1-\chi_0^2}) + \\ &\quad + F(\cos\phi_0 \to \chi_0, \sin\phi_0 \to -\sqrt{1-\chi_0^2}) \Big] \frac{d\chi_0}{\sqrt{1-\chi_0^2}}. \end{aligned} \tag{5.61}$$

Then we arrive at the following equation by integrating over ϕ_e:

$$\begin{aligned} \frac{\partial f}{\partial \tau}(\nu_1) &= \frac{3}{16\pi} \int_0^1 d\beta_e \int_{-1}^1 d\mu_e \int_{-1}^1 d\mu_2 \int_{-1}^1 d\chi_0\ f_e(\beta_e) \times \\ &\quad \times \frac{2n_{12}^2 n_{22}^2 + 2n_{12} n_{22}(\mu_2 - 1) + (\mu_2 - 1)^2}{n_{12} n_{22}^4 \gamma_e \sqrt{1-\chi_0^2}} \big[f(\nu_2) - f(\nu_1) \big]. \end{aligned} \tag{5.62}$$

Now at this stage we can do a check that the Covariant Boltzmann equation gives the same result as the Wright's method by making a transformation into the electron frame using the following variables:

$$\begin{aligned} \mu_0 &= \frac{\mu_2 - 1}{n_{12} n_{22}} + 1, \\ \mu &= \frac{\gamma_e n_{12} - 1}{n_{12} \gamma_e \beta_e}, \\ \mu' &= \frac{\gamma_e n_{22} - 1}{n_{22} \gamma_e \beta_e}. \end{aligned} \tag{5.63}$$

We then obtain at the end an equation in terms of the new variables in this form:

$$\begin{aligned}\frac{\partial f}{\partial \tau}(\nu_1) &= \frac{3}{16\pi}\int d\beta_e \int d\mu \int d\mu' \int d\mu_0 \big[f\big(\nu_2\big) - f\big(\nu_1\big)\big] f(\beta_e) \times \\ &\times \frac{1+\mu_0^2}{\gamma_e^4(1-\beta_e\mu)^3\sqrt{1-\mu_0^2-\mu^2-\mu'^{\,2}+2\mu_0\mu\mu'}},\end{aligned} \tag{5.64}$$

with

$$\begin{aligned}\mu_{0,min} &= \mu\mu' - \sqrt{(1-\mu^2)(1-\mu'^{\,2})}, \\ \mu_{0,max} &= \mu\mu' + \sqrt{(1-\mu^2)(1-\mu'^{\,2})}..\end{aligned} \tag{5.65}$$

The integration on μ_0 can be done easily and then introducing a last variable, which is related to the frequency shift which has been used by many authors (Colafrancesco 2003, Ensslin and Kaiser 2000), the equation can be written similar to the way of computing the intensity in SZE using the Wright's method (see Colafrancesco 2003, Ensslin and Kaiser 2000). This shows that in the Thomson limit the Covariant formalism to Sunyaev Zeldovich is equivalent to the Wright's method. This was done by Nozawa and Kohyama (2009):

$$\begin{aligned}\frac{\partial f}{\partial \tau}(\nu_1) &= \int_{-\infty}^{\infty} P(s)\ \big[f(e^s\nu_1) - f(\nu_1)\big]\ ds, \\ P(s) &= \int_{\sinh\frac{|s|}{2}}^{1} f(p_e)\ P(s,p_e)\ dp_e, \\ P(s,\beta_e) &= \frac{3\ e^s}{32}\int_{\mu_{min}}^{\mu_{max}} \frac{(3-\mu^2)\beta_e^2 - (1-3\mu^2)\big[1-e^s(1-\mu\beta_e)\big]}{\beta_e^3\gamma_e^4(1-\beta_e\mu)^2}\ d\mu.\end{aligned} \tag{5.66}$$

The function $P(s,p_e)$ is just the function $P(s,\beta_e)$ with the β_e substituted in terms of p_e as well as γ_e. This is given by

$$\begin{aligned}\gamma_e &= \sqrt{1+p_e^2}, \\ \beta_e &= \frac{p_e}{\sqrt{1+p_e^2}}.\end{aligned} \tag{5.67}$$

This shows that the formalism is consistent and now we are in a position to include the anisotropy. The rate of change of the distribution function can be

broken down into two terms

$$\frac{\partial f}{\partial \tau}(\nu_1, \hat{z}) = \left.\frac{\partial f}{\partial \tau}\right|_{in}(\nu_1, \hat{z}) - \left.\frac{\partial f}{\partial \tau}\right|_{out}(\nu_1, \hat{z}). \tag{5.68}$$

The rate of scattering out can easily be integrated and we just write down the result:

$$\left.\frac{\partial f}{\partial \tau}\right|_{out}(\nu_1, \hat{z}) = f(\nu_1, \hat{z}). \tag{5.69}$$

To determine the scattering in we expand the distribution function in a spherical harmonic series as follows:

$$f(\nu_1, \hat{n}) = \sum_{l=0}^{l=\infty} \sum_{m=-l}^{m=l} f_{l,m}(\nu) Y_{l,m}(\cos\theta, \phi) \tag{5.70}$$

$$Y_{l,m}(\cos\theta, \phi) = \sqrt{\frac{2l+1}{4\pi}\frac{(l-1)!}{(l+m)!}} P_l^m(\cos\theta) e^{im\phi}. \tag{5.71}$$

Inserting the expanded distribution function into equation 5.62 and for the "scattering in term" we obtain:

$$\begin{aligned}
\left.\frac{\partial f}{\partial \tau}(\nu_1, \hat{z})\right|_{in} &= \frac{3}{32\pi^2} \sum_{l=0}^{\infty} \sum_{m=-l}^{l} \int d\beta_e d\mu_e d\phi_e \int d\mu_2 d\phi_0 \frac{n_{12} f_e(\beta_e)}{n_{22}^2 \gamma_e} \times \\
&\quad \times \left[1 + \eta_{12}\left(1 + \frac{\eta_{12}}{2}\right)\right] f_{l,m}(\nu_2) \sqrt{\frac{2l+1}{4\pi}} \times \\
&\quad \times \frac{(l-m)!}{(l+m)!} P_l^m(\mu_2) e^{im(\phi_0+\phi_e)} = \\
&= \frac{3}{16\pi} \sum_{l=0}^{\infty} \sqrt{\frac{2l+1}{4\pi}} \int d\beta_e d\mu_e \int d\mu_2 d\chi_0 f_e(\beta_e) \times \\
&\quad \times \frac{2n_{12}^2 n_{22}^2 + 2n_{12} n_{22}(\mu_2 + 1) + (\mu_2 + 1)^2}{n_{12} n_{22}^4 \gamma_e \sqrt{1 - \chi_0^2}} f_{l,0}(\nu_2) P_l^0(\mu_2).
\end{aligned} \tag{5.72}$$

The integration over ϕ_e eliminates all the terms in $m \neq 0$. One can adopt a similar approach as previously by using the variables introduce in eq 5.64 but

we will use another set of variables introduce as follows:

$$s = \ln\left(\frac{n_{12}}{n_{22}}\right),$$
$$t = \ln\left(n_{12}n_{22}\right), \tag{5.73}$$
$$\mu_0 = \frac{\mu_2 - 1}{n_{12}n_{22}} + 1. \tag{5.74}$$

Substituting these variables into equation 5.72 and subtracting the scattering out term, 5.69, we obtain a set of equations similar to 5.71:

$$\begin{aligned}
\frac{\partial f}{\partial \tau}(\nu_1, \hat{z}) &= \sum_{l=0}^{l=\infty} \int_{-\infty}^{\infty} P_{l,0}(s) f_{l,0}(e^s \nu_1)\ ds - f(\nu_1, \hat{z}), \\
P_{l,0}(s) &= \int_{\sinh\frac{|s|}{2}}^{1} f_e(p_e)\ P_{l,0}(s, p_e)\ dp_e, \qquad (5.75) \\
P_{l,0}(s, \beta_e) &= -\frac{3}{64\pi}\sqrt{\frac{2l+1}{\pi}}\frac{e^{\frac{3s}{2}}}{\gamma_e^3 \beta_e^2}\int_{-t_0}^{t_0} e^{\frac{t}{2}} dt \int_{A-B}^{A+B} \frac{1+\mu_0^2}{\sqrt{B^2 - \left(A-\mu_0\right)^2}} \times \\
&\quad \times P_l^0\left(e^t(\mu_0 - 1) + 1\right)\ d\mu_0.
\end{aligned}$$

where

$$\begin{aligned}
t_0 &= |s| - \ln\left(\frac{1+\beta_e}{1-\beta_e}\right), \\
A &= \frac{e^{-t}}{\gamma_e^2 \beta_e^2}\left[1 + \gamma_e^2 e^t - 2\gamma_e e^{\frac{t}{2}} \cosh\frac{s}{2}\right], \qquad (5.76) \\
B &= 2\frac{e^{\frac{t}{2}}}{\gamma_e^2 \beta_e^2}\sqrt{\left[\cosh\left(\frac{s-t}{2}\right) - \gamma_e\right]\left[\cosh\left(\frac{s+t}{2}\right) - \gamma_e\right]}.
\end{aligned}$$

The function $P_{l,0}(s, p_e)$ is just the function $P_{l,0}(s, \beta_e)$ with the β_e substituted in terms of p_e as well as γ_e. One can see here that to each value of l one can associate a scattering kernel or redistribution function $P_{l,0}(s)$. The scattering kernel associated with the monopole term is actually related to the scattering kernel for the isotropic case as follows:

$$P_{0,0} = \frac{1}{\sqrt{4\pi}} P_1(s). \tag{5.77}$$

The scattering kernels for each l value conserve the property written as follows:

$$P_{l,0}(-s) = e^{-3s} P_{l,0}(s). \tag{5.78}$$

The change in the intensity for each value of l can then be computed as follows:

$$\begin{aligned} \frac{\partial I}{\partial \tau}(x,\hat{z}) &= \sum_{l=0}^{\infty} \int_{-\infty}^{\infty} P_{l,0}(s) I_{l,0}(e^{-s}x) ds - I(x,\hat{z}) = \\ &= \sum_{l=0}^{\infty} \int_{-\infty}^{\infty} P_{l,0}(s) I_{l,0}(e^{-s}x) ds - \sqrt{\frac{2l+1}{4\pi}} I_{l,0}(x,\hat{z}), \end{aligned} \tag{5.79}$$

where

$$\begin{aligned} I(x,\hat{n}) &= \sum_{l=0}^{\infty} \sum_{m=-l}^{l} I_{l,m}(x) Y_{l,m}(\theta,\phi) = \\ &= 2(kT_0)^3 \left[\frac{x^3}{e^x - 1} + \frac{e^x x^4}{(e^x-1)^2} \sum_{l=2}^{\infty} \sum_{m=-l}^{l} a_{l,m} Y_{l,m}(\theta,\phi) \right]. \end{aligned} \tag{5.80}$$

From this one can see:

$$\begin{aligned} I_{0,0}(x) &= 2\ \sqrt{4\pi}(kT_0)^3 \frac{x^3}{e^x - 1} = 2\ \sqrt{4\pi}(kT_0)^3 F_0(x), \\ I_{2,2}(x) &= 2\ a_{2,2}(kT_0)^3 \frac{e^x x^4}{(e^x-1)^2} = 2\ a_{2,2}(kT_0)^3 F_1(x), \\ I_{3,2}(x) &= 2\ a_{3,2}(kT_0)^3 \frac{e^x x^4}{(e^x-1)^2} = 2\ a_{3,2}(kT_0)^3 F_1(x). \end{aligned} \tag{5.81}$$

In eq 5.79 we have used the relation

$$P_l^0(1) = 1. \tag{5.82}$$

5.2.4 CMB multipoles and polarization of the SZE

Now we proceed to do the same in deriving the Stokes parameters Q and U for an incident anisotropic radiation. The Stokes parameter Q can be written as

follows:

$$\frac{1}{\nu_1^3}\frac{\partial Q}{\partial \tau}(\nu_1) = -\frac{3}{64\pi^2}\sum_{l=0}^{\infty}\sum_{m=-l}^{l}\int d\beta_e d\mu_e d\phi_e \frac{f_e(\beta_e)}{\gamma_e}\int \frac{d\mu_2 d\phi_0}{n_{12}n_{22}^4}\times$$
$$\times\big[\cos(2\phi_0+2\phi_e)\sin^2(\theta_2)n_{12}^2+2\cos(\phi_0+2\phi_e)\times$$
$$\times\sin(\theta_2)\sin(\theta_e)n_{12}r_{12}\gamma_e\beta_e+\cos(2\phi_e)\sin^2(\theta_e)r_{12}^2\beta_e^2\gamma_e^2\big]\times$$
$$\times\sqrt{\frac{2l+1}{4\pi}\frac{(l-m)!}{(l+m)!}}e^{im(\phi_0+\phi_e)}P_l^m(\mu_2)f_{l,m}\left(\frac{n_{12}}{n_{22}}\nu_1\right). \quad (5.83)$$

Upon integration with respect to ϕ_e only the terms with $m=\pm 2$ survive and we make use of the following property of the associated Legendre Polynomials

$$P_l^{-m}(\mu)=(-1)^m\frac{(l-m)!}{(l+m)!}P_l^m(\mu), \quad (5.84)$$

and we also impose the following condition on the photon redistribution function

$$f_{l,m}^*(\nu)=(-1)^m f_{l,-m}(\nu). \quad (5.85)$$

The Stokes parameter Q then is written as follows:

$$\frac{1}{\nu_1^3}\frac{\partial Q}{\partial \tau}(\nu_1) = -\frac{3}{16\pi}\sum_{l=2}^{\infty}\sqrt{\frac{2l+1}{4\pi}\frac{(l-2)!}{(l+2)!}}\int d\beta_e d\mu_e \frac{f_e(\beta_e)}{\gamma_e}\times$$
$$\times\int\frac{d\mu_2 d\chi_0}{n_{12}n_{22}^4\sqrt{1-\chi_0^2}}\big[(1-\mu_2^2)n_{12}^2+2n_{12}\beta_e\gamma_e(\mu_2-1)\times$$
$$\times\chi_0\sqrt{(1-\mu_2^2)(1-\mu_e^2)}+\beta_e^2\gamma_e^2(\mu_2-1)^2(1-\mu_e^2)(2\chi_0^2-1)\big]\times$$
$$\times Re\big[f_{l,2}\left(\frac{n_{12}}{n_{22}}\nu_1\right)\big]P_l^2(\mu_2). \quad (5.86)$$

Similarly the Stokes parameter U can be written like the previous one

$$\frac{1}{\nu_1^3}\frac{\partial U}{\partial \tau}(\nu_1) = \frac{3}{16\pi}\sum_{l=2}^{\infty}\sqrt{\frac{2l+1}{4\pi}\frac{(l-2)!}{(l+2)!}}\int d\beta_e d\mu_e \frac{f_e(\beta_e)}{\gamma_e}\int\frac{d\mu_2 d\chi_0}{n_{12}n_{22}^4\sqrt{1-\chi_0^2}}\times$$
$$\times\big[(1-\mu_2^2)n_{12}^2+2n_{12}\beta_e\gamma_e(\mu_2-1)\chi_0\sqrt{(1-\mu_2^2)(1-\mu_e^2)}+$$
$$+\beta_e^2\gamma_e^2(\mu_2-1)^2(1-\mu_e^2)(2\chi_0^2-1)\big]\times$$
$$\times Im\big[f_{l,2}\left(\frac{n_{12}}{n_{22}}\nu_1\right)\big]P_l^2(\mu_2). \quad (5.87)$$

One can see that in the relativistic case we don't have only the quadrupole which contributes to the polarization but also higher order poles like octopoles etc depending on the value of l. These expressions can actually be simplified further into the following equations similar to those used to compute for the intensity I

$$\begin{aligned}
\frac{1}{\nu_1^3}\frac{\partial Q}{\partial \tau}(\nu_1) &= \sum_{l=0}^{\infty}\int_{-\infty}^{\infty} P_{l,2}(s) Re\big[f_{l,2}(e^s\nu_1)\big], ds \\
\frac{1}{\nu_1^3}\frac{\partial U}{\partial \tau}(\nu_1) &= -\sum_{l=0}^{\infty}\int_{-\infty}^{\infty} P_{l,2}(s) Im\big[f_{l,2}(e^s\nu_1)\big], ds \\
P_{l,2}(s) &= \int_{\sinh(|s|/2)}^{\infty} P_{l,2}(s,p_e) f_e(p_e) dp_e,
\end{aligned}$$

$$\begin{aligned}
P_{l,2}(s,\beta_e) &= -\frac{3}{32\pi}\sqrt{\frac{2l+1}{4\pi}\frac{(l-2)!}{(l+2)!}}\frac{e^{\frac{3}{2}s}}{\gamma_e^2\beta_e^2}\int_{-t_0}^{t_0} e^{\frac{t}{2}} dt \times \\
&\quad \times \int_{A-B}^{A+B} d\mu_0 \frac{P_l^2(1+e^t(\mu_0-1))}{\sqrt{B^2-(A-\mu_0)^2}}\frac{\mu_0-1}{2+e^t(\mu_0-1)} \times \\
&\quad \times\big[(\mu_0-1)\big[2-e^t\big(\gamma_e^2(\mu_0-1)(1+\beta_e^2)-2\big)\big] + \\
&\quad -8\gamma_e(\mu_0-1)e^{t/2}\cosh(\frac{s}{2}) - 4\cosh s\big]. \qquad (5.88)
\end{aligned}$$

The redistribution kernel $P_{l,2}(s)$ follows a similar kind of relationship as that of $P_{l,0}(s)$ written as follows:

$$P_{l,2}(-s) = e^{-3s}P_{l,2}(s). \qquad (5.89)$$

We compute the scattering kernel $P_{l,m}(s)$ for two types of electron populations, namely thermal and non-thermal electron populations. This allows us to cast the Stokes parameters Q and U in terms of the intensity:

$$\begin{aligned}
\frac{\partial Q}{\partial \tau}(x) &= \sum_{l=2}^{\infty}\int_{-\infty}^{\infty} P_{l,2}(s) Re\big[I_{l,2}(e^{-s}x)\big] ds, \\
\frac{\partial U}{\partial \tau}(x) &= -\sum_{l=2}^{\infty}\int_{-\infty}^{\infty} P_{l,2}(s) Im\big[I_{l,2}(e^{-s}x)\big] ds. \qquad (5.90)
\end{aligned}$$

These last equations allow one to compute the Stokes parameters Q and U for any value of l. In this work we computed only to $l = 2$. We show in Fig 5.3 and

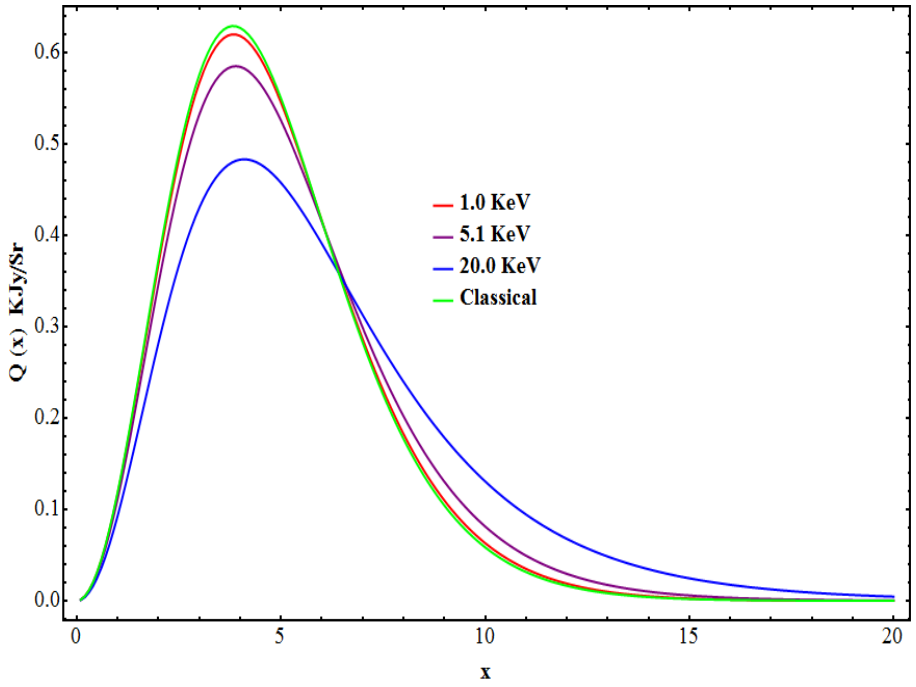

Figure 5.3: The spectrum of the Stokes parameter Q for different temperature of the plasma arising from the quadrupole of the CMB, assumed here to be $a_{2,2} = 3 \times 10^{-4}$.

Fig 5.4 the spectrum of the Stokes Q parameter arising from the quadrupole and the octopole of the CMB for different temperature of a thermal plasma.The Stokes parameters Q and U can also be written for superposing contribution of the quadrupole $a_{2,2} = 3 \times 10^{-4}$ and octupole $a_{3,2} = 7 \times 10^{-4}$ as follows:

$$\begin{aligned} \frac{\partial Q}{\partial \tau}(x) &= \int_{-\infty}^{\infty} P_{2,2}(s) Re[a_{2,2}] F_1(e^{-s}x) ds + \int_{-\infty}^{\infty} P_{3,2}(s) Re[a_{3,2}] F_1(e^{-s}x) ds, \\ \frac{\partial U}{\partial \tau}(x) &= -\int_{-\infty}^{\infty} P_{2,2}(s) Im[a_{2,2}] F_1(e^{-s}x) ds - \int_{-\infty}^{\infty} P_{3,2}(s) Im[a_{3,2}] F_1(e^{-s}x) ds. \end{aligned} \tag{5.91}$$

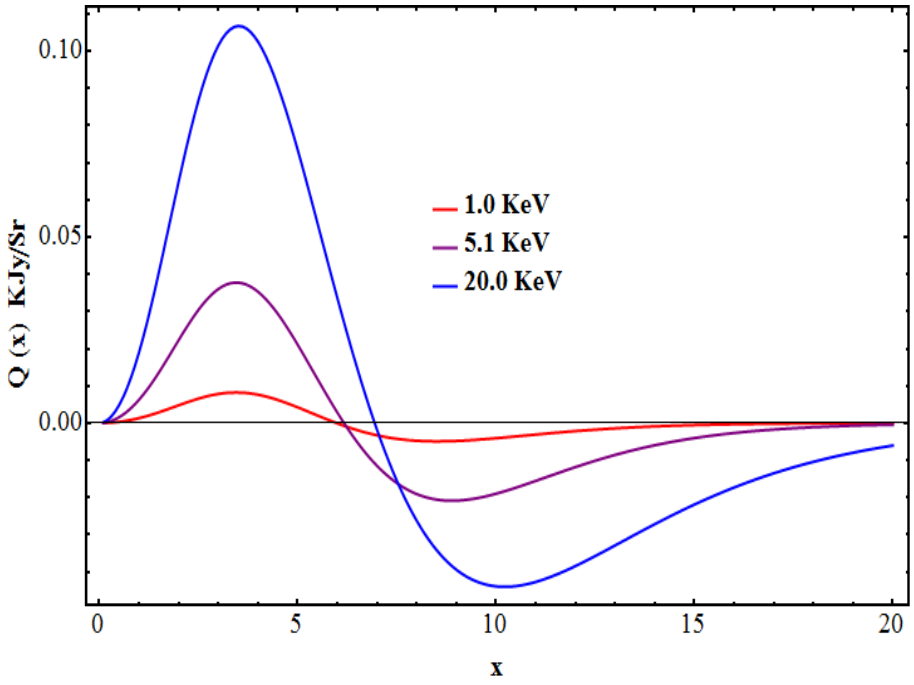

Figure 5.4: The spectrum of the Stokes parameter Q for different temperature of the plasma arising from the quadrupole of the CMB, assumed here to be $a_{3,2} = 7 \times 10^{-4}$.

5.2.5 Combination of two electron populations

Using this formalism one can also compute the total Polarization SZE due to two electron populations residing in the same ICM. This was done by Colafrancesco et al. (2003) for the case of intensity only while this time we will do it for the Stokes parameter Q and U in the case of the quadrupole and octopole. We write the distribution function of the electron $f_e(p)$ as follows:

$$f_e(p) = C_A f_{e,A}(p) + C_B f_{e,B}(p), \tag{5.92}$$

where $f_{e,A}(p)$ correspond to the distribution function of electron population A and $f_{e,B}(p)$ correspond to the distribution function of electron population B. C_A and C_B are normalization constants with $C_A + C_B = 1$ (see Colafrancesco

et al. 2003) and

$$C_A = \frac{\tau_A}{\tau},$$
$$C_B = \frac{\tau_B}{\tau}, \tag{5.93}$$

with $\tau = \tau_A + \tau_B$. The total scattering kernel for any value of m and l due to the combination of population A and B is written as follows:

$$\begin{aligned} P_{l,m}(s) &= \int f_e(p)\ P_{l,m}(s,p)\ dp \\ &= \int C_A f_{e,A}(p) P_{l,m}(s,p) + C_B f_{e,B}(p) P_{l,m}(s,p)\ dp \\ &= C_A P_{l,m,A}(s) + C_B P_{l,m,B}(s). \end{aligned} \tag{5.94}$$

The Stokes parameters I can be written as:

$$\begin{aligned} \frac{\partial I}{\partial \tau}(x,\hat{z}) &= \frac{\tau_A}{\tau}\sum_{l=0}^{\infty}\int_{-\infty}^{\infty} P_{l,0,A}(s) I_{l,0}(e^{-s}x) ds + \\ &\quad + \frac{\tau_B}{\tau}\sum_{l=0}^{\infty}\int_{-\infty}^{\infty} P_{l,0,B}(s) I_{l,0}(e^{-s}x) ds - \sqrt{\frac{2l+1}{4\pi}} I(x,\hat{z}), \end{aligned} \tag{5.95}$$

and the Stokes parameters Q and U are written as:

$$\begin{aligned} \frac{\partial Q}{\partial \tau}(x,\hat{z}) &= \frac{\tau_A}{\tau}\sum_{l=0}^{\infty}\int_{-\infty}^{\infty} P_{l,2,A}(s) Re[I_{l,2}(e^{-s}x)] ds + \\ &\quad + \frac{\tau_B}{\tau}\sum_{l=0}^{\infty}\int_{-\infty}^{\infty} P_{l,2,B}(s) Re[I_{l,2}(e^{-s}x)] ds \\ \frac{\partial U}{\partial \tau}(x,\hat{z}) &= -\frac{\tau_A}{\tau}\sum_{l=0}^{\infty}\int_{-\infty}^{\infty} P_{l,2,A}(s) Im[I_{l,2}(e^{-s}x)] ds + \\ &\quad - \frac{\tau_B}{\tau}\sum_{l=0}^{\infty}\int_{-\infty}^{\infty} P_{l,2,B}(s) Im[I_{l,2}(e^{-s}x)] ds. \end{aligned} \tag{5.96}$$

We present in Appendix A the different re-distribution functions of the two electron populations namely thermal and non-thermal.

5.2.6 SZE polarization due to finite optical depth

Another contribution to the polarization of the SZE , as mentioned in the first chapter, comes from double scattering of a photon off electrons. Consider an electron at the origin in the (X, Y, Z) coordinate system as shown in Fig 5.5. The first electron scatters the CMB radiation and causes a SZE. The distorted radiation introduce by the first electron, in the non-relativistic limit, along the direction (θ, ϕ) is written as

$$\Delta I(x, \theta, \phi) = 2(kT_0)^3 \frac{k_B T_e}{m_e c^2} \tau_e(\theta, \phi) g(x). \tag{5.97}$$

The optical depth $\tau_e(\theta, \phi)$ is written

$$\tau_e(\theta, \phi) = \int_{\hat{n_1}} \sigma_T n_e(r, \theta, \phi)\ dl \tag{5.98}$$

where $\hat{n_1}$ points from the first electron towards the second electron and the integration is performed along this direction. The second electron sees an anisotropic incoming radiation due to the dependence of the optical depth on direction, $\tau_e(\theta, \phi)$, and when it scatters it into the line of sight produces polarization. The Stokes parameters are then written in this case as

$$Q(x) = \frac{3}{16\pi} \tau_{e,z} \left[2\ (kT_0)^3 g(x) \right] \int \sin^2(\theta) \cos(2\phi)\ \frac{k_B T_e}{m_e c^2} \tau_e(\theta, \phi)\ d\Omega, \tag{5.99}$$

$$U(x) = \frac{3}{16\pi} \tau_{e,z} \left[2\ (kT_0)^3 g(x) \right] \int \sin^2(\theta) \sin(2\phi)\ \frac{k_B T_e}{m_e c^2} \tau_e(\theta, \phi)\ d\Omega. \tag{5.100}$$

Here $\tau_{e,z}$ is the optical depth along the line of sight. This was derived by Sazonov & Sunyaev 1999. This is the non-relativistic approach for computing polarization due to finite optical depth. The formalism that we used in the previous sections allows us to be able to extend it into the full relativistic regime. The argument is much the same as in the non-relativistic case except that we need to take into account the fact that the radiation will be upscattered again by the second electron.The radiation after being scattered by the first electron can be written as follows

$$I'(x, \theta, \phi) = I(x, \theta, \phi) + \tau(\theta, \phi) \frac{\partial I'(x)}{\partial \tau}, \tag{5.101}$$

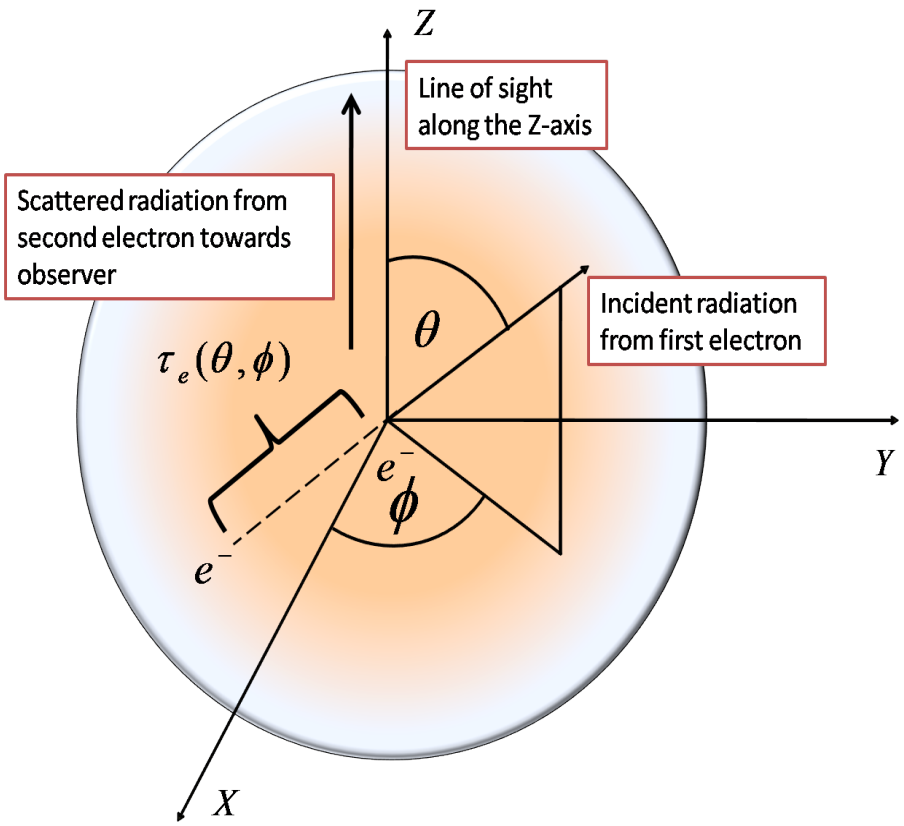

Figure 5.5: The scattering geometry for double scattering.The second electron is located at the origin of the coordinate system and it receives a radiation from the first electron in the direction (θ, ϕ). The first electron has already introduced a SZE and the second electron sees an anisotropy in the radiation because of the directional dependence of the optical depth $\tau_e(\theta, \phi)$. The second electron then generates polarization when it Thomson scattered the radiation received from the first electron.

where

$$\frac{\partial I'(x)}{\partial \tau} = \int_{-\infty}^{\infty} P_{0,0}(s) I_{0,0}(e^{-s}x) ds - \sqrt{\frac{1}{4\pi}}\, I_{l,0}(x, \hat{z}). \tag{5.102}$$

Note that $I'(x, \theta, \phi)$ is the scattered radiation by the first electron and $I(x, \theta, \phi)$ is the incoming radiation towards the first electron. One can notice that this last

equation can be intepreted as if the second electron is receiving an anisotropic radiation having a primordial anisotropy plus an anisotropy due to directional dependence of the optical depth. Inserting this equation into equation 5.83, we can deduce that

$$I'_{l,m}(x) = I_{l,m}(x) + \tau_{l,m}\frac{\partial I}{\partial \tau}(x). \tag{5.103}$$

The Stokes parameter $Q(x)$ is then written as

$$\frac{\partial Q}{\partial \tau}(x) = \sum_{l=2}^{\infty}\int_{-\infty}^{\infty} P_{l,2}(s) Re\big[I_{l,2}(xe^{-s}) + \tau_{l,2}\frac{\partial I}{\partial \tau}(xe^{-s})\big] d\ s. \tag{5.104}$$

One can also write

$$\frac{\partial I}{\partial \tau}(xe^{-s}) = \int_{-\infty}^{\infty} P_{0,0}(t-s) I_{0,0}(xe^{-t}) d\ t - \frac{I_{0,0}(xe^{-s})}{\sqrt{4\pi}}, \tag{5.105}$$

Then substituting this into equation 5.104 we obtain

$$\frac{\partial Q}{\partial \tau}(x) = \sum_{l=2}^{\infty}\int_{-\infty}^{\infty} P_{l,2}(s) Re\big[I_{l,2}(xe^{-s})\big] d\ s +$$

$$Re[\tau_{l,2}]\int_{-\infty}^{\infty}\int_{-\infty}^{\infty} P_{l,2}(t) P_{0,0}(s-t) I_{0,0}(xe^{-s}) d\,t d\,s - \frac{1}{\sqrt{4\pi}}\int_{-\infty}^{\infty} P_{l,2}(s) I_{0,0}(xe^{-s}) d\,s, \tag{5.106}$$

which can be re-written as

$$\frac{\partial Q}{\partial \tau}(x) = \sum_{l=2}^{\infty}\int_{-\infty}^{\infty} P_{l,2}(s)\ Re\big[I_{l,2}(xe^{-s})\big] ds + Re[\tau_{l,2}]\int_{-\infty}^{\infty}\left[P''_{l,2}(s) - \frac{1}{\sqrt{4\pi}} P_{l.2}\right] I_{0,0}(xe^{-s})\ d\,s, \tag{5.107}$$

where

$$P''_{l,2}(s) = P_{l,2}(s) \star P_{0,0}(s). \tag{5.108}$$

The effect is still of the order of τ^2 and is of order of τ less than the polarization arising from the primordial multipoles of the CMB.

5.2.7 SZE polarization due to tranverse motion of cosmic structures

We mentioned in the first chapter that the component of the peculiar velocity (see Sazonov & Sunyaev 1999) of a cosmic structure along the line of sight

induces a kinetic SZE (kSZE). In addition to that, the transverse component of this peculiar velocity in turn produces a polarization. This is due to the directional dependence of the temperature of the CMB as viewed by a cosmic structure with a non-zero peculiar velocity. In the CMB frame, the spectrum of the radiation is isotropic and follows the spectrum of a blackbody with temperature T_0. Imagine now an electron moving in this radiation field at velocity $\vec{\beta_c}$ with respect to an observer fixed to the CMB frame. The spectrum of the CMB in the electron rest frame follows still that of a blackbody except that the temperature of the CMB will be directional dependent. The transformation of the CMB temperature between the electron rest frame and the observer frame is given by

$$T(\hat{n}) = \frac{T_0}{\gamma\big(1+\vec{\beta_e}.\hat{n}\big)} = \frac{T_0}{\gamma\big(1+\beta_c\ \delta(\theta,\phi)\big)}, \tag{5.109}$$

where $T(\hat{n})$ is the temperature of the CMB in the rest frame of the electron. The spectrum of the CMB in this frame is written as

$$I(x,\theta,\phi) = 2\ (kT_0)^3 \frac{x^3}{\exp\left[x\gamma_c(1+\beta_c\ \delta(\theta,\phi)\right]-1}. \tag{5.110}$$

The variable θ and ϕ define the velocity of the observer as seen in the electron rest frame $(-\vec{\beta_c})$. We then obtain, in the non-relativistic limit, the distortion of the radiation in the electron frame as

$$I(x,\delta) = 2\ (kT_0)^3 \left[F_0(x) - \frac{F_1(x)}{2}\beta_c\ \delta + \frac{F_2(x)}{4}\ \big(\beta_c\ \delta\big)^2\right], \tag{5.111}$$

where $F_2(x) = x\ \big[\big(e^x+1\big)/\big(e^x-1\big)\big]F_1(x)$. The variable $\delta(\theta,\phi)$ is the cosine of the angle between the velocity vector $\vec{\beta_c}$ and the direction $\hat{n}$ of the incoming radiation. As one can see, polarization will arise due to the quadrupole term $\big(\beta_c\ \delta\big)^2$. The Stokes parameters can be computed by inserting the expression of $I(x,\delta)$ into equation 5.1 and equation 5.2 and integrating over the variable θ and ϕ. The result is then obtain as

$$\frac{\partial Q}{\partial \tau}(x) = \frac{1}{20}\frac{(kT_0)^3}{(hc)^2}\beta_c^2 \sin^2\theta_c \cos 2\phi_c F_2(x), \tag{5.112}$$

and

$$\frac{\partial U}{\partial \tau}(x) = \frac{1}{20}\frac{(kT_0)^3}{(hc)^2}\beta_c^2 \sin^2\theta_c \sin 2\phi_c F_2(x). \tag{5.113}$$

where $\beta_T = \beta_c \sin\theta_c$ is the transverse component of the peculiar velocity of the cosmic structure. Transforming back into the CMB frame leaves the Stokes parameters intact as far as terms up to β_c^2 are concerned. Even though our present analysis is in the non-relativistic regime, it is a good approximation since cosmic structure peculiar velocity is rarely greater than 1000 km/s.

Chapter 6

Structure of astrophysical plasmas

Studying the SZE in various cosmic atmospheres provides many insights on their energetics, pressure and dynamical structure. The combination of SZE with other emission mechanisms related to the same particle distribution (i.e., synchrotron, high-E ICS emission, bremsstrahlung emission) provides further information on the radiation, matter and magnetic fields that are co-spatial with the electrons producing the SZE. These properties of the SZE concern various cosmic structures, from galaxy clusters to radiogalaxy lobes, from galaxy halos to supercluster and the WHIM (see Colafrancesco 2012 for a review).

The redshift-independent nature of the SZE allowto use this effect as a powerful cosmological probe by using both the redshift evolution of cluster abundance and direct probes of cosmological parameters.The SZE has a wide range of cosmological applications: it can be used to determine the main cosmological parameters and the Dark Energy (DE) equation of state, and also set constraints to modified Gravity scenarios and to the properties of primordial magnetic fields (see Colafrancesco 2012 for a review).

6.1 Plasma structure from SZE polarization

We have seen that the Stokes parameters arising from the CMB primordial anisotropy are proportional to the optical depth along the line of sight. This can allow us to probe the spatial distribution of the plasma on the plane of the sky. For example if the plasma spatial distribution is constant, then the polarization arising from the Q Stokes parameter will be horizontal throughout the cosmic structure. Fig 6.1 shows the Linear polarization arising from the primordial quadrupole of the CMB for an isothermal beta model with spherical spatial distribution of the plasma. The optical depth, using this density profile,

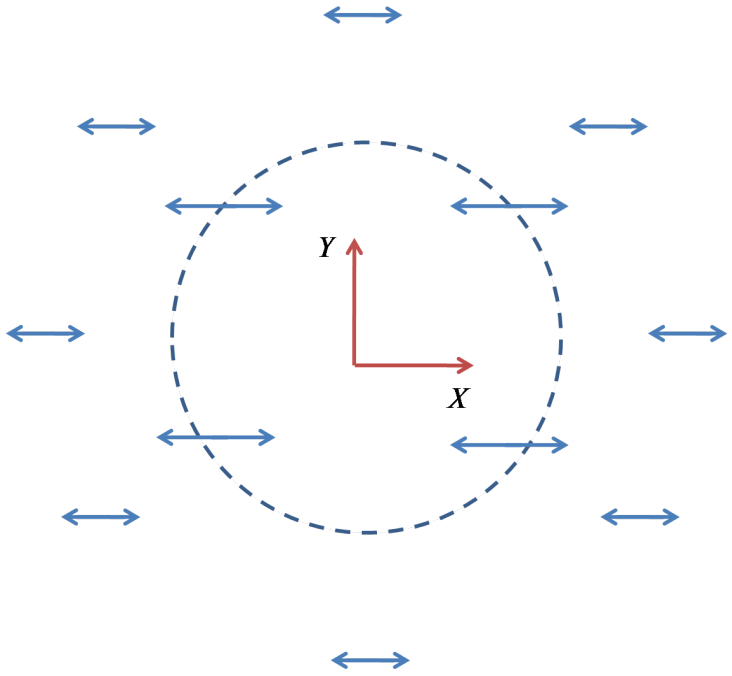

Figure 6.1: The Q Stokes parameter arising from the primordial anisotropy of the CMB for a spherical plasma distribution. The green curve represents the Stokes parameter in the non-relativistic domain.

can be written as follows

$$\tau_e(\theta) = n_{e0}\sigma_T r_c Z(\theta), \tag{6.1}$$

where θ is the angular separation between the cluster center and the point of observation. The function $Z(\theta)$ is written as

$$Z(\theta) = \sqrt{\pi}\frac{\Gamma\left(3\beta/2 - 1/2\right)}{\Gamma\left(3/2\beta\right)}\left[1 + \left(\frac{\theta}{\theta_c}\right)^2\right]^{1/2-3/2\beta}. \tag{6.2}$$

Any deviation from spherical symmetry will result in polarization pattern which is more complicated. In addition to that, we noticed that the Stokes parameters also have different spectral features depending on the temperature and hence polarization of the SZE reveals itself as a probe for temperatures of cosmic structures. The polarization arising from multiple scattering can be used to

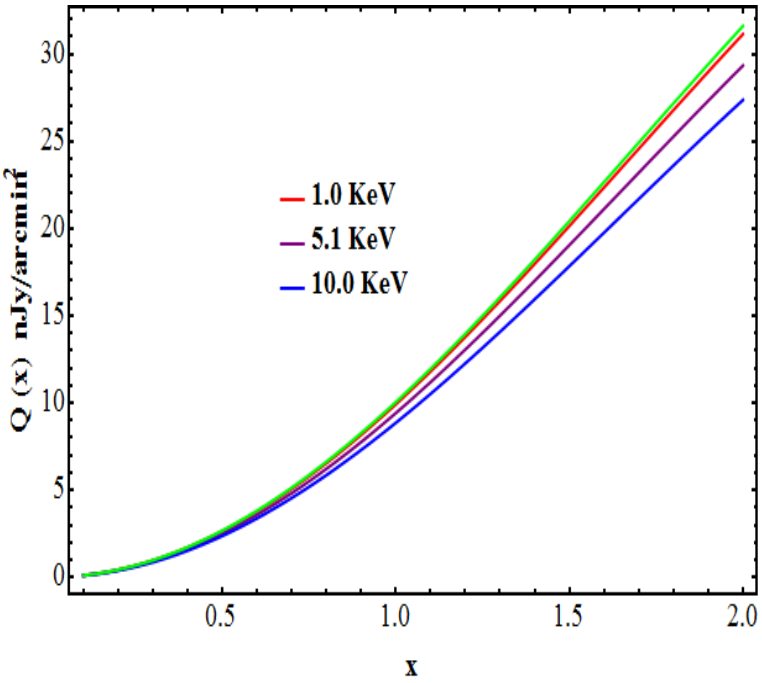

Figure 6.2: The Stokes parameter Q associated with the quadrupole of the CMB for different plasma temperatures at low frequencies.

probe the homogeneity and isotropy of the plasma inhabiting cosmic structures and this effect is of the order of τ_e^2. The shape of the Stokes parameters spectrum follows that of the SZE in intensity except that it is supressed by the term τ_e^2.

The optical depth in a given direction can be written as

$$\tau_e(\theta,\phi) = \sum_{l=0}^{\infty}\sum_{m=-l}^{l} \tau_{l,m} Y_{l,m}\big(\theta,\phi\big). \tag{6.3}$$

Using this then the Stokes parameters can be written as

$$Q(x) = \frac{1}{2}\sqrt{\frac{3}{10\pi}}\frac{k_B T_e}{m_e c^2} Re[\tau_{2,2}]\tau_{e,z}\bigg[\ 2\ (kT_0)^3 g(x)\bigg], \tag{6.4}$$

and

$$U(x) = \frac{1}{2}\sqrt{\frac{3}{10\pi}}\frac{k_B T_e}{m_e c^2} Im[\tau_{2,2}]\tau_{e,z}\bigg[\ 2\ (kT_0)^3 g(x)\bigg]. \tag{6.5}$$

For sphericallly symmetric plasmas, the polarization pattern will be radial at frequencies less than the cross-over frequency, $x_0 \approx 3.83$, and circular at frequencies higher than this as pointed out by Sazonov & Sunyaev 1998.

6.2 Reconstruction of peculiar velocity field

The kinetic SZE in intensity is directly related to the component a cosmic structure's peculiar velocity along the line of sight. The polarization on the other hand is directly related to the transverse component of the peculiar velocity. Combining both should allow the complete reconstruction of the peculiar velocity of the cosmic structure. During merger events in galaxy clusters, substructures formed can move with very high peculiar velocities and in these cases the kSZ effect is more pronounced than the thermal SZE (Ruan et al. 2013). Simulation of a merger event in a galaxy cluster was performed by Ruan et al. 2013. Fig.6.3 shows the Compton parameter y of the gas along the line of sight for each pixel. There are two substructures A and B that shows high peculiar velocities. The SZE, both thermal and kinematic, associated with these structures are shown in Figure 6.4.

In addition to the spectral distortion in the intensity, substructures A and B will also show a polarization to due to the transverse component of their peculiar velocities. Fig 6.5 and Fig 6.6 shows the Q Stokes parameter spectrum for substructures A and B arising from their respective substructure transverse

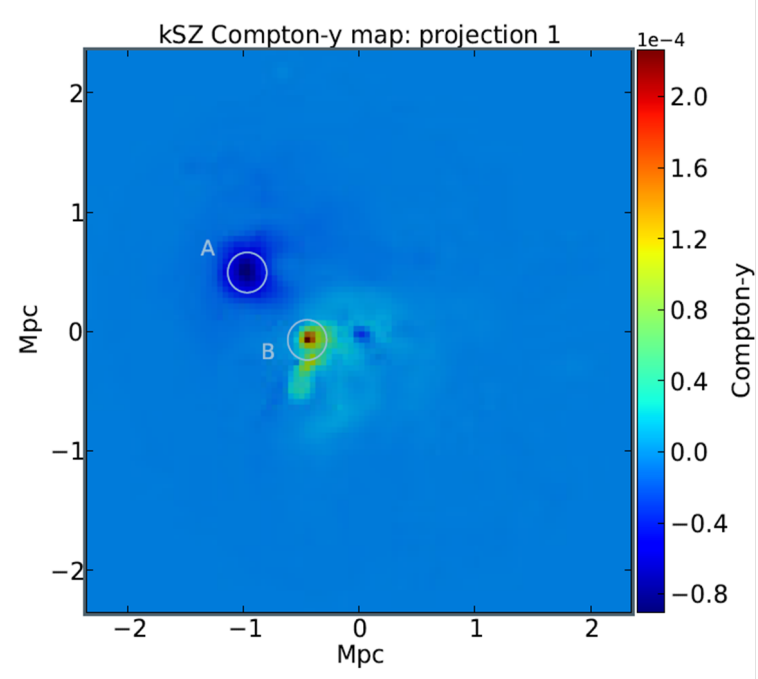

Figure 6.3: The encircle regions A and B represent two substructures moving with peculiar velocities -1150 km/s and 2492 km/s along the line of sight (Ruan et al. 2013.).

veloctiy, where a value β_T of 0.01 is assumed for A and 0.02 for B. The direction of the polarization will be orthogonal to the peculiar velocity.

6.3 SZE polarization from radio galaxy lobes and radio relics

Radiogalaxy lobes (RG) are excellent cosmic structures hosting a plasma containing non-thermal components. Polarized synchrotron emissions and Faraday rotation measurements of RG lobes testify the presence of tangled magnetic fields and the existence of relativistic electrons.For example the radiogalaxy RG 0208+35 shows a value of $B = 0.8\mu$G at the center of its lobe (Guidetti et al.

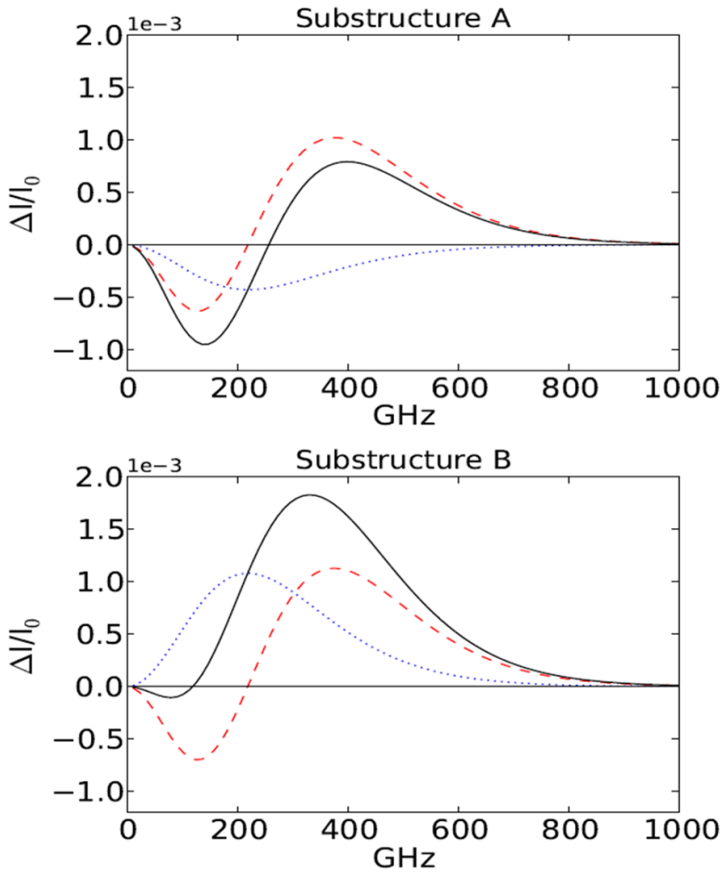

Figure 6.4: The thermal (red) and kinetic SZE (blue) spectral distortions for structures A and B. The black curve shows the spectral distortion arising from the superposition of both components (Ruan et al. 2013.).$I_0 = 2(k_B T_0)^3/(hc)^2$

2011).Complementary studies of RG lobes also show extended X-ray emission (Erlund et al. 2006) and the mechanism attributed to these observations is inverse Compton scattering of the CMB photons (ICCMB) by relativistic electrons confined in these lobes. It has been shown also that these electrons can actually diffuse over large intergalactic volumes and penetrate giant cavities of galaxy clusters. The presence of ICCMB in these structures leads to the expectation of a SZE from them. Predicted SZE within this context have been

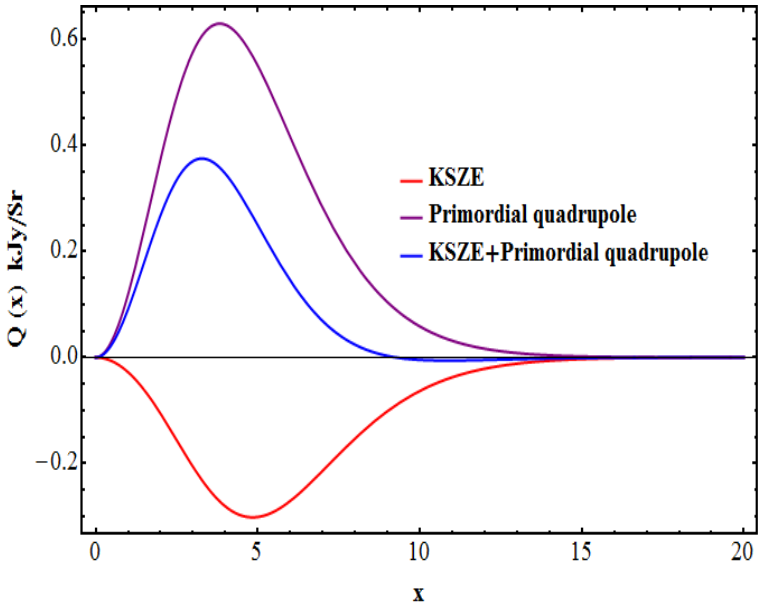

Figure 6.5: The Q Stokes parameter spectrum for substructure A for an optical depth $\tau_e = 0.01$. The red curve shows the KSZE spectrum and the purple curve shows the primordial anisotropy spectrum. The blue curve shows the superposition of the two.

computed by Colafrancesco et al 2012 and shown in Figure 6.7. We compute on the other hand, the Stokes parameter Q arising from the relativistic electrons that inhabit these radio lobes as shown in Figure 6.8 and Figure 6.9. Since SZE in intensity is expected, its polarization also follows. In Fig 6.8 and 6.9 we show respectively the expected spectrum of the Stokes parameter $Q(x)$ associated with the quadrupole and the octopole of the CMB. Connections between the radio relics of galaxy clusters and radio galaxy lobes have also been anticipated (see e.g.,Feretti et al. 2012, Keshet et al. 2004, Miniati et al. 2001). Particle acceleration/re-acceleration in galaxy clusters can be provided by first order Fermi processes (Shock acceleration) and observations have shown that shock accelerations are linked to relics. The electrons that are accelerated during these shocks can be from the thermal ICM or from radio galaxies. So a possible

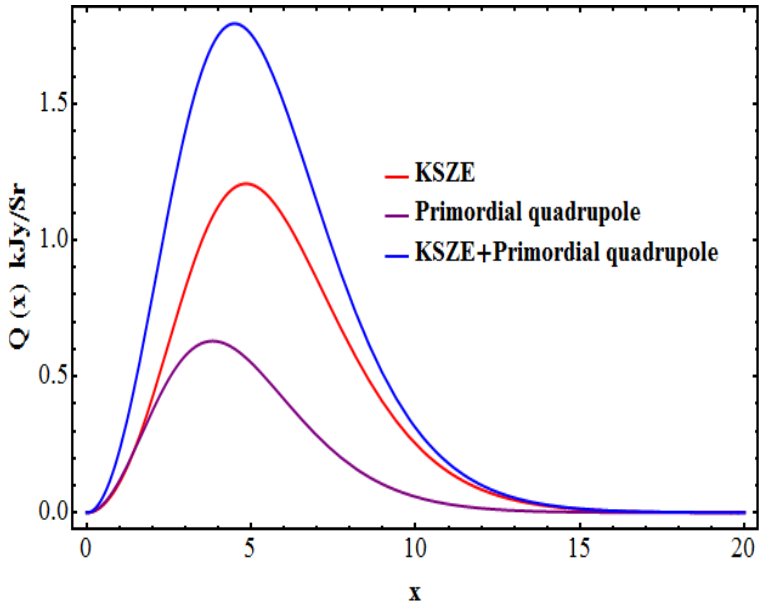

Figure 6.6: The Q Stokes parameter spectrum for substructure B for an optical depth $\tau_e = 0.01$. The red curve shows the KSZE spectrum and the purple curve shows the primordial anisotropy spectrum. The blue curve shows the superposition of the two.

thermal SZE contaminated with non-thermal ones is expected. Polarization ($\approx$ 30 %) is also assiociated with relics from synchrotron radio emissions. These electrons responsible for these synchrotron emissions can also generate SZE polarization. The SZE polarization associated with relativistic electrons, following a single power law spectrum, in a pool of thermal electrons has been computed and shown in Figure 6.10 and Figure 6.11.

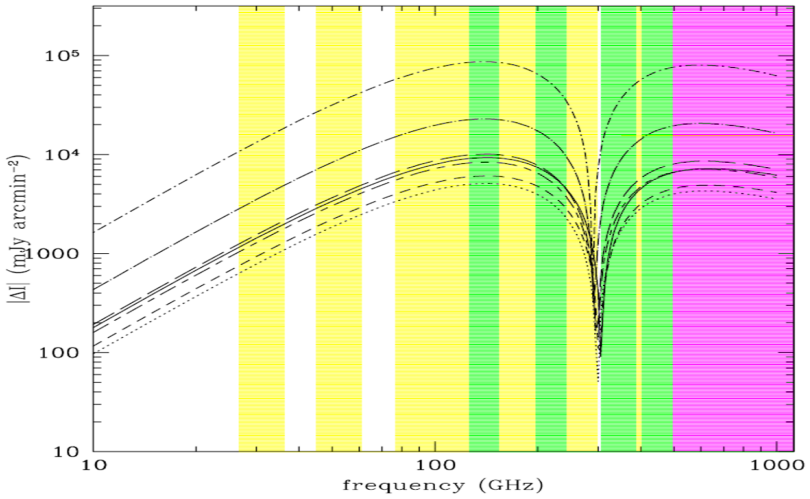

Figure 6.7: The SZE expected from a set of radio galaxies considered by Colafrancesco et al. 2012.

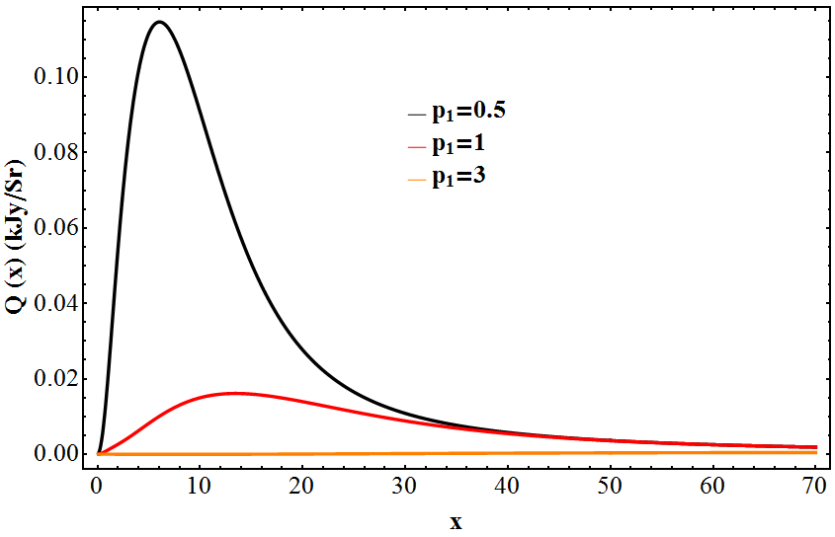

Figure 6.8: The spectrum of the Stokes parameter $Q(x)$ associated with the quadrupole of the CMB, computed for the relativistic electrons that inhabit RG lobes.

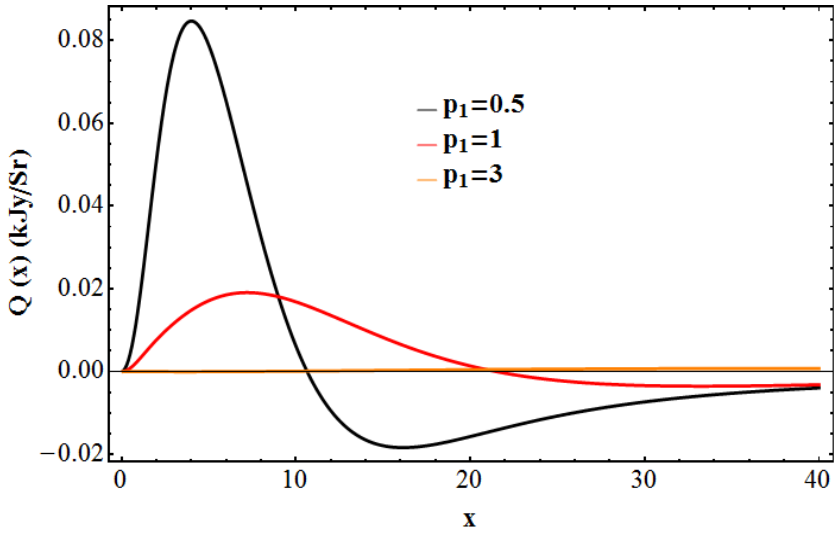

Figure 6.9: The spectrum of the Stokes parameter $Q(x)$ associated with the octopole of the CMB, computed for the relativistic electrons that inhabit RG lobes.

6.4 Testing the homogeneity of the Universe with the SZE

We have seen until now how the SZE and its polarization can be used to probe the energetic, content as well as spatial distribution of the plasmas that inhabit various cosmic structures from galaxy clusters to radio galaxies. The SZE and its complementary component, polarization, has also its relevancy in cosmological context. In this section we analyse the power of the SZE and its polarization in answering fundamental cosmological issues. We concentrate here on how the SZE can be used to probe the homogeneity of the matter distribution in the cosmos. The question of whether we occupy a special position in the Universe is crucial for cosmological models of dark energy. Acccording to the Copernican principle, we do not occupy a special position. In the standard model of cosmology, the Copernican principle is a tenet in the theory but nevertheless, other cosmological models has also been proposed such as Le-Maitre-Tolman

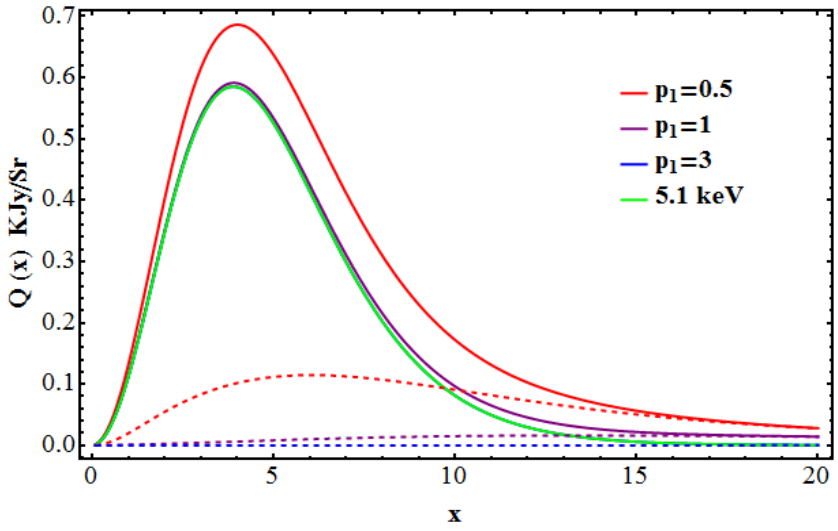

Figure 6.10: We show here the spectrum of the Stokes parameter Q associated with the quadrupole for a thermal population (green) at 5.1 keV, a non-thermal population (dotted) and the combination of both.

Bondi(LTB) models which uses the LTB spacetime (see e.g., Caldwell & Stebbins 2007, Celerier 2000). Within this paradigm our location in the Universe could be near the center of a void. We also discuss the possibility of putting observational constraints on LTB models. The matter distribution about our location in the Universe is highly isotropic inferred from the observed CMB distribution on the sky and the high blackbody nature of its spectrum give us firm observational indication that the early Universe was in thermal equilibrium and highly uniform. Gravity and the expansion of the Universe are driving agents behind the result in which matter is distributed across, but how is matter distributed over the Universe as a whole?. The most general theory of gravity consistent with observations is the Einstein theory of gravity and the metric of the Universe, that is the FLRW metric, emerges from this theory on the assumption that the Universe is homogeneous over large scale (scale larger than galaxy clusters). If the Universe is homogeneous, then it means that all cosmic points are equivalent. This is what is known as the Copernican principle. Homogeneity

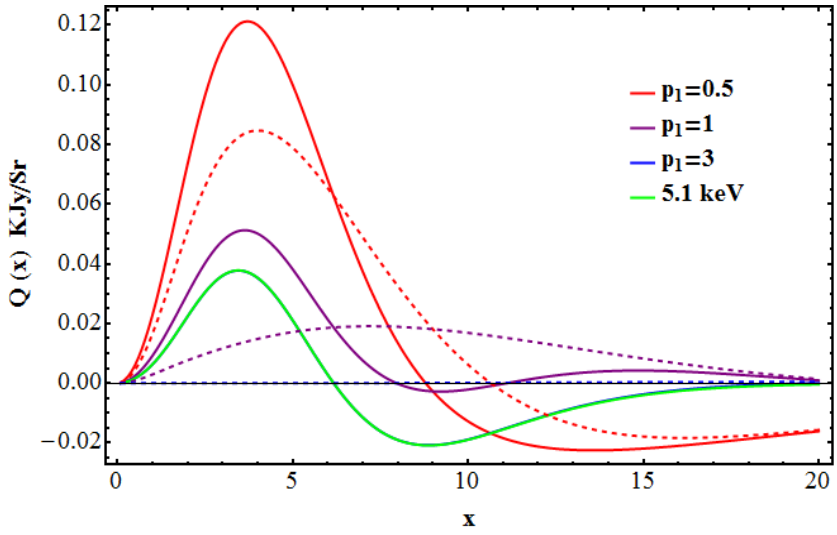

Figure 6.11: We show here the spectrum of the Stokes parameter Q associated with the octopole for a thermal population (green) at 5.1 keV, a non-thermal population (dotted) and the combination of both.

is not observationally based but an assumption due to the fact that we can only observe the distribution of matter from only one spacetime point as we cannot move from one point to another within the cosmic realm. The only way to test homogeneity is to link it to isotropy (Maartens 2011). This means that if the matter distribution is homogeneous then it automatically satisfies the criteria of being isotropic about any location. The question then boils down to the sphere of last scattering as seen by different observers at different cosmic locations across the Universe. Galaxy surveys cannot be used to probe homogeneity since we observe them down our past lightcone (Figure 6.12). Observing the CMB actually tell us about the matter distribution at the sphere of last scattering as seen by an observer located at a given spacetime point in the cosmos. If this observer see a near isotropic radiation then he can conclude that the matter distribution about its location is nearly isotropic. Testing the isotropy of matter distribution for different observers on large scale would allow us to probe homogeneity. The SZE together with its polarization will be an indication of

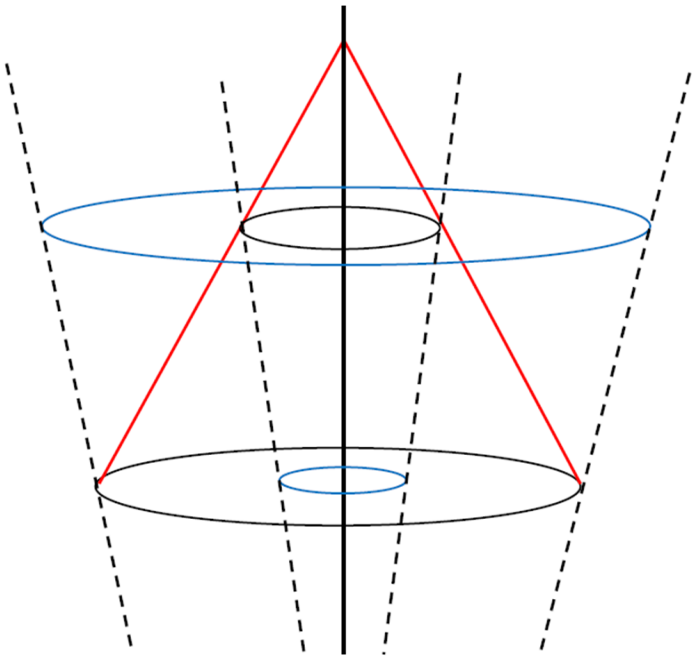

Figure 6.12: Galaxy surveys are snapshots of our past lightcone (Maartens 2011).

the level of anisotropy in the CMB as seen by observers at diifferent cosmic locations in the Universe.The SZE actually scatters the CMB photons into our past lightcone as illustrated in Figure 6.13 If large anisotropies are seen at different regions where galaxy clusters occupied, then this would definitely implies that they are seeing a different matter distribution compared to our location and this would violate the homogeneity assumption. A criteria for homogeneity is given by Maartens (2011) where it is stated that for all observers in a homogeneous Universe the vanishing of the dipole, quadrupole and octopole is a sufficient observational requirement to impose homogeneity. The polarization of the SZE allow us to access these higher multipoles at the different cluster locations in the Universe as the Stokes parameters are directly related to the multipoles. We show in Figure 6.14 the plot of the quadrupole and octopole at low frequencies.

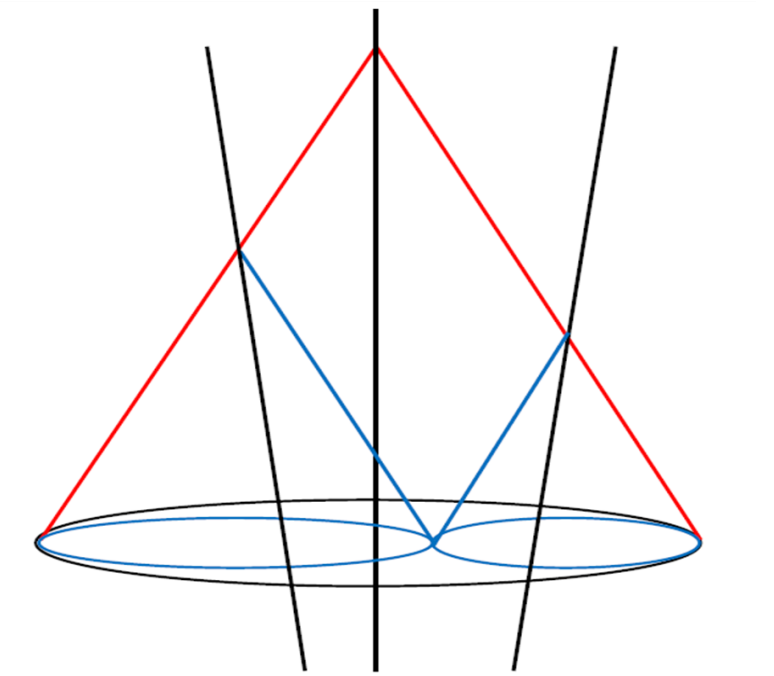

Figure 6.13: Scattering of CMB photons by galaxy clusters into our past light-cone (Maartens 2011).

Possible observational constraints can be put on LTB models as well through the kinetic SZE. LTB models predict that our spacetime location could be near the center of a void and these structures usually causes ionized gas to be expelled outward in a radial direction and would cause large peculiar velocties to be acquired by cosmic structures. Within the framework of LTBs, dark energy or a cosmological constant is not required and still able to produce a Hubble diagram (Bondi 1947) in good agreement with observations. Since the kinetic SZE can measure peculiar velocites, it would prove very crucial in probing these kinds of scenarios. The kinetic SZE polarization would also complement in the search for cosmic voids.

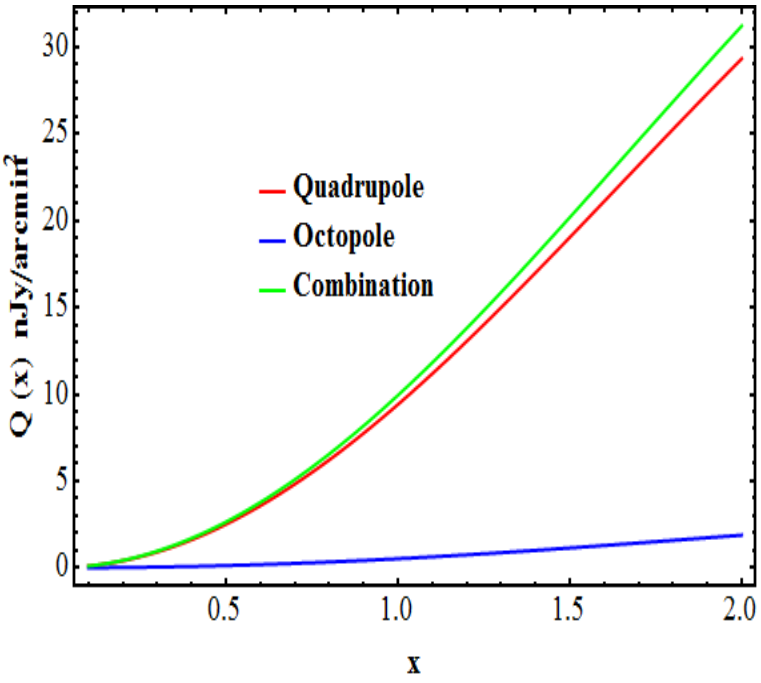

Figure 6.14: The quadrupole and the octopole at low frequencies for a plasma temperature of 5.1 keV.

Chapter 7

Conclusions and future outline

The main results obtained in this Thesis are related to the derivation of to the use of the polarization and intensity properties of the SZE in cosmic structures, like galaxy clusters and radio galaxies. We have further highlighted some of the possible use of the polarized SZE in cosmology.

As for the clusters of galaxies, we have been able to combine X-ray, radio and SZE measurements of a sample of clusters, selected from the all-sky Planck survey, to constrain the non-thermal pressure content of the largest sample of RH galaxy clusters observed by the Planck Collaboration. Since the SZE is directly related to the total particle pressure, thermal plus non-thermal, and that X-ray bolometric luminosity is directly related to only the thermal particle pressure, this allowed us to derive the ratio $X \equiv P_{non-th}/P_{th}$ between non-thermal and thermal pressure without any assumption concerning the magnetic field (as it is necessary using radio observations only). The positive value of X found for our cluster sample shows that RH clusters host a considerable amount of non-thermal electrons co-spatial with the ICM. The correlation between the ratio X and the X-ray luminosity L_X, $X \sim L_X^{-0.96}$, implies the existence of a relation

between the density distribution of thermal and non-thermal particles on the same spatial extent. This seems to be consistent with a scenario in which relativistic electrons and protons are injected at an early cluster age by one or more cosmic ray sources and then diffuse and accumulate in the cluster atmosphere but are eventually diluted by the infalling (accreting) thermal plasma. This fact is also consistent with the outcomes of relativistic covariant kinetic theories of shock acceleration in galaxy clusters (see, e.g., Wolfe and Melia 2006, 2008) that predict that the major effect of shocks and mergers is to heat the ICM (rather than accelerating electrons at relativistic energies): in such a case the relative contribution of non-thermal particles to the total pressure in clusters should decrease with increasing cluster temperature, or X-ray luminosity since these two quantities are strongly correlated.

Our results also show that the combination of multi-frequency observations of RH clusters at different wavelengths (radio, mm. and X-rays) is able to provide physical constraints on the non-thermal particle content of galaxy clusters. This is possible by combining the relevant parameters carrying information on the non-thermal (i.e. the total Compton parameter) and thermal (i.e. the X-ray bremsstrahlung luminosity) pressure components residing in the cluster atmosphere. The achievement of this goal requires to access new generation instruments that are capable to offer sensitivity and spectral resolution that are unprecedented.

In this context, the next generation radio (e.g. SKA and its precursors, like MeerKAT), mm. (e.g. Millimetron, and in general mm. experiment with spatially-resolved spectroscopic capabilities) and X-ray instruments will definitely shed light on the origin of radio halos in galaxy clusters and on their cosmological evolution. We will discuss the impact of these results on high-energy properties of galaxy clusters in a forthcoming study (Colafrancesco et al. in preparation, see also Colafrancesco et al. 2012).

As for the polarized SZE, we have been able to solve the polarized relativistic Boltzmann equation in the Thomson regime and extract the Stokes parameters associated with the multipoles of the CMB. The spectral features of the Stokes

parameters arising from the quadrupole and the octupole have been computed. One of the first result to be noted is that higher-order multipoles, like octupole etc., also contribute to the polarization of the SZE, which is not the case in the non-relativistic derivation, and that each multipole has different spectral features. This means that computing polarization of SZE in the full relativistic regime allows one to access higher-order anisotropy of the primordial CMB radiation seen at the cluster location. These higher-order multipoles of the CMB carry great astrophysical and cosmological information, as we have discussed. The Stokes parameters that we derived are found to depend on the radiation seen by the cosmic structure and as well as parameters such as temperature, number density, energies associated with the latter.

The polarization patterns and the spectral features of the SZE in a given cosmic structure provide detailed information to the temperature, energy spectrum, and density distribution of the electrons in the plasma of these structures, as well as on the nature (thermal or non-thermal) of these electrons. We noticed that depending on the energy/momentum distribution of the electron population, the Stokes parameters show different spectral features.

We also note that the kinetic SZE together with its polarization component, can be used to measure the bulk velocity of the plasma in cosmic structure as well as of substructures formed during cluster formation. This, in turn, allows particle acceleration/re-acceleration models and other models for the origin of non-thermal phenomena in clusters to be constrained. Combining the SZE polarization with other measurements, such as X-ray and radio, allows hence a tomographic reconstruction of cosmic structures such as galaxy clusters and RG-lobes.

We finally discussed the use of the SZE, together with its polarization, to test fundamental properties of the Universe, like its homogeneity assumption. The multipoles of the CMB only reveal themselves when relativistic effect is taken into account in computing the SZE polarization, hence providing a direct link to the isotropy/anisotropies of the CMB at the cluster location in the Universe. This fact provides us with the unique opportunity to know how the

distribution of matter and radiation is at different locations in the Universe. The SZE in intensity is actually the monopole seen by a galaxy cluster (or a radiogalaxy) at its location, while the SZE polarization gives information about the anisotropy of the radiation as seen at that location, hence allowing us to access other properties of the last scattering epoch. Observing the SZE (both intensity and polarization) in cosmic structures allows hence to test the homogeneity of the Universe by looking at the primordial structure of the CMB radiation at different places in the cosmos where clusters (and radio galaxies) are located (in space and time). The direct measurements of the dipole, quadrupole and octupole at different location in the Universe are therefore able to provide stringent constraints on the hypothesis that the Universe is homogeneous. The dipole can be inferred by the kinetic SZE while the quadrupole and octupole can be inferred from the polarization of the SZE.
Combining millimeter and low-frequency SZE observations should allow to separate the quadrupole from the octupole, since the latter is zero around frequency $\sim$ 280 GHz - 341 GHz for cluster temperature ranging between 1 keV to 5 keV. At low frequencies the quadrupole is mostly dominant over the octupole. In this respect, we also stress here that the SZE polarization is also a direct measurement of the CMB quadrupole and of the other higher-order multipoles which are directly linked to the primordial irregularities at the epoch of recombination.

To conclude, we have made an extensive study of the SZE and its polarization in various cosmic structures, and we discussed how this effect provides us with unique probes not only for understanding the plasma that resides in cosmic structures, but also to use cosmic structures as unique cosmological probes.
Because the structure of plasma inhabiting cosmic structures is very complex and manifest itself via different radiation mechanisms (such as X-ray, radio and SZE), this demands for a multi-frequency approach in order to fully understand the formation and evolution of these cosmic structures and to use them as reliable cosmological probes. The combination of observations from Planck, ACT, SPT, and forthcoming instruments such as MeerKAT, as well as the SKA, and the future CTA would definitely allow us to increase our understanding

of the different structures of the Universe by providing us with an appropriate multi-frequency platform to study the intimate details of cosmic structures with the SZE.

Bibliography

[1] Abell,G.O 1958, Astrophys.J.suppl, 3, 211

[2] Ade, P.A.R. et al 2013, arXiv:1303.5076

[3] Akritas, M. and Bershady, M. 1996, ApJ, 470, 706

[4] Ameglio, S. et al. 2006, MNRAS, 369, 1459

[5] Arnaud, M. et al. 2010, A & A, 517, 92

[6] Bahcall, N.A, 1995, ApJ,198, 249

[7] Bartelmann, M. & Schneider, P. 1999, A&A, 345, 17

[8] Basu, K. 2012, MNRAS, 421, L112

[9] Bautz, L.P & Morgan W.W 1970, Astrophys.J.Lett. 162, L149

[10] Bennett, C.L et al. 2003, Astrophys. J. Suppl., 148, 1 [astro-ph/0302207]

[11] Birkinshaw, M.1999, Physical Report, 310, p 97-195

[12] Blandford, R.D. & Narayan, R. 1992, ARAA, 30, 311

[13] Blasi, P. and Colafrancesco, S. 1999, Astro Particle Physics, 12, 169

[14] Blasi,P. & Colafrancesco, S. 1998, Astroparticle physics,9,227

[15] Bohringer, H. & Werner, N. 2009, A&A rev, arXiv:0907.4277

[16] Bond, J.R. et al. 1991, ApJ, 379, 440

[17] Bondi, H., 1947, MNRAS, 107, 410 .

[18] Brunetti , G. et al.2001, MNRAS, 320,365

[19] Brunetti G, Cassano, R., Dolag, K. and Setti, G. 2009, A&A, 507, 661

[20] Caldwell, R.R. & Stebbins, A. 2008, Phys.Rev.Lett, 100, issue 19 (arXiv:0711.3459 [astro-ph])

[21] Calstrom, J. et al, 2000, "Particle physics and the Universe, proceedings of Nobel symposium 109, Haga slott, Enkoping, Sweden, 20-25 August 1998" , 148, 40

[22] Calstrom, J. et al, 2002, A &A , p 643-680, 40

[23] Carilli, C.L & Taylor, G.B 2002, ARAA, 40, 319

[24] Ce'le'rier, M.-N. 2000, A&A, 353, 63

[25] Challinor et al. 2000, MNRAS, 312, 159

[26] Challinor, A. and Lasenby, A., 1998, ApJ, v 499, p1

[27] Chandrasekhar, S., "Radiative Transfer", Dover publication, 1960

[28] Colafrancesco, S. ,2009, S.A.It, 81,104

[29] Colafrancesco, S. & Marchegiani, P. 2011, A&A, 535, 208

[30] Colafrancesco, S. & Mele , B. 2001, ApJ, 562, 24

[31] Colafrancesco, S. & Vittorio, N. 1994, ApJ, 422, 443

[32] Colafrancesco, S. 1999, in "Diffuse thermal and relativistic plasma in galaxy clusters". Edited by Hans Bohringer, Luigina Feretti, Peter Schuecker. Garching, Germany : Max-Planck-Institut fur Extraterrestrische Physik, 1999, p.269

[33] Colafrancesco, S. 2008, MNRAS, 385, 2041-2048

[34] Colafrancesco, S. 2012, invited review at the Frascati Meeting 'Frontier objects between particle physics and astrophysics', Vulcano (Italy), in press.

[35] Colafrancesco, S. and Blasi, P. 1998, Astro Particle Physics, 9, 227

[36] Colafrancesco, S. and Marchegiani, P. 2008, A&A, 484, 51

[37] Colafrancesco, S. et al, 2012, A&A, in press, arXiv:1312.1846v1 [astro-ph.CO]

[38] Colafrancesco, S. et al. 2003, A&A 397, 27-52

[39] Colafrancesco, S., Lucchin, F. & Matarrese, S. 1989, ApJ, 345, 3-11

[40] Colafrancesco, S., Profumo, S., & Ullio, P. 2006, A&A, 397, 27

[41] Colafrancesco,S. et al. 2013, A&A, 550, A92

[42] Cook, R. and Dell'Antonio, P. 2012, ApJ, 750, 14

[43] Dennison, B. 1980 ApJ,239,L93

[44] Dressler A, 1978, Ap.J, 226, 55

[45] Dunkley, J., et al., 2009, ApJ, 701, 1804

[46] Ensslin, T and Kaiser, C 2000, A&A, 360, 417

[47] Erlund, M.C. et al 2006, MNRAS, 371, 29

[48] Feng, J.L. 2010, ARAA, 48, 495

[49] Feretti, L. et al,2004, New Astronomy Reviews elsevier, v 48,1137-114

[50] Feretti, L. et al. 2012, A&A Rev., 20, 54

[51] Fusco-Femiano et al. 1999, ApJ, 513, L21

[52] Giovannini, G. and Feretti, L. 2000, New Astronomy, 5, 335

[53] Giovannini, M. 2004, Int.J.Mod.Phys.,D13,391

[54] Govoni, F. & Feretti, L. 2004, Int.J.Mod.Phys, D13, 1549

[55] Guidetti, D. et al 2011, MNRAS, 413, 2525

[56] Hand,N. et al. 2012, Phys.Rev.Lett, 109, issue 4, 041101

[57] Hansen, F. and Lilje, P., 1999, MNRAS, vol 306 p 153-160

[58] Hoekstra,H. et al. 2013, Space Science Reviews, 177,75

[59] Hu, W. & Dodelson, S. 2002, ARAA, 40, 171

[60] Itoh, N., Kohyama, Y., Nozawa, S., 1998, ApJ, vol 502, p 7

[61] Jaffe, W.J. 1977, ApJ, 212, 1

[62] Jungman, G., Kamionkowski, M. & Griest, K. 1996, Physical Report, 267, 195

[63] Kaastra, J.S., Bleeker, J.A.M. & Mewe, R. 1998, Nucl.Phys.B, 69, 567

[64] Keshet, U et al. 2004, ApJ, 617, 281

[65] Kompaneets, A.S 1956, Zh.E.F.T., 31, 876. Translation in Sov. Phys. JETP, 4, 730 (1957)

[66] Kravtsov, A.V & Borgani, S. 2012, ARAA, 50, 353

[67] Lacey, C. & Cole, S. 1993, MNRAS, 262, 627

[68] Lieu et al. 1996, Science, 274, 1335

[69] Longair, M. 1993, High Energy Astrophysics (Cambridge University Press)

[70] Maartens, R. 2011, (arXiv:1104.1300)

[71] Mather, J.C et al. 1990, ApJ,354,L37 and Mather,J.C. et al. 1994, ApJ, 420,439

[72] Miniati, F. et al. 2001. ApJ, 562, 233

[73] Nagirner, D.I., Poutanen, J., 1994, AP & SS Reviews, 9,1

[74] Narayanan,V.K & Croft, R.A.C 1999, ApJ,515,471

[75] Nozawa, S. and Kohyama, Y., 2009, Physical Reviews D, vol 79, 083005

[76] Nozawa, S., Kohyama, Y., Itoh, N., 2010, Physical Review D , vol 82, 103009

[77] Ota, N., and Mitsuda, K. 2004, A&A, 428, 754

[78] Peebles, P.J.E,1993, Princeton University Press, "Principles of physical cosmology"

[79] Penzias,A.A. & Wilson, R.W. 1965,ApJ,142,419

[80] Peccei, R. D. & Quinn, H.R. 1997, Phys. Rev. Lett 38, Issue 25, 1440

[81] Pfrommer, C. et al. 2008, MNRAS, 385, 1211

[82] Planck Collaboration 2011, A& A, 536, 8

[83] Planck collaboration 2013, eprint arXiv:1303.5083

[84] Portsmouth, J. and Bertschinger, E., 2004a, arXiv:astro-ph/0412094

[85] Portsmouth, J. and Bertschinger, E., 2004b, arXiv:astro-ph/0412095

[86] Press, W. & Schechter, P. 1994, ApJ, 187, 425

[87] Prmiack, J.R. 1997 [arXiv:astro-ph/9707285]

[88] Reed, B.C. 1992, Am. J. Phys., 60, 59

[89] Reichert et al. 2011 and Tucker, W. et al. 1998, ApJ, 496,L5

[90] Reichert, A. et al. 2011, A&A, 535, 4

[91] Rines, K. et al. 2013, ApJ, 767, 15

[92] Roettiger ,K., Stone, J.M. & Burns, J.O. 1999, ApJ, 518,594

[93] Roettiger, K., Burns, J.O. & Stone, M. 1999, ApJ, 518, 603

[94] Roland , J. 1981, A& A , 93, 407

[95] Ruan, J.,J., et al 2013, MNRAS, 432, 3508

[96] Rybicki, G. B., & Lightman, A. P. 1979, Radiative Processes in Astrophysics (New York: Wiley)

[97] Sarazin, C.L 1988, "X-ray emission from clusters of galaxies", Cambridge Univ. Press: Cambridge

[98] Sarazin, C.L. 1999, ApJ, 520, 529

[99] Sarazin, C.L.,2008, Lect.Notes Phys, 740,1-30

[100] Sazanov, S.Y. & Sunyaev, R.A., 1999, MNRAS, 310, 765

[101] Sikivie, P. 2010, Int.Mod.Phys, 25,554

[102] Silk, J. & White, S.D.M 1978, ApJ, 226, L03

[103] Skillman, S.W. et al. 2012, preprint arXiv:1211.3122

[104] Smoot,G.F et al. 1992,ApJ,396,L1

[105] Spergel, D.N. et al 2003, ApJ, 148, 175

[106] Sunyaev, R.A & Zel'dovich, Ya.B 1972, comments Astrophys.SpaceSci.,4,173

[107] Sunyaev, R.A. & Zel'dovich, Y.B., 1980, MNRAS, 190, 413

[108] Tullio, M.,2011, "Tomografia delle strutture cosmiche attraverso lo studio della polarizzazione dell'effetto S-Z", Tesi di Laurea in Astronomia ed Astrofisica.

[109] Vergados, J.D., Hansen, S.H & Host, O. 2008, Physical Reviews, D77

[110] Voit, M. 2005, Rev.Mod.Phys, 77, 207-258

[111] Wolf, M., 1906, Astron.Nachr.170,211

[112] Wolfe, B. & Melia, F. 2006,ApJ, 638, 125

[113] Wolfe, B. & Melia, F. 2008, ApJ, 675, 156

[114] Wright, E.,1979, ApJ, 232,348-351

[115] Wu, F., Xue, Y. and Fang, L. 1999, ApJ, 524, 22

[116] Zhang, Y. et al. 2011, A&A, 105, 526

[117] Zwicky, F. 1933, Helv.Phys.Acta, 6, 110

[118] Zwicky,F. 1937, ApJ,86,217

Appendix A

Photon re-distribution functions of the CMB radiation

We present here the re-distribution functions of the CMB photons in the SZE and the spectra associated with each multi-pole (monopole, dipole, quadrupole, octopole) for two types of electron populations namely thermal and non-thermal populations.

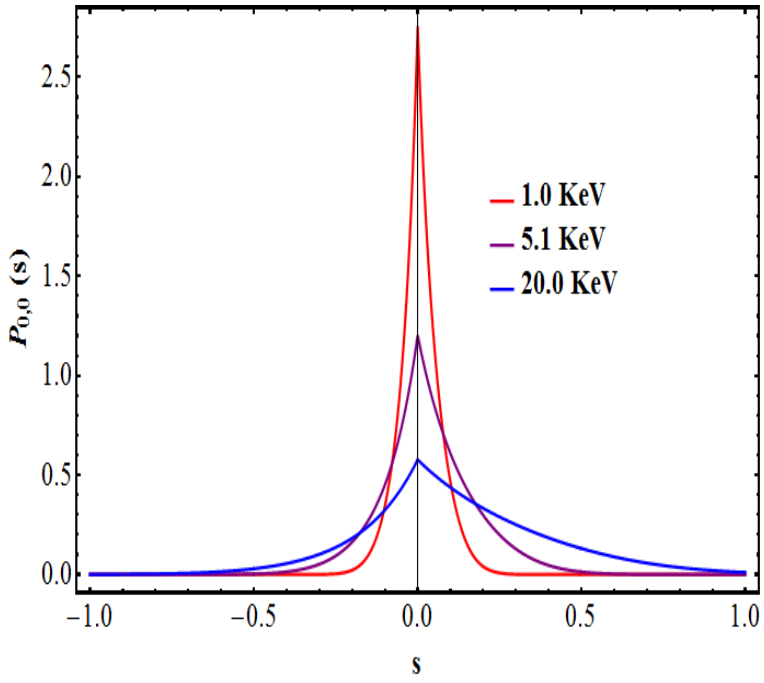

Figure A.1: The re-distribution function $P_{0,0}(s)$ associated with the monopole for a thermal population of electrons.

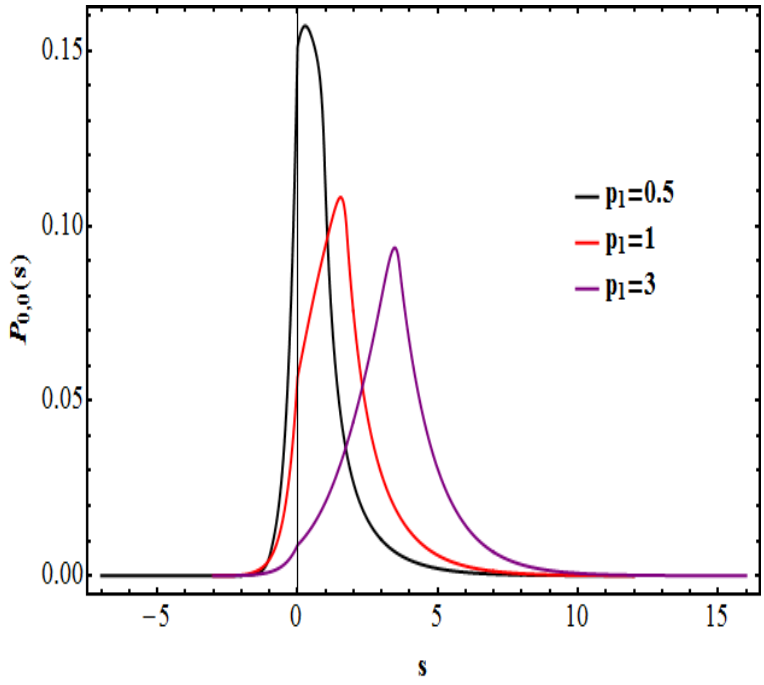

Figure A.2: The re-distribution function $P_{0,0}(s)$ associated with the monopole for a non-thermal population of electrons.

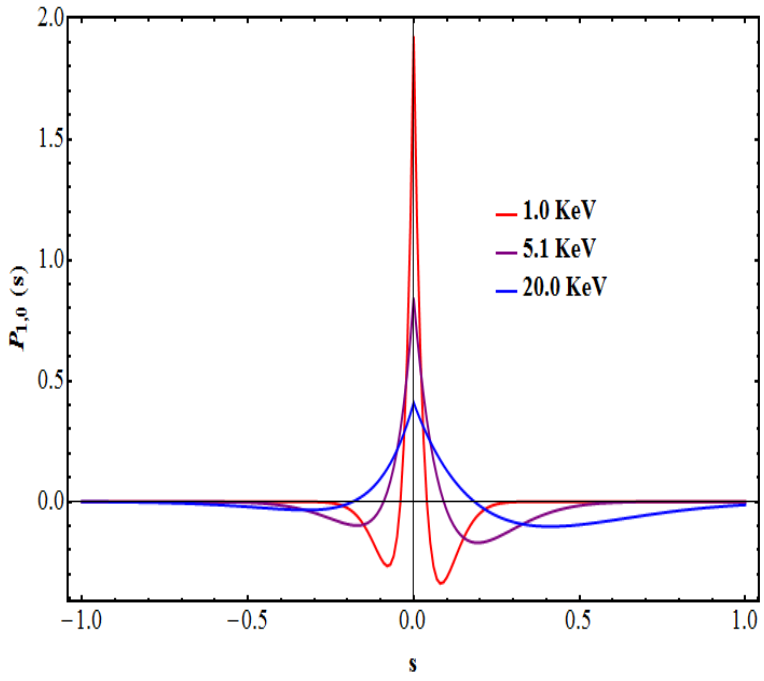

Figure A.3: The re-distribution function $P_{1,0}(s)$ associated with the dipole for a thermal population of electrons.

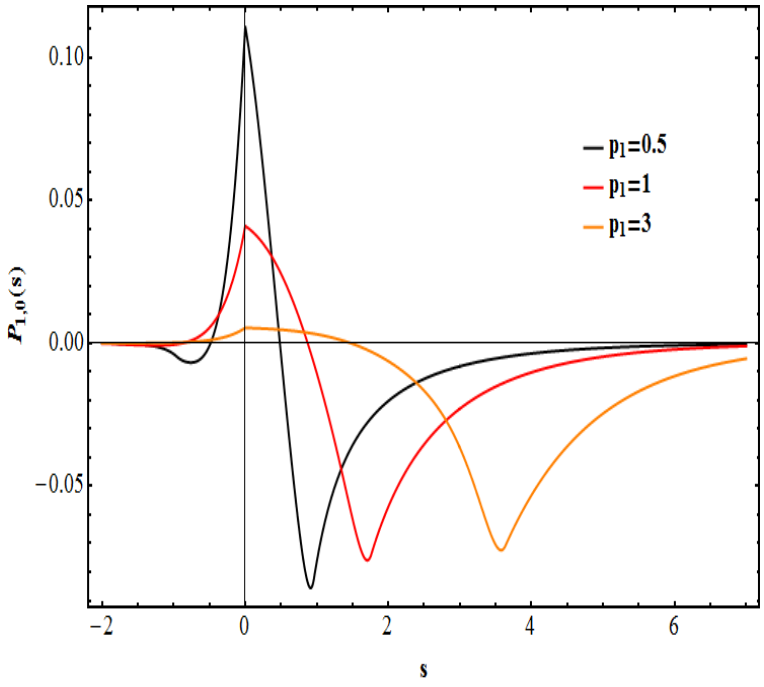

Figure A.4: The re-distribution function $P_{1,0}(s)$ associated with the dipole for a non-thermal population of electrons.

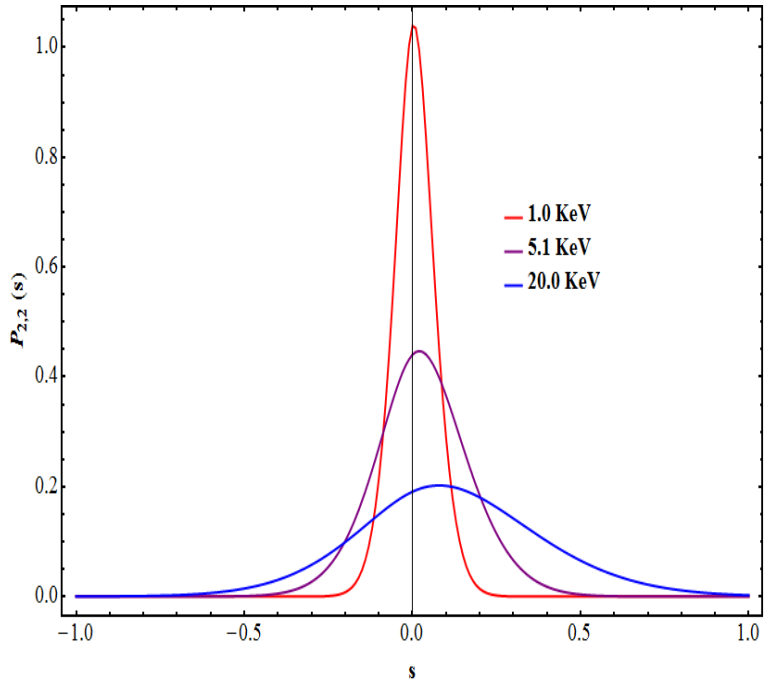

Figure A.5: The re-distribution function $P_{2,2}(s)$ associated with the quadrupole for a thermal population of electrons.

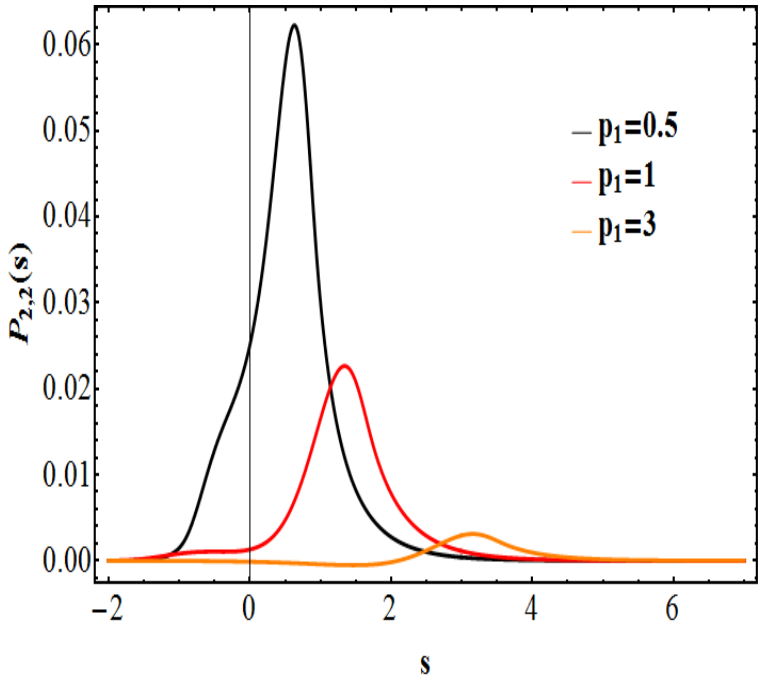

Figure A.6: The re-distribution function $P_{2,2}(s)$ associated with the quadrupole for a non-thermal population of electrons.

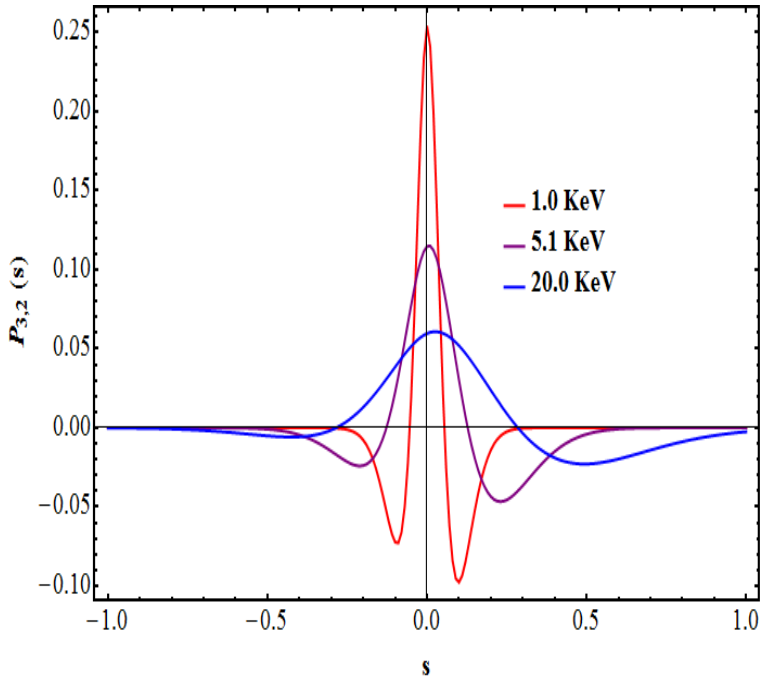

Figure A.7: The re-distribution function $P_{3,2}(s)$ associated with the quadrupole for a thermal population of electrons.

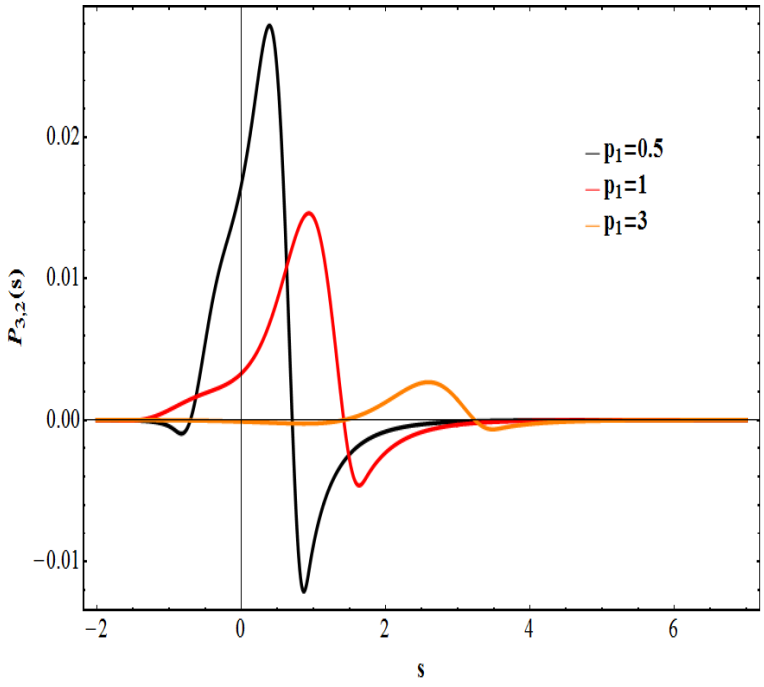

Figure A.8: The re-distribution function $P_{3,2}(s)$ associated with the quadrupole for a non-thermal population of electrons.

Appendix B

The RH clusters sample

We present here the sample of radio-halo clusters that we derived (see Colafrancesco et al. 2013) using data from the Planck collaboration (2011), Brunetti et al. (2009) and Reichert et al. (2011). We verified that these clusters are actually radio-halos by cross-correlating these data with those provided by Feretti et al. (2012).

Table B.1: The RH clusters sample. Clusters with "*" means no errors available and "**" means no avaliable data

Cluster	z	L_X (10^{44} erg s^{-1})	$P_{1.4}$ (10^{24} W/Hz)
1ES0657	0.2994	65.2 ± 0.90	28.21 ± 1.97
RXCJ2003	0.3171	27.23 ± 4.95	12.30 ± 0.71
A2744	0.3080	22.12 ± 1.70	17.16 ± 1.71
A2163	0.2030	64.1 ± 5.3	18.44 ± 0.24
A1300	0.3071	18.0 ± 1.50	6.09 ± 0.61
A0665	0.1816	21.7 ± 2.00	3.98 ± 0.39
A773	0.2170	20.9 ± 1.60	1.73 ± 0.17
A2256	0.0581	10.7 ± 0.90	0.68 ± 0.12
Coma	0.0231	10.44 ± 0.28	0.72 ± 0.06
A0520	0.2010	20.1 ± 0.70	3.91 ± 0.39
A209	0.2060	13.3 ± 1.10	1.19 ± 0.26
A754	0.0535	12.94 ± 0.99	1.08 ± 0.06
A401	0.0737	16.8 ± 1.0	0.22*
A697	0.282	41.9 ± 2.3	1.9*
A781	0.3004	6.3 ± 1.0	4.07*
A1995	0.3186	17.1 ± 0.2	1.35*
A2034	0.113	9.5 ± 1.0	4.37*
A2218	0.1756	11.1 ± 0.8	0.40*
A1689	0.1832	28.4 ± 1.0	**
MACSJ0717	0.5548	84.18 ± 1.01	50.0 ± 10
A1914	0.1712	21.70 ± 1.1	5.24 ± 0.24
A2219	0.2256	45.10 ± 2.3	1.23 ± 0.57
A2255	0.0806	6.50 ± 0.7	0.89 ± 0.04

Table B.2: Cluster values for Y_{SZ} and associated uncertainty Θ_X

Cluster	Y_{SZ} (arcmin^2)	ΔY_{SZ} (arcmin^2)
1ES0657	0.0067	0.0003
RXCJ2003	0.0027	0.0004
A2744	0.0042	0.0005
A2163	0.0173	0.0007
A1300	0.0035	0.0005
A0665	0.006	0.0005
A773	0.0038	0.0004
A2256	0.0242	0.0009
Coma	0.1173	0.0054
A0520	0.0046	0.0006
A209	0.0053	0.0005
A754	0.033	0.0012
A401	0.0193	0.0016
A697	0.0051	0.0005
A781	0.0017	0.0003
A1995	0.0015	0.0003
A2034	0.0055	0.0008
A2218	0.0044	0.0003
A1689	0.0071	0.0008
MACSJ0717	0.0028	0.0004
A1914	0.0057	0.0005
A2219	0.0085	0.0005
A2255	0.0103	0.0006